Modeling Electromagnetic Interactions of Molecules in Nanophotonic Materials

Cristian A. Marocico

Zernike Institute PhD thesis series 2012-28

ISSN	1570-1530
ISBN book	978-90-367-5868-0
ISBN electronic	978-90-367-5867-3

The work described in this thesis was performed at the Centre for Theoretical Physics and the Zernike Institute for Advanced Materials, Rijks*universiteit* Groningen. This work was supported by the NanoNed technology program of the Dutch Ministry of Economic affairs.

Printed by PrintPartners Ipskamp B.V., Enschede, The Netherlands

University of Groningen
Zernike Institute
for Advanced Materials

RIJKSUNIVERSITEIT GRONINGEN

Modeling Electromagnetic Interactions of Molecules in Nanophotonic Materials

Proefschrift

ter verkrijging van het doctoraat in de
Wiskunde en Natuurwetenschappen
aan de Rijksuniversiteit Groningen
op gezag van de
Rector Magnificus, dr. E. Sterken,
in het openbaar te verdedigen op
maandag 12 november 2012
om 12:45 uur

door

Cristian Adrian Marocico

geboren op 19 april 1980
te Timişoara, Roemenië

Promotor:	Prof. dr. J. Knoester
Beoordelingscommissie:	Prof. dr. A. Polman Prof. dr. H.A. de Raedt Prof. dr. ir. P.H.M van Loosdrecht

ISBN: 978-90-367-5868-0

Contents

General Introduction **1**

1 Theoretical Introduction **5**
1.1 Classical and Quantum Electrodynamics 6
1.1.1 The Classical Theory of Electrodynamics 6
1.1.2 Quantization of the Electromagnetic Field 9
1.2 Spontaneous Emission and Energy Transfer 11
1.2.1 Spontaneous Emission 12
1.2.2 Energy Transfer 14
1.3 The Green's Tensor in Cartesian and Cylindrical Coordinates 19
1.3.1 The free-space Green's tensor in Cartesian coordinates 19
1.3.2 The free-space Green's tensor in Cylindrical coordinates . . . 25
1.4 An Introduction to Surface Plasmon-Polaritons 27
1.4.1 General introduction to surface plasmon-polaritons 27
1.4.2 Surface plasmon-polaritons on a single planar interface 27

2 Metallic Slab and Planar Waveguide **31**
Abstract 31
2.1 Introduction 32
2.1.1 The Green's tensor in a multilayered geometry 32
2.2 Metallic slab in a dielectric host medium 33
2.2.1 Spontaneous Emission 37
2.2.2 Energy Transfer 40
2.3 Planar Waveguide 44

2.3.1 Spontaneous Emission 44
2.3.2 Energy Transfer 48
2.4 Summary and conclusions 50

3 Intermolecular interactions and ET near a circular cylinder 53
Abstract 53
3.1 Introduction 54
3.2 The Green's Tensor for an infinite cylinder 54
3.2.1 Formalism 54
3.2.2 Numerical implementation 58
3.3 Results and Discussion 59
3.3.1 Frequency-independent dielectric permittivity 60
3.3.2 Drude dielectric permittivity 63
3.3.3 Frequency-dependence of the energy transfer rate 66
3.4 Summary and Conclusions 69

4 Intermolecular interactions and ET in PhCSs 71
Abstract 71
4.1 Introduction 72
4.2 Theoretical Framework 74
4.2.1 The Finite-Difference Time-Domain Method 74
4.2.2 Decay rates, energy-transfer and FDTD calculations 75
4.2.3 Photonic Crystals and band structures 77
4.3 Results and Discussion 78
4.3.1 Decay rates 79
4.3.2 Energy Transfer rates 83
4.4 Summary and Conclusions 85

Conclusions 87

Samenvatting 93

Acknowledgements 97

Bibliography 99

List of Figures

1.1 Feynman diagrams for resonance energy transfer 16
1.2 Geometry of two half-spaces 22
1.3 Band structure and electric field of SPPs in a half-space geometry . . 28
1.4 Decay lengths of SPPs in a half-space geometry 30

2.1 Illustration of the multilayered geometry 32
2.2 Illustration of the metal slab in a dielectric host geometry 34
2.3 Band structure of SPPs in a slab geometry 37
2.4 Spontaneous emission near a metallic slab 39
2.5 Molecular configurations for ET transfer near a metallic slab 41
2.6 Energy transfer near a metallic slab 42
2.7 Geometry of the waveguide 44
2.8 Band structure of SPPs in a planar waveguide geometry 45
2.9 Decay rates above a planar waveguide 46
2.10 Decay rates inside a planar waveguide 47
2.11 Energy transfer rates in a planar waveguide geometry 49

3.1 Geometry of the cylinder in a dielectric background 54
3.2 Integration contour in the complex k_z-plane 59
3.3 Relative energy transfer rate near a dielectric cylinder 61
3.4 Relative multipole contributions 63
3.5 Relative energy transfer near a Drude metal cylinder 65
3.6 Dispersion relations of SPPs on a Drude metal cylinder 66
3.7 Frequency-dependence of ET rate near a Drude metal cylinder 67

4.1 Geometry and reciprocal lattice of 2D PhCs 73
4.2 Band diagrams of 2D PhCs 77
4.3 Geometry of a PhCS 78
4.4 Band diagram of PhCSs 79
4.5 Relative decay rate in a PhCS 80
4.6 Relative decay rate in a AuPhCS 82
4.7 Relative energy transfer rate in a PhCS 83
4.8 Relative energy transfer rate in a AuPhCS 85

General Introduction

There's plenty of room at the bottom
– R.P. Feynman, December 29th 1959, Caltech

Overview

The formulation by James Clerk Maxwell (1831–1878) of the laws of classical electrodynamics (Maxwell's equations) is universally considered as one of the single greatest contributions to our current understanding of the world. Richard Feynman considered its importance in human history to dwarf that of the American Civil War, to which it was contemporary [1, p. I.11]. These laws beautifully merge the – until then – disparate phenomena of electricity, magnetism and light into a unified synthesis, elegant through its simplicity, both mathematical and conceptual. Among other things, it predicted the existence of electromagnetic waves traveling at the speed of light, a prediction confirmed in 1887 by Heinrich Hertz (1857–1894) who managed to generate and detect radio waves. The fact that the speed of electromagnetic waves was the same as the speed of light provided conclusive proof that light was an electromagnetic wave.

With the advent of *quantum theory* at the beginning of the 20^{th} century, our understanding of the nature of light underwent profound changes at the hands of Max Planck (1858–1947), Albert Einstein (1879–1955), Louis de Broglie (1892–1987), Niels Bohr (1885–1962), and others. The corpuscular or discrete nature of light was revealed and the concept of the *photon* as the smallest "piece of light" was introduced. At the same time, atoms and their constituents were discovered to sometime behave

like waves. This unity through duality in the microscopic realm was an important conceptual shift.

Towards the middle of the 20$^{\text{th}}$ century, Richard Feynman, Julian Schwinger, Sin-Itiro Tomonaga and Freeman Dyson completed the new quantum theory of light and matter, *quantum electrodynamics* (QED), for which the first three physicists shared a Nobel Prize in 1965. In this new paradigm, the electromagnetic interactions between electrons and protons (charged particles, in general), are mediated by the particles of light, photons.

The quantum theory of light and matter or quantum electrodynamics is, to this day, the most precise and all-encompassing theory of physics. The same Feynman compared its accuracy in agreeing with experiments to the feat of measuring the width of North America and have the result accurate to within the width of a human hair. As for the scope of the theory, it is thus far our most fundamental commonly accepted theory of electromagnetic phenomena. It can satisfactorily explain the spontaneous emission of atoms and molecules, the Lamb shift, the anomalous magnetic moment of the electron, and many other phenomena. It is by no means far removed from everyday life, but has important direct technological applications, such as the laser, PET scans, solar cells, and a variety of others. Indeed, the technological potential of quantum electrodynamics has not nearly been fully explored, as we hope to show in this work. Our focus in this work shall be solely on the spontaneous emission of molecules and the transfer of excitation energy between molecules.

Considering the interaction of radiation and matter, Einstein realized in 1917 that thermodynamic equilibrium between the two requires the existence of three interaction processes: *spontaneous emission*, in which an initially excited atom, in the absence of external radiation spontaneously emits a photon and decays to a lower energy state, *stimulated emission*, in which the presence of external radiation induces the decay of an excited atom (this effect underlies the functioning of lasers) and *absorption*, in which an atom absorbs a photon from the external radiation and is excited to a higher energy state. As the process of spontaneous emission occurs in the absence of external radiation, it is reasonable that it should be an intrinsic property of the emitting atom, and not depend on any external circumstances.

In 1946, however, Purcell was able to show that this is not the case [2]. The environment of the atom is able to influence its spontaneous emission (SE) rate in the following manner: although the excited atom exists in an electromagnetic vacuum, after emission there is at least one photon present and the existence of this photon must be compatible with the *(local) density of states* (LDOS) of the electromagnetic field in whatever surroundings the atom finds itself in, i.e. cavities, mirrors, etc. The environment, therefore, will modify the SE rate of an atom through the LDOS. Since Purcell's early work on the subject, different geometries have been studied in conjunction with the modification of the spontaneous emission rate: planar metallic and dielec-

tric interfaces [3–10], micro-cavities [11–19] and multilayered geometries [20, 21], nanorods [22–26], nanospheres [27–32], photonic crystals [33–39] and other nanostructures [40–44].

When more than one atom is present at a time and at least one of these atoms is in an excited state, another important interaction process can occur: the transfer of the excitation energy from the excited atom to one of the non-excited ones. This process of resonant transfer of excitation energy (ET) between two atoms or molecules is the main mechanism by which an excited system transfers its electronic excitation to a neighboring one. It plays an essential role in microscopy, e.g. *scanning near-field optical microscopy* (SNOM), nanophotonics, e.g. *light-emitting diodes* (LEDs), micro- and nano- lasers, biophysics, e.g. photosynthesis [45]. Considering the dependence of the energy transfer process on the distance between the two atoms involved, one can distinguish several regimes[1]: the non-radiative short-range regime first described by Förster [46], valid when $R \ll \lambda$ (or $R \lesssim 10$nm for the optical regime), with a R^{-6} dependence characteristic of the squared instantaneous Coulomb coupling between two dipoles, and the radiative long-range regime [47], valid when $R \gg \lambda$, which has a R^{-2} distance dependence. In the above, λ is the wavelength associated with the transition of the donor molecule. There also exists an intermediate regime, valid when $R \approx \lambda$, with a R^{-4} distance dependence. The transfer of the excitation can always be regarded as proceeding through the exchange of photons. In the Förster regime, these photons are virtual, i.e. they appear only in intermediate states and are unobservable, thus not being required to conserve energy. This "energy freedom" is, nevertheless, not complete, as one can derive from the energy-time "uncertainty" relations a maximum spread in energy, associated with the minimum lifetime of these virtual photons, $\tau_m = R/c$ [48, 49]. In the radiative regime, on the other hand, the photons are real, their energy equals that of the electronic transition considered and the energy transfer process can be viewed as the emission and absorption of a real photon.

As for the case of the SE rate, the environment in which the interacting donor and acceptor are placed can have a profound influence on the energy transfer rate between them. Unlike the case of the SE rate, however, where the rate is proportional to the LDOS, the effect of the environment on the energy transfer rate is more complex, as we shall show in this work.

The spontaneous emission rate of emitters such as quantum dots, fluorescent dye molecules, etc., finds important technological and commercial applications in novel light sources such as nanolasers and light emitting diodes (LEDs). As we mentioned in a previous paragraph, the process of energy transfer is ubiquitous in nature and technology and, particularly in the Förster regime, plays a central role in such devices as solar cells and LEDs, it can act as a very sensitive nanoscale ruler [50–52], among

[1] We confine our investigation in this work to the weak-coupling regime, where the energy transfer process is irreversible and one can, therefore, define an energy transfer *rate*.

other applications.

Given the numerous applications of the resonance energy transfer, controlled modification of the transfer rate is highly desirable. One way to achieve modifications of the transfer rate is by using inhomogeneous geometries. Theoretical and experimental work has been carried out in order to study the modifications of the energy transfer rate in different geometries: planar dielectric interfaces [53, 54], micro-cavities [55–59], dielectric spheres [60–62] and nanofibers [63]. In all cases, both enhancement and inhibition of the energy transfer rate have been observed and calculated.

One aspect of placing the interacting molecules in inhomogeneous environments is the fact that these environments support interesting modes of the electromagnetic field, such as surface-plasmon polaritons (SPPs) [64]. The properties of these surface plasmon-polaritons, such as subwavelength confinement and large electric field enhancement, can be successfully exploited for fine control of energy transfer at the nanoscale [65–70].

From the overview presented so far, and as we have already mentioned, controlling the energy transfer process at the nanoscale is highly desirable. In this work we undertake the task of theoretically and numerically investigating the energy transfer process in several nanoscale geometries, with a bias towards the role of surface-plasmon polaritons in modifying the energy transfer rate.

Outline of this thesis

The first proper chapter of the thesis, Chapter 1 is mainly dedicated to setting up the theoretical framework for the calculations presented in later chapters. Chapter 2 deals with the spontaneous emission of a molecule and the energy transfer between two molecules in multilayered geometries, with a particular emphasis on the influence of surface plasmon-polaritons on these rates. In Chapter 3 we calculate the emission rate and energy transfer rate between molecules near a circular cylinder. The role of surface plasmon-polaritons is again emphasized. In Chapter 4 a photonic crystal slab of cylindrical air-holes in a dielectric host is investigated with respect to its effect on the electromagnetic properties of atoms and molecules. By adding a metallic substrate to this geometry, the effect of SPPs can be investigated. In the final chapter, we summarize the work presented in the thesis and finish with some conclusions.

CHAPTER 1

Theoretical Introduction

Overview

Throughout this thesis we will, for the most part, use a Green's tensor formalism to calculate the spontaneous emission and energy transfer rates of molecules. The Green's tensor represents a solution of the Maxwell equations of electrodynamics corresponding to the electric field produced by a point dipole source. As such, it is perfectly suited to express interactions between molecules approximated as point dipoles. Furthermore, the Green's tensor formalism can easily take into account inhomogeneous dispersive and absorbing surroundings [71]. Given that the Green's tensor represents the response of a particular geometry to a point-like dipolar excitation, it essentially contains all the information regarding that geometry. In addition to the spontaneous emission and energy transfer rates, other quantities such as the frequency shift [25,72], electromagnetic scattering [73–75], Casimir-Polder interactions [76–78] can be calculated from knowledge of the Green's tensor.

In this chapter we give a somewhat detailed exposition of the Green's tensor formalism used in this work to calculate spontaneous emission and energy transfer rates in nanostructured environments. We start with the formulation of the equations of classical and quantum electrodynamics in terms of the Green's tensor (Sec. 1.1), after which we present a derivation of the spontaneous emission and energy transfer rates in the Green's tensor formalism (Sec. 1.2). Next we show how the homogeneous Green's tensor can be calculated in Cartesian and Cylindrical coordinates (Sec. 1.3). The expressions for the Green's tensor obtained here form the basis for calculating the

Green's tensor in inhomogeneous geometries. Finally, we give a brief introduction to surface-plasmon polariton calculations (Sec. 1.4), with the example of a single planar interface between a metal and a dielectric.

1.1 Classical and Quantum Electrodynamics

1.1.1 The Classical Theory of Electrodynamics

A brief overview of the classical and quantum theories of electrodynamics may be useful at this early point. Classical electrodynamics begins and ends with Maxwell's equations, which are differential equations relating four vector quantities which describe the electromagnetic field: electric field intensity $\mathbf{E}(\mathbf{r},t)$, magnetic field intensity $\mathbf{H}(\mathbf{r},t)$, electric displacement $\mathbf{D}(\mathbf{r},t)$ and magnetic induction $\mathbf{B}(\mathbf{r},t)$. The source of the electromagnetic field described by these four vectors is an electric charge distribution $\rho(\mathbf{r},t)$ and/or an electric current distribution $\mathbf{j}(\mathbf{r},t)$. It is important to mention that these charge and current distributions consist exclusively of *free* charges and currents. Any bound charges and currents (i.e. inside atoms and molecules) are incorporated in a phenomenological way in the field vectors $\mathbf{D}$ and $\mathbf{H}$[1]. In the most general case and using natural units ($c = 1$ and, in the context of quantum theory, $\hbar = 1$), the classical Maxwell equations can be written as [79, p. 2]:

$$\nabla \times \mathbf{E}(\mathbf{r},t) + \frac{\partial \mathbf{B}(\mathbf{r},t)}{\partial t} = 0, \tag{1.1a}$$

$$\nabla \times \mathbf{H}(\mathbf{r},t) - \frac{\partial \mathbf{D}(\mathbf{r},t)}{\partial t} = \mathbf{j}(\mathbf{r},t), \tag{1.1b}$$

to which one adds the divergence equations

$$\nabla \cdot \mathbf{B}(\mathbf{r},t) = 0, \tag{1.1c}$$

$$\nabla \cdot \mathbf{D}(\mathbf{r},t) = \rho(\mathbf{r},t). \tag{1.1d}$$

As a side-note, the four equations above are not independent. Indeed, if one uses the continuity equation

$$\nabla \cdot \mathbf{j}(\mathbf{r},t) + \frac{\partial \rho(\mathbf{r},t)}{\partial t} = 0, \tag{1.2}$$

one can derive the divergence equations (1.1c) and (1.1d) from the curl equations (1.1a) and (1.1b).

[1] Throughout this work, we will explicitly write down the $\mathbf{r}$ and t (or ω) arguments of the fields and distributions only when necessary.

As we mentioned in the opening paragraph of this section, the charge distribution ρ and current distribution $\mathbf{j}$ refer solely to the *free* charges and currents. To account for charges bound up in atoms or molecules, the auxiliary field vectors $\mathbf{D}$ and $\mathbf{H}$ are introduced. These field vectors account for the bound-up charges, currents and spins and, therefore, describe the electromagnetic response of material bodies. Besides depending on the particular properties of the material bodies they describe, the auxiliary vectors can also conceivably depend on the electromagnetic field to which these bodies respond ($\mathbf{E}$ and $\mathbf{B}$). For our purposes here, it is sufficient to consider that the electric displacement vector ($\mathbf{D}$) depends solely on the electric field intensity vector ($\mathbf{E}$) and that the magnetic field intensity vector ($\mathbf{H}$) is a function of the magnetic induction ($\mathbf{B}$) only [80, p. 266]:

$$\mathbf{D} = \mathbf{D}(\mathbf{E}), \qquad \mathbf{H} = \mathbf{H}(\mathbf{B}). \tag{1.3}$$

In the most general case, the functional dependence in Eqs. (1.3), can include non-linear, as well as anisotropic materials. In this work, however, we confine ourselves to isotropic, linear, local and non-magnetic materials[2]. In such materials, the functional relations in Eqs. (1.3) become [80, p. 266]:

$$\mathbf{D}(\mathbf{r},t) = \mathbf{E}(\mathbf{r},t) + \int_0^\infty \mathrm{d}\tau\, \chi(\tau)\mathbf{E}(\mathbf{r},t-\tau), \qquad \mathbf{H}(\mathbf{r},t) = \mathbf{B}(\mathbf{r},t), \tag{1.4}$$

where $\chi(\tau)$ is the linear electric susceptibility [81].

In all the above equations, the field vectors and distributions are given in the time domain (as functions of t). At this point, we can introduce the temporal Fourier transforms of the fields and distributions which, in general, have the form:

$$\mathscr{F}(\mathbf{r},t) = \frac{1}{\sqrt{2\pi}} \int_0^\infty \mathrm{d}\omega\, \mathrm{e}^{-i\omega t}\, \mathscr{F}(\mathbf{r},\omega) + \text{c.c.}. \tag{1.5}$$

Using the Fourier transforms of the fields and distributions in the Maxwell equations (1.1) and the continuity equation (1.2), one obtains these equations in the *frequency-domain* [81]:

$$\nabla \times \mathbf{E}(\mathbf{r},\omega) - i\omega\, \mathbf{B}(\mathbf{r},\omega) = 0, \tag{1.6a}$$

$$\nabla \times \mathbf{B}(\mathbf{r},\omega) + i\omega\, \varepsilon(\omega)\, \mathbf{E}(\mathbf{r},\omega) = \mathbf{j}(\mathbf{r},\omega), \tag{1.6b}$$

$$\nabla \cdot \mathbf{B}(\mathbf{r},\omega) = 0, \tag{1.6c}$$

$$\nabla \cdot [\varepsilon(\omega)\mathbf{E}(\mathbf{r},\omega)] = \rho(\mathbf{r},\omega), \tag{1.6d}$$

[2] Inhomogeneous materials, the subject of this thesis, are described by considering piece-wise homogeneous materials with abrupt transitions between them (i.e. surfaces or interfaces). Relations (1.4) apply strictly to the individual homogeneous components that these materials are made up of.

and

$$\nabla \cdot \mathbf{j}(\mathbf{r},\omega) - i\omega\rho(\mathbf{r},\omega) = 0. \tag{1.7}$$

To arrive at these expressions, we have used relations (1.4) for the auxiliary fields and have introduced the frequency-dependent complex-valued *dielectric permittivity* of the material

$$\varepsilon(\omega) = 1 + \int_0^\infty \mathrm{d}\tau\, \chi(\tau)\, \mathrm{e}^{i\omega\tau}. \tag{1.8}$$

One further simplification of the framework can be achieved by considering all charges and currents as being bundled up in material bodies – we have no free charges or currents. In this case the Maxwell equations become:

$$\nabla \times \mathbf{E}(\mathbf{r},\omega) - i\omega\mathbf{B}(\mathbf{r},\omega) = 0, \tag{1.9a}$$

$$\nabla \times \mathbf{B}(\mathbf{r},\omega) + i\omega\,\varepsilon(\omega)\mathbf{E}(\mathbf{r},\omega) = 0, \tag{1.9b}$$

$$\nabla \cdot \mathbf{B}(\mathbf{r},\omega) = 0, \tag{1.9c}$$

$$\nabla \cdot \mathbf{E}(\mathbf{r},\omega) = 0, \tag{1.9d}$$

and matter reveals itself through the dielectric permittivity, $\varepsilon(\omega)$. As we mentioned above, this permittivity can (and usually is) a complex-valued function of frequency, which we write as $\varepsilon(\omega) = \varepsilon'(\omega) + i\varepsilon''(\omega)$, where $\varepsilon'(\omega)$ and $\varepsilon''(\omega)$ are real functions of frequency, representing the real and imaginary parts of the dielectric permittivity. The dielectric permittivity, as a function of frequency has to satisfy the Kramers-Kronig relations [80, p. 281], which are a consequence of the causality principle.

From the first two Maxwell equations in the frequency domain, (1.9a) and (1.9b), one can derive the Helmholtz equation for the electric field **E**:

$$\boxed{\nabla \times \nabla \times \mathbf{E}(\mathbf{r},\omega) - \omega^2\varepsilon(\omega)\mathbf{E}(\mathbf{r},\omega) = 0,} \tag{1.10}$$

or, taking into account Eq. (1.9d),

$$\nabla^2\mathbf{E}(\mathbf{r},\omega) + \omega^2\varepsilon(\omega)\mathbf{E}(\mathbf{r},\omega) = 0. \tag{1.11}$$

Equivalent expressions hold for the magnetic field **B**. As we mentioned before (footnote on page 7), these equations for the electric and magnetic fields only hold in homogeneous media. This constitutes a severe limitation on the kind of calculations possible in this framework. Extension of this formalism to include inhomogeneous media, i.e. media where the dielectric properties vary as a function of space, as well as frequency, can be accomplished by considering these spatial variations in a piecewise fashion. Hence, $\varepsilon(\omega)$ experiences abrupt jumps at surfaces and interfaces and

is otherwise constant. Maxwell's equations (1.9) (or the Helmholtz equation (1.10)) are then solved inside each of these regions of constant dielectric permittivity and the resulting fields are "welded" at the interfaces by imposing the well-known continuity conditions of electrodynamics [79, p. 34-37], i.e. the continuity of the normal components of $\mathbf{B}$ and of the tangential components of $\mathbf{E}$.

1.1.2 Quantization of the Electromagnetic Field

Passing from the classical to the quantum description of the electromagnetic field, one promotes the electromagnetic field vectors $\mathbf{E}(\mathbf{r},\omega)$ and $\mathbf{B}(\mathbf{r},\omega)$ to quantum operators that satisfy the *quantum Maxwell equations* [82]:

$$\nabla \times \hat{\mathbf{E}}(\mathbf{r},\omega) - i\omega\hat{\mathbf{B}}(\mathbf{r},\omega) = 0, \tag{1.12a}$$

$$\nabla \times \hat{\mathbf{B}}(\mathbf{r},\omega) + i\omega\varepsilon(\omega)\hat{\mathbf{E}}(\mathbf{r},\omega) = \hat{\mathbf{j}}(\mathbf{r},\omega), \tag{1.12b}$$

$$\nabla \cdot \hat{\mathbf{B}}(\mathbf{r},\omega) = 0, \tag{1.12c}$$

$$\varepsilon(\omega)\nabla \cdot \hat{\mathbf{E}}(\mathbf{r},\omega) = \hat{\rho}(\mathbf{r},\omega). \tag{1.12d}$$

In a dielectric without average charge and current densities, the new operators introduced in the above equations, $\hat{\rho}(\mathbf{r},\omega)$ and $\hat{\mathbf{j}}(\mathbf{r},\omega)$, represent the noise charge density operator and the noise current density operator, respectively [83]. These noise operators account for absorption in the medium due to propagation, and are needed if the field vectors are to be promoted to quantum operators in a such a way as to preserve the equal-time commutation relations between the field vectors (see later Eqs. (1.20) and [84]). They can be related to a noise polarization operator $\hat{\mathbf{P}}(\mathbf{r},\omega)$ as follows

$$\hat{\rho}(\mathbf{r},\omega) = -\nabla \cdot \hat{\mathbf{P}}(\mathbf{r},\omega), \tag{1.13a}$$

$$\hat{\mathbf{j}}(\mathbf{r},\omega) = -i\omega\hat{\mathbf{P}}(\mathbf{r},\omega). \tag{1.13b}$$

It can be easily verified that these new operators obey the continuity equation

$$\nabla \cdot \hat{\mathbf{j}}(\mathbf{r},\omega) - i\omega\hat{\rho}(\mathbf{r},\omega) = 0, \tag{1.14}$$

thus deserving the name of *charge* and *current* density operators. Analogous to the classical case, one can derive from the quantum Maxwell equations (1.12) a *quantum Helmholtz equation* for the electric field operator $\hat{\mathbf{E}}(\mathbf{r},\omega)$ [85]:

$$\nabla \times \nabla \times \hat{\mathbf{E}}(\mathbf{r},\omega) - \omega^2\varepsilon(\omega)\hat{\mathbf{E}}(\mathbf{r},\omega) = i\omega\hat{\mathbf{j}}(\mathbf{r},\omega). \tag{1.15}$$

To solve this type of equation, a new quantity is usually introduced, namely the Green's tensor, $\mathscr{G}(\mathbf{r},\mathbf{s},\omega)$. The Green's tensor represents the electromagnetic response

of a particular configuration of material bodies to a unit point-like excitation. Therefore, it obeys the following differential equation:

$$\nabla \times \nabla \times \mathscr{G}(\mathbf{r},\mathbf{s},\omega) - \omega^2 \varepsilon(\omega)\mathscr{G}(\mathbf{r},\mathbf{s},\omega) = \mathscr{I}\delta(\mathbf{r}-\mathbf{s}), \tag{1.16}$$

where $\mathscr{I}$ is the unit 3×3 tensor. The electric field operator $\hat{\mathbf{E}}(\mathbf{r},\omega)$ can now be expressed as a function of the Green's tensor as

$$\hat{\mathbf{E}}(\mathbf{r},\omega) = i\omega \int \mathrm{d}^3 s \mathscr{G}(\mathbf{r},\mathbf{s},\omega)\cdot\hat{\mathbf{j}}(\mathbf{s},\omega). \tag{1.17}$$

Analogous to the definition of the temporal Fourier transforms of the fields in the classical case, Eq. (1.5), it is now possible to define the Schrödinger picture electric and magnetic field operators as

$$\hat{\mathbf{E}}(\mathbf{r}) = \frac{1}{\sqrt{2\pi}}\int_0^\infty \mathrm{d}\omega\, \hat{\mathbf{E}}(\mathbf{r},\omega) + \text{h.c.}, \tag{1.18a}$$

$$\hat{\mathbf{B}}(\mathbf{r}) = \frac{1}{\sqrt{2\pi}}\int_0^\infty \mathrm{d}\omega\, \hat{\mathbf{B}}(\mathbf{r},\omega) + \text{h.c.}, \tag{1.18b}$$

where the Fourier transform has been taken at $t=0$, for simplicity. The magnetic field operator in the frequency domain, $\hat{\mathbf{B}}(\mathbf{r},\omega)$, can be deduced from Eq. (1.12a) to be

$$\hat{\mathbf{B}}(\mathbf{r},\omega) = -\frac{i}{\omega}\nabla\times\hat{\mathbf{E}}(\mathbf{r},\omega). \tag{1.19}$$

These Schrödinger picture electric and magnetic field operators are required to obey the usual equal-time commutation relations of quantum electrodynamics [80] (using natural units again, such that $\hbar = 1$):

$$\left[\hat{E}_i(\mathbf{r}),\hat{E}_j(\mathbf{r}')\right] = \left[\hat{B}_i(\mathbf{r}),\hat{B}_j(\mathbf{r}')\right] = 0, \tag{1.20a}$$

$$\left[\hat{E}_i(\mathbf{r}),\hat{B}_j(\mathbf{r}')\right] = -i\varepsilon_{ijk}\frac{\partial}{\partial x_k}\delta(\mathbf{r}-\mathbf{r}'), \tag{1.20b}$$

a requirement that can be accomplished by introducing the auxiliary vector field operators, $\hat{\mathbf{f}}(\mathbf{r},\omega)$, through the bosonic commutation relations

$$\left[\hat{f}_i(\mathbf{r},\omega),\hat{f}_j(\mathbf{r}',\omega')\right] = \left[\hat{f}_i^\dagger(\mathbf{r},\omega),\hat{f}_j^\dagger(\mathbf{r}',\omega')\right] = 0, \tag{1.21a}$$

$$\left[\hat{f}_i(\mathbf{r},\omega),\hat{f}_j^\dagger(\mathbf{r}',\omega')\right] = \delta_{ij}\delta(\mathbf{r}-\mathbf{r}')\delta(\omega-\omega'), \tag{1.21b}$$

and expressing the noise current density operator in terms of these bosonic vector field operators as

$$\hat{\mathbf{j}}(\mathbf{r},\omega) = \omega\sqrt{2\varepsilon''(\mathbf{r},\omega)}\hat{\mathbf{f}}(\mathbf{r},\omega). \tag{1.22}$$

Following this, the Schrödinger electric field operator becomes

$$\hat{\mathbf{E}}(\mathbf{r}) = i\sqrt{\frac{1}{\pi}}\int_0^\infty \mathrm{d}\omega\,\omega^2 \int \mathrm{d}^3 s\sqrt{\varepsilon''(\mathbf{s},\omega)}\mathscr{G}(\mathbf{r},\mathbf{s},\omega)\cdot\hat{\mathbf{f}}(\mathbf{s},\omega) + \mathrm{h.c.} \tag{1.23}$$

It is this operator that is used in calculating the interactions of matter and radiation.

The newly introduced bosonic vector operators, $\hat{\mathbf{f}}^\dagger$ and $\hat{\mathbf{f}}$, are creation and annihilation operators for medium-dressed states, i.e. polaritons such as surface plasmon-polaritons, as we shall see later in this work. In the limit $\varepsilon'' \to 0$ (and, strictly speaking, $\varepsilon' \to 1$), the noise current operator $\hat{\mathbf{j}}$ vanishes, but the electric field operator from Eq. (1.23) does not vanish and instead reduces to the electric field operator in an inert medium (or vacuum) [86].

In the following section, the framework for calculating the spontaneous emission rate and the energy transfer rate is set up.

1.2 Spontaneous Emission and Energy Transfer

When considering the electronic excitation of an atom or molecule, there are a few salient characteristics, such as its spontaneous emission rate, or the rate of transfer of this excitation to another atom or molecule. Both these processes are quantum mechanical in nature and can, therefore, be studied within the framework of quantum electrodynamics. Both processes arise from the interaction of the atoms or molecules with the quantized electromagnetic field. In order to describe this interaction, we need to introduce the quantized Hamiltonian for the molecule-field system. We shall, in what follows, treat the molecule-field interaction as a perturbation, whence the Hamiltonian of the system can be written as

$$\hat{H} = \hat{H}_{\mathrm{em}} + \hat{H}_{\mathrm{mol}} + \hat{H}_{\mathrm{int}}, \tag{1.24}$$

where $\hat{H}_{\mathrm{em}}$ is the Hamiltonian for the free electromagnetic field, $\hat{H}_{\mathrm{mol}}$ is the Hamiltonian for the atom/molecule in the absence of radiation, and $\hat{H}_{\mathrm{int}}$ is the interaction Hamiltonian between the atom/molecule and radiation. The expressions for these Hamiltonians are [82]:

$$\hat{H}_{\mathrm{em}} = \frac{1}{2}\int \mathrm{d}^3 r\left[\hat{\mathbf{E}}(\mathbf{r})^2 + \hat{\mathbf{B}}(\mathbf{r})^2\right] = \int \mathrm{d}^3 r\int_0^\infty \mathrm{d}\omega\,\omega\hat{\mathbf{f}}^\dagger(\mathbf{r},\omega)\cdot\hat{\mathbf{f}}(\mathbf{r},\omega), \tag{1.25a}$$

$$\hat{H}_{\text{mol}} = \sum_{\alpha} \omega_{\alpha} \sigma_{\alpha}^{\dagger} \sigma_{\alpha}, \tag{1.25b}$$

$$\hat{H}_{\text{int}} = -\sum_{\alpha} \hat{\mu}_{\alpha} \cdot \hat{\mathbf{E}}(\mathbf{r}_{\alpha}), \tag{1.25c}$$

in the multipolar formalism of quantum electrodynamics, in which all interactions between molecules are mediated by the electromagnetic field and are, hence, retarded. The summation index α in (1.25b) and (1.25c) ranges over all the molecules of interest, i.e. all the molecules not considered part of material bodies. The various quantities introduced in the above expressions are as follows:

- ω_{α} – transition frequency of molecule α considered as a two-level quantum mechanical system;
- $\sigma_{\alpha}^{\dagger}$ and σ_{α} – the Pauli raising and lowering operators for molecule α, defined as $\sigma_{\alpha}^{\dagger} = |e\rangle_{\alpha}\langle g|_{\alpha}$ and $\sigma_{\alpha} = |g\rangle_{\alpha}\langle e|_{\alpha}$ with $|g\rangle_{\alpha}$ and $|e\rangle_{\alpha}$ being the ground and excited states, respectively, of molecule α; these operators create or destroy an excitation on molecule α – when the molecule is viewed as a two-level system;
- $\hat{\mu}_{\alpha} = \mu_{\alpha}\sigma_{\alpha}^{\dagger} + \mu_{\alpha}^{*}\sigma_{\alpha}$ – the dipole operator of molecule α, with μ_{α} being the transition dipole moment of the molecule between its ground and (first) excited state.

The Hamiltonian in Eq. (1.24) completely describes (in the electric dipole approximation) the interaction of a system of charges (atom, molecule, etc.) with an electromagnetic field. The *spontaneous emission* of an excited molecule and the *energy transfer* between molecules are examples of such interactions. In what follows, we shall consider these two phenomena in the framework of quantum electrodynamics presented thus far.

1.2.1 Spontaneous Emission

Let us consider a single atom or molecule, modeled as a two-level quantum mechanical system, with transition frequency ω_0. We denote the ground state by $|g\rangle$ and the excited state by $|e\rangle$. In addition to the atom or molecule, it is also necessary to consider the electromagnetic field which, in this case, will be in its vacuum state, denoted by $|0\rangle$. The initial state of this system can now be written as:

$$|i\rangle = |e\rangle \otimes |0\rangle. \tag{1.26}$$

The molecule does not remain in this excited state indefinitely, but will decay to its ground state, $|g\rangle$, by emitting a photon into the electromagnetic field. This photon has a definite polarization λ and propagation direction $\mathbf{k}$ and, therefore, the new state

of the electromagnetic field can be written as $|1(\mathbf{k},\lambda)\rangle$. More generally, when not in a vacuum, the excited molecule need not emit a radiative photon. In the presence of material bodies, the molecule can transfer its excitation to a variety of medium-dressed states of the electromagnetic field, e.g. *surface* and *bulk plasmon-polaritons*, *evanescent waves*, etc. Considering expression (1.25a) for the free electromagnetic field Hamiltonian, one can write the state of the electromagnetic field which contains one excitation as $\hat{f}_i^\dagger(\mathbf{r},\omega)|0\rangle$, where the operator $\hat{f}_i^\dagger(\mathbf{r},\omega)$ acts on the vacuum state to create the medium-dressed state of the electromagnetic field as mentioned above. The final state of the system will, hence, be

$$|f\rangle = |g\rangle \otimes \hat{f}_i^\dagger(\mathbf{r},\omega)|0\rangle. \tag{1.27}$$

The aim now is to calculate the rate of transition from the initial state $|i\rangle$ to the final state $|f\rangle$. Applying time-dependent perturbation theory to this particular problem [87, p. 84], one can derive a rate for the transition $|i\rangle \longrightarrow |f\rangle$, which rate has the following expression:

$$w_{fi} = 2\pi \left|\langle f|\hat{T}|i\rangle\right|^2 \delta(\omega-\omega_0), \tag{1.28}$$

where ω_0 represents the transition frequency of the molecule and ω represents the frequency of the medium dressed electromagnetic excitations into which the molecule decays. The Dirac δ-function assures conservation of energy in this process. The $\hat{T}$ operator is the *transition operator* and is responsible for the decay of the molecule. Perturbatively, this operator can be written, to second-order in the molecule-field interaction, as

$$\hat{T} = \hat{H}_{\text{int}} + \hat{H}_{\text{int}} \frac{1}{\omega_0 - \hat{H}_0 + i\eta^+} \hat{H}_{\text{int}} \tag{1.29}$$

where $\hat{H}_0$ is the unperturbed part of the total Hamiltonian

$$\hat{H}_0 = \hat{H}_{\text{mol}} + \hat{H}_{\text{em}} = \omega_0 \sigma_0^\dagger \sigma_0 + \int \mathrm{d}^3 r \int_0^\infty \mathrm{d}\omega\, \omega\, \hat{\mathbf{f}}^\dagger(\mathbf{r},\omega)\cdot\hat{\mathbf{f}}(\mathbf{r},\omega), \tag{1.30}$$

η^+ is an infinitesimally small positive constant, and ω_0 is the energy of the initial state (in natural units). The energy of the final state is, analogously, ω and energy conservation dictates that $\omega_0 = \omega$.

In calculating the spontaneous emission rate of the molecule, only the first-order term in Eq. (1.29) has any contribution. Furthermore, because of the presence of the Dirac δ-function in the expression for the transition rate w_{fi}, Eq. (1.28), a summation over the final states $|f\rangle$ is necessary for the transition rate to be well-behaved (this is, in fact, Fermi's Golden Rule). Performing this summation, the final expression for the spontaneous emission rate of the molecule is:

$$\gamma = \sum_f w_{fi} = 2\omega_0^2 \mu_i \,\mathrm{Im}\mathscr{G}_{ij}(\mathbf{r},\mathbf{r},\omega)\mu_j, \tag{1.31}$$

where μ_i are the matrix elements of the transition dipole moments of the molecule in an orthogonal reference frame. As we mentioned before, the components of the Green's tensor $\mathscr{G}_{ij}(\mathbf{r},\mathbf{r},\omega)$ in the above expression represent the j component of the electric field at point $\mathbf{r}$, created by a point dipole source placed at point $\mathbf{r}$ and oriented along the i Cartesian coordinate. The fact that the field and source points coincide is a specific characteristic of calculations involving the decay rate of a molecule. Normally, only the real part of the Green's tensor from (1.16) exhibits a singularity when $\mathbf{r} \to \mathbf{s}$; therefore, in using the imaginary part of the Green's tensor in (1.30), we are assured of obtaining a finite result for the emission rate of the molecule.[3]

It is worth pointing out that Eq. (1.31) above can be derived equally well from a purely classical treatment of the emission process [3, 14, 28, 33], a treatment which we shall outline in Chapter 4 to justify our employing a FDTD technique for the Photonic Crystal Slab.

It is customary to express the emission rate of a molecule in inhomogeneous media in units of the free-space emission rate γ_0 of the same molecule. We define, therefore, a new quantity

$$\bar{\gamma} = \frac{\gamma}{\gamma_0}. \tag{1.32}$$

The well-known expression for γ_0, given by the Einstein A-coefficient [87], reads

$$\gamma_0 = \frac{\omega^3 \mu^2}{3\pi}. \tag{1.33}$$

This expression is easily derived from (1.31) by making use of the vacuum expression of the Green's tensor (which the reader can find at the end of this Section, Eq. (1.55)), taking the imaginary part, and only then the limit $\mathbf{r}_A \to \mathbf{r}_B$, or $R \to 0$. The normalized emission rate of the molecule is, therefore:

$$\boxed{\bar{\gamma} = \frac{6\pi}{\omega} \tilde{\mu}_i \, \mathrm{Im}\mathscr{G}_{ij}(\mathbf{r},\mathbf{r},\omega)\tilde{\mu}_j}, \tag{1.34}$$

with $\tilde{\mu}_i = \mu_i/\mu$. It is this expression that we shall use throughout this work to calculate the decay rate of an excited molecule in inhomogeneous media.

1.2.2 Energy Transfer

In this subsection we extend the formalism introduced in 1.2 to describe interactions between two molecules and the electromagnetic field, and consider the process of *resonance energy transfer*.

[3] Things are somewhat more complicated when the molecule is placed inside an absorbing medium; this will not be the case in our study. Reference [88] provides further insight into dealing with the case of a molecule embedded in an absorbing medium.

Consider, to this end, two molecules, A and B, as two-level quantum mechanical systems. Initially, molecule A is in its excited state, $|a'\rangle$, while molecule B is in its ground state $|b\rangle$.[4] As before, the electromagnetic field is in its vacuum state, $|0\rangle$. The initial state thus set up is

$$|i\rangle = |a'\rangle \otimes |b\rangle \otimes |0\rangle. \tag{1.35}$$

From this initial state, through the interaction with the electromagnetic field, the excitation of molecule A will be transfered to molecule B, achieving a final state represented by

$$|f\rangle = |a\rangle \otimes |b'\rangle \otimes |0\rangle. \tag{1.36}$$

Again, as in the case of the emission of a single molecule, one can define a rate for this transition

$$w_{fi} = 2\pi \left|\langle f|\hat{T}|i\rangle\right|^2 \delta(\omega_A - \omega_B), \tag{1.37}$$

where ω_A and ω_B are the transition frequencies of the two molecules and the transition operator is again given by (1.29). Unlike for the spontaneous emission case, the second-order term in the expansion of the transition operator will be the one that determines the transfer rate. The matrix element of this operator between the initial and final states is given by:

$$\langle f|\hat{T}|i\rangle = \sum_{|\alpha\rangle} \langle f|\hat{H}_{\text{int}} \frac{1}{E_i - \hat{H}_0 + i\eta^+} |\alpha\rangle\langle\alpha|\hat{H}_{\text{int}}|i\rangle, \tag{1.38}$$

where the complete set of intermediate states, $|\alpha\rangle$, has been introduced. These intermediate states come in two flavors:

$$|\alpha_I\rangle = |a\rangle \otimes |b\rangle \otimes \hat{f}_i^\dagger(\mathbf{s},\omega)|0\rangle, \tag{1.39a}$$

$$|\alpha_{II}\rangle = |a'\rangle \otimes |b'\rangle \otimes \hat{f}_i^\dagger(\mathbf{s},\omega)|0\rangle, \tag{1.39b}$$

and they correspond to the two physical situations depicted in the Feynman diagrams of Fig. 1.1.

Expression (1.39a) corresponds to the *direct transfer* of excitation from the excited molecule A to the unexcited one, B. Expression (1.39b), on the other hand, has a more implausible interpretation: in this second case, the intermediate photon travels backwards in time, such that in the intermediate states, both molecules are excited. Both of these processes, however, do contribute to the energy transfer, and we must sum over them to obtain the total energy transfer rate.

[4] In this subsection excited states are represented by primes over letters, to avoid confusion.

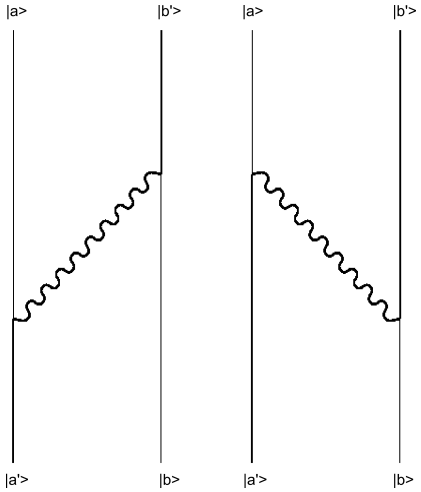

Figure 1.1: *Feynman diagrams for resonance energy transfer.*

The matrix elements of the transition operator from (1.38) now become

$$\langle f|\hat{T}|i\rangle = \sum_i \int_0^\infty \mathrm{d}\omega \int \mathrm{d}^3 s \frac{\langle a,b',0|\hat{H}_{\mathrm{int}}\hat{f}_i^\dagger(\mathbf{s},\omega)|a,b,0\rangle\langle a,b,0|\hat{f}_i(\mathbf{s},\omega)\hat{H}_{\mathrm{int}}|a',b,0\rangle}{\omega_A-\omega+i\eta}$$
$$+\sum_i \int_0^\infty \mathrm{d}\omega \int \mathrm{d}^3 s \frac{\langle a,b',0|\hat{H}_{\mathrm{int}}\hat{f}_i^\dagger(\mathbf{s},\omega)|a',b',0\rangle\langle a',b',0|\hat{f}_i(\mathbf{s},\omega)\hat{H}_{\mathrm{int}}|a',b,0\rangle}{-\omega_B-\omega+i\eta}, \quad (1.40)$$

where four type of matrix elements appear:

$$\langle a,b,0|\hat{f}_i(\mathbf{s},\omega)\hat{H}_{\mathrm{int}}|a',b,0\rangle = \frac{i}{\sqrt{\pi}}\mu_A^j\omega^2\sqrt{\varepsilon''(\mathbf{s},\omega)}\mathscr{G}_{ji}^*(\mathbf{r}_A,\mathbf{s},\omega), \quad (1.41a)$$

$$\langle a,b',0|\hat{H}_{\mathrm{int}}\hat{f}_i^\dagger(\mathbf{s},\omega)|a,b,0\rangle = -\frac{i}{\sqrt{\pi}}\mu_B^j\omega^2\sqrt{\varepsilon''(\mathbf{s},\omega)}\mathscr{G}_{ji}(\mathbf{r}_B,\mathbf{s},\omega), \quad (1.41b)$$

$$\langle a',b',0|\hat{f}_i(\mathbf{s},\omega)\hat{H}_{\mathrm{int}}|a',b,0\rangle = \frac{i}{\sqrt{\pi}}\mu_B^j\omega^2\sqrt{\varepsilon''(\mathbf{s},\omega)}\mathscr{G}_{ji}^*(\mathbf{r}_B,\mathbf{s},\omega), \quad (1.41c)$$

$$\langle a,b',0|\hat{H}_{\mathrm{int}}\hat{f}_i^\dagger(\mathbf{s},\omega)|a',b',0\rangle = -\frac{i}{\sqrt{\pi}}\mu_A^j\omega^2\sqrt{\varepsilon''(\mathbf{s},\omega)}\mathscr{G}_{ji}(\mathbf{r}_A,\mathbf{s},\omega). \quad (1.41d)$$

Using these expression in Eq. (1.40), in conjunction with the well-known fact that $\mathscr{G}_{ij}(\mathbf{r},\mathbf{s},\omega) = \mathscr{G}_{ji}(\mathbf{s},\mathbf{r},\omega)$ and the property of the Green's tensor [82, 83] that[5]

$$\mathrm{Im}\mathscr{G}_{ij}(\mathbf{r}_A,\mathbf{r}_B,\omega) = \int \mathrm{d}^3 s\, \omega^2\, \varepsilon''(\mathbf{s},\omega)\mathscr{G}_{ik}(\mathbf{r}_A,\mathbf{s},\omega)\mathscr{G}^*_{jk}(\mathbf{r}_B,\mathbf{s},\omega), \tag{1.42}$$

the matrix elements of the transition operator between the initial and final states read:

$$\langle f|\hat{T}|i\rangle = \frac{\mu_A^j \mu_B^k}{\pi} \int_0^\infty \mathrm{d}\omega\, \omega^2 \left[\frac{\mathrm{Im}\mathscr{G}_{jk}(\mathbf{r}_A,\mathbf{r}_B,\omega)}{\omega_A - \omega + i\eta} + \frac{\mathrm{Im}\mathscr{G}_{jk}(\mathbf{r}_A,\mathbf{r}_B,\omega)}{-\omega_B - \omega + i\eta} \right]. \tag{1.43}$$

This expression can be further simplified by requiring that $\omega_A = \omega_B = \omega_0$. If, in addition to this, we use the property of the Green's function that $\mathscr{G}_{ij}(\mathbf{r}_A,\mathbf{r}_B,-\omega) = \mathscr{G}^*_{ij}(\mathbf{r}_A,\mathbf{r}_B,\omega)$, and hence $\mathrm{Im}\mathscr{G}_{ij}(\mathbf{r}_A,\mathbf{r}_B,-\omega) = -\mathrm{Im}\mathscr{G}_{ij}(\mathbf{r}_A,\mathbf{r}_B,\omega)$, Eq. (1.43) then becomes

$$\langle f|\hat{T}|i\rangle = \frac{\mu_A^j \mu_B^k}{\pi} \int_{-\infty}^\infty \mathrm{d}\omega \frac{\omega^2\, \mathrm{Im}\mathscr{G}_{jk}(\mathbf{r}_A,\mathbf{r}_B,\omega)}{\omega_0 - \omega + i\,\eta\,\mathrm{sgn}\,\omega}, \tag{1.44}$$

where $\mathrm{sgn}\,\omega$ returns the sign of ω. Finally, this integral can be evaluated using contour integration and the properties of the Green's tensor in the complex-ω plane (holomorphism, to be precise) and it yields

$$\langle f|\hat{T}|i\rangle = \omega_0^2\, \mu_A^j \mathscr{G}_{jk}(\mathbf{r}_A,\mathbf{r}_B,\omega_0)\, \mu_B^k. \tag{1.45}$$

This expression, when substituted into Eq. (1.37), yields the following expression for the energy transfer rate:

$$w_{fi} = 2\pi\, |\omega_0^2\, \mu_A^j \mathscr{G}_{jk}(\mathbf{r}_A,\mathbf{r}_B,\omega_0)\, \mu_B^k|^2 \delta(\omega_A - \omega_B). \tag{1.46}$$

The ground and excited levels of the two molecules, $|a\rangle$ and $|a'\rangle$, $|b\rangle$ and $|b'\rangle$ are really electronic levels, which may have a deeper structure of vibrational levels. We turn now to these additional levels and consider the energy transfer rate between the initial and final state manifolds of the two molecules. To this end, a summation is performed over the vibrational levels of both the electronic excited state manifold of molecule A and the electronic ground state manifold of molecule B – for the initial state – as well as over the vibrational levels of the electronic ground state manifold of molecule A and the electronic excited state manifold of molecule B – for the final state. This summation gives for the total energy transfer rate the expression

$$w = \sum_{|f\rangle,|i\rangle} p_i w_{fi}, \tag{1.47}$$

[5] This equality can be derived by considering the differential equation for the Green's tensor, Eq. (1.16), and its complex conjugate, multiplying by the Green's tensor, and subtracting.

where the double summation is performed over the initial and final states and p_i denotes the *equilibrium occupation probability* of the initial state. With the inclusion of the vibrational energy levels of the two molecules into the calculations, one may use the Born-Oppenheimer approximation which allows the dipole transition matrix elements to be written as

$$\mu_A = \hat{\mathbf{d}}_A v_{a'a} \tag{1.48}$$

(with a similar decomposition for molecule B), where $\hat{\mathbf{d}}_A$ is the purely electronic transition dipole matrix element of the molecule, and $v_{a'a}$ is the overlap integral between the two vibrational states.

With this in mind, the total energy transfer rate between the two molecules A and B becomes:

$$w = 2\pi \sum_{a',a} \sum_{b,b'} p_{a'} p_b |v_{a'a} v_{bb'}|^2 |\omega_0^2 d_A^j \mathscr{G}_{jk}(\mathbf{r}_A, \mathbf{r}_B, \omega_0) d_B^k|^2. \tag{1.49}$$

In the above equation, $p_{a'}$ is the equilibrium occupation probability of vibrational level a' in the excited manifold of molecule A, and p_b is the equilibrium occupation probability of vibrational level b in the ground state manifold of molecule B. Eq. (1.49) can be simplified and reorganized somewhat in the following manner:

$$w = \int \mathrm{d}\omega \, \Gamma(\omega) \, \sigma_A^{\mathrm{em}}(\omega) \, \sigma_B^{\mathrm{abs}}(\omega), \tag{1.50}$$

where

$$\Gamma(\omega) = 2\pi\omega^4 |\mathbf{d}_A \cdot \mathscr{G}(\mathbf{r}_A, \mathbf{r}_B, \omega) \cdot \mathbf{d}_B|^2 \tag{1.51}$$

and

$$\sigma_A^{\mathrm{em}}(\omega) = \sum_{a',a} p_{a'} |v_{a'a}|^2 \delta(\omega - \omega_A), \tag{1.52a}$$

$$\sigma_B^{\mathrm{abs}}(\omega) = \sum_{b,b'} p_b |v_{bb'}|^2 \delta(\omega - \omega_B). \tag{1.52b}$$

Here $\sigma_A^{\mathrm{em}}(\omega)$ and $\sigma_B^{\mathrm{abs}}(\omega)$ can be identified as the equilibrium single-photon emission spectrum of molecule A and absorption spectrum of molecule B, respectively. If the Green's tensor is a slowly varying function of frequency, on the scale of the emission and absorption linewidths, then it can be taken approximately at the $0-0$ transition frequency ω_A of molecule A:

$$w = \Gamma(\omega_A) \int \mathrm{d}\omega \, \sigma_A^{\mathrm{em}}(\omega) \, \sigma_B^{\mathrm{abs}}(\omega). \tag{1.53}$$

The integral in the above equation is the overlap integral of the donor emission and acceptor absorption spectra appearing in Förster's celebrated theory [46]. In this thesis,

we shall assume that the conditions for (1.53) are obeyed and shall use this equation for the energy transfer rate.

As for the case of the emission rate of a molecule in a nanostructured environment, the quantity we are most interested in is the normalized energy transfer rate, i.e. the ratio between the energy transfer rate in the nanostructured environment and the energy transfer rate between the same molecules, at the same positions, but in free-space. This new quantity will be denoted by $\tilde{\Gamma}$ and it will constitute henceforth a measure of the effect of the nanostructured environment on the energy transfer rate between two molecules. Its expression is

$$\tilde{\Gamma}(\omega) = \frac{\Gamma(\omega)}{\Gamma_0(\omega)} = \frac{|\mathbf{d}_A \cdot \mathscr{G}(\mathbf{r}_A, \mathbf{r}_B, \omega) \cdot \mathbf{d}_B|^2}{|\mathbf{d}_A \cdot \mathscr{G}_0(\mathbf{r}_A, \mathbf{r}_B, \omega) \cdot \mathbf{d}_B|^2}, \tag{1.54}$$

where $\mathscr{G}_0(\mathbf{r}_A, \mathbf{r}_B, \omega)$ is the Green's tensor in free-space [89]. It has the well-known expression

$$\mathscr{G}_0^{ij}(\mathbf{r}_A, \mathbf{r}_B, \omega) = -\frac{1}{k_0^2} \frac{\mathrm{e}^{ik_0R}}{4\pi R^3} \left[(1 - ik_0R)(\delta_{ij} - 3\hat{R}_i\hat{R}_j) - k_0^2R^2(\delta_{ij} - \hat{R}_i\hat{R}_j)\right], \tag{1.55}$$

with $\mathbf{R} = \mathbf{r}_A - \mathbf{r}_B$ and $k_0 = \omega$.

1.3 The Green's Tensor in Cartesian and Cylindrical Coordinates

This section focuses on the formalism used to calculate the free-space Green's tensor in Cartesian and Cylindrical coordinates. Notwithstanding the fact that the free-space Green's tensor can be calculated in closed form (see Eq. (1.55) above), it is important to have an expansion of the Green's tensor in terms of plane-waves (or their equivalent in Cylindrical coordinates, Bessel functions) for dealing with inhomogeneous problems. For these calculations, we follow Chew [89] and omit a few of the more technical details, such as proofs of orthogonality and completeness.

1.3.1 The free-space Green's tensor in Cartesian coordinates

In order to calculate the Green's tensor in Cartesian coordinates, we start from the differential equation that it satisfies, Eq. (1.16), and we set $\varepsilon(\omega) = 1$ for vacuum. This differential equation now becomes:

$$\nabla_{\mathbf{r}} \times \nabla_{\mathbf{r}} \times \mathscr{G}(\mathbf{r}, \mathbf{s}, \omega) - \omega^2 \mathscr{G}(\mathbf{r}, \mathbf{s}, \omega) = \mathscr{I}\delta(\mathbf{r} - \mathbf{s}), \tag{1.56}$$

where we have made obvious that the differential operators act on the target variable $\mathbf{r}$ only. The goal is to find an expansion of the Green's tensor in terms of the *vector wave functions* (VWFs) in Cartesian coordinates. These VWFs are solutions of the homogeneous Helmholtz equation in Cartesian coordinates:

$$\nabla \times \nabla \times \mathbf{F}(\mathbf{k},\mathbf{r}) - k^2 \mathbf{F}(\mathbf{k},\mathbf{r}) = 0, \tag{1.57}$$

where $k^2 = k_x^2 + k_y^2 + k_z^2$ denotes the eigenvalue of the differential operator $\nabla \times \nabla \times$. Given that the Helmholtz equation is completely separable in Cartesian coordinates, one can construct the VWF solutions from the solutions of the corresponding scalar Helmholtz equation,

$$\nabla^2 \psi(\mathbf{k},\mathbf{r}) + k^2 \psi(\mathbf{k},\mathbf{r}) = 0, \tag{1.58}$$

which have a plane-wave form

$$\psi(\mathbf{k},\mathbf{r}) = \mathrm{e}^{i\mathbf{k}\cdot\mathbf{r}}, \tag{1.59}$$

as follows:

$$\mathbf{M}(\mathbf{k},\mathbf{r}) = \nabla \times [\psi(\mathbf{k},\mathbf{r})\hat{z}] = i\,(\mathbf{k}\times\hat{z})\,\mathrm{e}^{i\mathbf{k}\cdot\mathbf{r}}, \tag{1.60a}$$

$$\mathbf{N}(\mathbf{k},\mathbf{r}) = \frac{1}{k}\nabla \times \nabla \times [\psi(\mathbf{k},\mathbf{r})\hat{z}] = -\frac{1}{k}\mathbf{k}\times(\mathbf{k}\times\hat{z})\,\mathrm{e}^{i\mathbf{k}\cdot\mathbf{r}}, \tag{1.60b}$$

$$\mathbf{L}(\mathbf{k},\mathbf{r}) = \nabla\psi(\mathbf{k},\mathbf{r}) = i\mathbf{k}\mathrm{e}^{i\mathbf{k}\cdot\mathbf{r}}. \tag{1.60c}$$

It can be shown that these VWFs form an orthogonal and complete set of eigenfunctions [89], which means that one can expand the Green's tensor on the basis that they form as follows:

$$\mathscr{G}(\mathbf{r},\mathbf{s},\omega) = \int \mathrm{d}^3k\,[\mathbf{M}(\mathbf{k},\mathbf{r})\mathbf{m}(\mathbf{k},\mathbf{s}) + \mathbf{N}(\mathbf{k},\mathbf{r})\mathbf{n}(\mathbf{k},\mathbf{s}) + \mathbf{L}(\mathbf{k},\mathbf{r})\mathbf{l}(\mathbf{k},\mathbf{s})]\,. \tag{1.61}$$

The unknown coefficients $\mathbf{m}(\mathbf{k},\mathbf{s})$, $\mathbf{n}(\mathbf{k},\mathbf{s})$ and $\mathbf{l}(\mathbf{k},\mathbf{s})$ can be calculated by inserting the expression for the Green's tensor from Eq. (1.61) into the differential equation Eq. (1.56) and using the orthogonality and completeness of the VWFs [89]. We obtain

$$\begin{gathered}\mathbf{m}(\mathbf{k},\mathbf{s}) = \frac{1}{(2\pi)^3}\frac{\mathbf{M}^*(\mathbf{k},\mathbf{s})}{k_\rho^2(k^2-\omega^2)}, \quad \mathbf{n}(\mathbf{k},\mathbf{s}) = \frac{1}{(2\pi)^3}\frac{\mathbf{N}^*(\mathbf{k},\mathbf{s})}{k_\rho^2(k^2-\omega^2)}, \\ \mathbf{l}(\mathbf{k},\mathbf{s}) = -\frac{1}{(2\pi)^3}\frac{\mathbf{L}^*(\mathbf{k},\mathbf{s})}{\omega^2 k^2},\end{gathered} \tag{1.62}$$

from which the Green's tensor can now be written as:

$$\mathscr{G}(\mathbf{r},\mathbf{s},\omega) = \frac{1}{(2\pi)^3}\int \mathrm{d}^3k \left[\frac{\mathbf{M}(\mathbf{k},\mathbf{r})\mathbf{M}^*(\mathbf{k},\mathbf{s})}{k_\rho^2(k^2-\omega^2)} + \frac{\mathbf{N}(\mathbf{k},\mathbf{r})\mathbf{N}^*(\mathbf{k},\mathbf{s})}{k_\rho^2(k^2-\omega^2)} - \frac{\mathbf{L}(\mathbf{k},\mathbf{r})\mathbf{L}^*(\mathbf{k},\mathbf{s})}{k^2\omega^2}\right], \tag{1.63}$$

where $k_\rho^2 = k_x^2 + k_y^2$. This expression for the Green's tensor can be further simplified by performing the integration in the complex k_z plane. The details of this integration are not very involved and are covered extensively in [89], so we will only sketch them here. Each of the three terms under the integral sign in Eq. (1.63) has a number of poles in the complex k_z plane. The **M**-term has poles at $k_z = \pm\sqrt{\omega^2 - k_\rho^2}$, whose contribution to the integral can be easily extracted. The **N**-term also has poles at $k_z = \pm\sqrt{\omega^2 - k_\rho^2}$, as well as static poles at $k_z = \pm ik_\rho$ (appearing because of the $1/k$ factor in Eq. (1.60b)). The contribution of these static poles is exactly canceled by the contribution of the poles coming from the last term in Eq. (1.63), involving the **L**-term. We are, hence, left with a two-dimensional integral for the Green's tensor, which now takes the form

$$\mathscr{G}(\mathbf{r},\mathbf{s},\omega) = -\frac{\delta(\mathbf{r}-\mathbf{s})}{\omega^2}\hat{\mathbf{z}}\hat{\mathbf{z}} + \frac{i}{8\pi^2}\int \mathrm{d}^2k_\rho \frac{1}{k_z k_\rho^2}\left[\mathbf{M}(\mathbf{k}_\rho,\pm k_z,\mathbf{r})\mathbf{M}^*(\mathbf{k}_\rho,\pm k_z,\mathbf{s}) + \right.$$
$$\left. + \mathbf{N}(\mathbf{k}_\rho,\pm k_z,\mathbf{r})\mathbf{N}^*(\mathbf{k}_\rho,\pm k_z,\mathbf{s})\right], \qquad z \gtrless z_s, \tag{1.64}$$

where z_s is the z-component of the source position vector $\mathbf{s}$. The δ-singularity in the Green's tensor, originating from the integral of the **L**-term and contributing only to the real part of the Green's tensor, is an illustration of the self-field of a dipolar current density. As the Green's tensor in a homogeneous medium can also be calculated in closed form, the presence of this singularity does not pose any numerical problem in calculations and we will have no need to consider it from now on.

An example: The Green's tensor in a half-space geometry

As an illustration of the method we shall use throughout this thesis, a method put forward in [89] and [90], we shall present the calculations for the Green's tensor in a geometry consisting of two half-spaces with different dielectric properties separated by an infinite planar surface of discontinuity (see Fig. 1.2). Known as *the method of scattering superposition*, the idea behind this method is that the Green's tensor in any geometry can be split into two parts as follows:

$$\mathscr{G}(\mathbf{r},\mathbf{s},\omega) = \mathscr{G}_h(\mathbf{r},\mathbf{s},\omega) + \mathscr{G}_s(\mathbf{r},\mathbf{s},\omega), \tag{1.65}$$

where the first term, $\mathscr{G}_h(\mathbf{r},\mathbf{s},\omega)$, is known as the *homogeneous* term and it accounts for the direct path between the source and target points, $\mathbf{s}$ and $\mathbf{r}$, i.e. when the two points are in the same medium, and are not separated by any surface of discontinuity. When the source and target points are in different media, the homogeneous term is null, and the Green's tensor reduces to the always present second term in the above expression, the *scattering* term, $\mathscr{G}_s(\mathbf{r},\mathbf{s},\omega)$. All the scattering properties of the different bodies

Figure 1.2: *Geometry of two half-spaces.*

present in the geometry under consideration are embodied in the scattering term and we shall outline its derivation for the case of the half-space geometry in what follows. Being that we are dealing with a planar interface between the two half-spaces, Cartesian coordinates are a natural choice and so we start with the expansion of the Green's tensor in terms of the VWFs in Cartesian coordinates, Eq. (1.64). Because the VWFs form a complete and orthogonal set of eigenfunctions, one can expand the scattering term in Eq. (1.65) in terms of the VWFs as well. We distinguish two different physical situations, depending on the position of the source point, **s**, as follows: (a) the source point is in medium 1, above the interface and (b) the source point is in medium 2, below the interface. Furthermore, for each of these two cases, the target point **r** can also be in either medium 1 or medium 2. We are thus led to four distinct expressions for the scattering part of the Green's tensor, which are:

$$\mathscr{G}_s^{(11)}(\mathbf{r},\mathbf{s},\omega) = \frac{i}{8\pi^2}\int \mathrm{d}^2 k_\rho \frac{1}{k_{z1}k_\rho^2}\Big[R_M^{+(11)-}\mathbf{M}(\mathbf{k}_\rho,k_{z1},\mathbf{r})\mathbf{M}^*(\mathbf{k}_\rho,-k_{z1},\mathbf{s}) + \\ + R_N^{+(11)-}\mathbf{N}(\mathbf{k}_\rho,k_{z1},\mathbf{r})\mathbf{N}^*(\mathbf{k}_\rho,-k_{z1},\mathbf{s})\Big], \tag{1.66a}$$

$$\mathscr{G}_s^{(21)}(\mathbf{r},\mathbf{s},\omega) = \frac{i}{8\pi^2}\int \mathrm{d}^2 k_\rho \frac{1}{k_{z1}k_\rho^2}\Big[R_M^{-(21)-}\mathbf{M}(\mathbf{k}_\rho,-k_{z2},\mathbf{r})\mathbf{M}^*(\mathbf{k}_\rho,-k_{z1},\mathbf{s}) + \\ + R_N^{-(21)-}\mathbf{N}(\mathbf{k}_\rho,-k_{z2},\mathbf{r})\mathbf{N}^*(\mathbf{k}_\rho,-k_{z1},\mathbf{s})\Big], \tag{1.66b}$$

$$\mathscr{G}_s^{(12)}(\mathbf{r},\mathbf{s},\omega) = \frac{i}{8\pi^2}\int \mathrm{d}^2k_\rho \frac{1}{k_{z2}k_\rho^2}\Big[R_M^{+(12)+}\mathbf{M}(\mathbf{k}_\rho,k_{z1},\mathbf{r})\mathbf{M}^*(\mathbf{k}_\rho,k_{z2},\mathbf{s}) + \\ + R_N^{+(12)+}\mathbf{N}(\mathbf{k}_\rho,k_{z1},\mathbf{r})\mathbf{N}^*(\mathbf{k}_\rho,k_{z2},\mathbf{s})\Big], \tag{1.66c}$$

$$\mathscr{G}_s^{(22)}(\mathbf{r},\mathbf{s},\omega) = \frac{i}{8\pi^2}\int \mathrm{d}^2k_\rho \frac{1}{k_{z2}k_\rho^2}\Big[R_M^{-(22)+}\mathbf{M}(\mathbf{k}_\rho,-k_{z2},\mathbf{r})\mathbf{M}^*(\mathbf{k}_\rho,k_{z2},\mathbf{s}) + \\ + R_N^{-(22)+}\mathbf{N}(\mathbf{k}_\rho,-k_{z2},\mathbf{r})\mathbf{N}^*(\mathbf{k}_\rho,k_{z2},\mathbf{s})\Big]. \tag{1.66d}$$

Each one of the four above expressions has the general form of Eq. (1.64), and we will now discuss the differences. All four scattering terms are distinguished amongst themselves by the use of two numeric superscripts, (ij), with $i = 1,2$ and $j = 1,2$. The first superscript denotes the medium in which the target point $\mathbf{r}$ is located, while the second superscript denotes the medium in which the source point $\mathbf{s}$ is located. The additional subscript on the z-component of the wavevector, k_{zi}, with $i = 1,2$ serves the same function. Finally, the R-coefficients are the usual Fresnel coefficients for reflection and transmission at the interface between two media and we will derive them in what follows. The subscripts (M and N) denote the polarization, which is decoupled in this geometry, i.e. there only exist pure *transverse magnetic* (TM) or *transverse electric* (TE) modes, and no hybrids. The rather lengthy superscripts on these coefficients are best explained through an illustration: $R_N^{+(12)+}$ denotes the Fresnel coefficient for the transmission from medium 2 into medium 1, in which case the propagation at the source point is in the positive z-direction and the propagation at the target point is also in the z-direction. Although the $\pm$ superscripts may be redundant in this simple case (the radiation condition makes the coefficients uniquely determined by the (ij) superscripts), they will play a role further on when there is more than one surface of discontinuity.

We turn now to calculating the R-coefficients for this simple geometry. In order to do so, one must impose boundary and continuity conditions on the Green's tensor and derive the R-coefficients from these constraints. We have already hinted at one boundary condition in the above paragraph, namely the radiation condition. This condition ensures that there are no incoming waves from either $z \to \infty$ or from $z \to -\infty$, as there are no scatterers present other than the interface at $z = 0$ and, hence, no source for these incoming waves. As we have mentioned, this condition is already taken into account in the expressions in (1.66) and we will not consider it anymore. This leaves the continuity conditions at the interface $z = 0$. Continuity of the tangential component of the electric field $\mathbf{E}$ and the normal component of the magnetic field $\mathbf{B}$ translates into the following conditions in terms of the Green's tensor:

$$\hat{\mathbf{z}} \times \Big[\mathscr{G}^{(1i)}(\mathbf{r},\mathbf{s},\omega) - \mathscr{G}^{(2i)}(\mathbf{r},\mathbf{s},\omega)\Big]\Big|_{z=0} = 0, \tag{1.67a}$$

$$\hat{\mathbf{z}} \times \left[\nabla_{\mathbf{r}} \times \mathscr{G}^{(1i)}(\mathbf{r},\mathbf{s},\omega) - \nabla_{\mathbf{r}} \times \mathscr{G}^{(2i)}(\mathbf{r},\mathbf{s},\omega) \right] \Big|_{z=0} = 0, \tag{1.67b}$$

where the superscript i indicates that the continuity conditions have the same functional form, for the source point $\mathbf{s}$ located in either medium. One must note that the above conditions involve the total Green's tensor $\mathscr{G}(\mathbf{r},\mathbf{s},\omega)$ and not only the scattering part, $\mathscr{G}_s(\mathbf{r},\mathbf{s},\omega)$. As such the continuity equations lead to an *inhomogeneous* system of linear equations, in the unknowns R, with free-terms given by the homogeneous part of the Green's tensor, $\mathscr{G}_h(\mathbf{r},\mathbf{s},\omega)$. The characteristic matrices of this system, for the two polarizations, TE and TM, have the form:

$$\Delta_M = \begin{pmatrix} 1 & -1 \\ k_{z1} & k_{z2} \end{pmatrix}, \qquad \Delta_N = \begin{pmatrix} \dfrac{k_{z1}}{k_1} & \dfrac{k_{z2}}{k_2} \\ k_1 & -k_2 \end{pmatrix}, \tag{1.68}$$

while the unknown coefficient vectors are

$$\mathbf{R}_M^{(i)} = \begin{pmatrix} R_M^{+(1i)} \\ R_M^{-(2i)} \end{pmatrix}, \qquad \mathbf{R}_N^{(i)} = \begin{pmatrix} R_N^{+(1i)} \\ R_N^{-(2i)} \end{pmatrix}. \tag{1.69}$$

Finally, the free-term vectors are

$$\mathbf{V}_M^{(1)} = \begin{pmatrix} -1 \\ k_{z1} \end{pmatrix}, \quad \mathbf{V}_N^{(1)} = \begin{pmatrix} \dfrac{k_{z1}}{k_1} \\ -k_1 \end{pmatrix}, \quad \mathbf{V}_M^{(2)} = \begin{pmatrix} 1 \\ k_{z2} \end{pmatrix}, \quad \mathbf{V}_N^{(2)} = \begin{pmatrix} \dfrac{k_{z2}}{k_2} \\ k_2 \end{pmatrix}. \tag{1.70}$$

The continuity conditions (1.67) can now be written in matrix form as

$$\Delta_{M(N)} \cdot \mathbf{R}_{M(N)}^{(i)} = \mathbf{V}_{M(N)}^{(i)}, \tag{1.71}$$

leading to the following expressions for the Fresnel coefficients:

$$R_M^{+(11)-} = \frac{k_{z1} - k_{z2}}{k_{z1} + k_{z2}}, \quad R_M^{-(21)-} = \frac{2k_{z1}}{k_{z1} + k_{z2}}, \tag{1.72a}$$

$$R_M^{+(12)+} = \frac{2k_{z2}}{k_{z2} + k_{z1}}, \quad R_M^{-(22)+} = \frac{k_{z2} - k_{z1}}{k_{z2} + k_{z1}}, \tag{1.72b}$$

$$R_N^{+(11)-} = \frac{\varepsilon_2 k_{z1} - \varepsilon_1 k_{z2}}{\varepsilon_2 k_{z1} + \varepsilon_1 k_{z2}}, \quad R_N^{-(21)-} = \frac{2\sqrt{\varepsilon_1}\sqrt{\varepsilon_2} k_{z1}}{\varepsilon_2 k_{z1} + \varepsilon_1 k_{z2}}, \tag{1.72c}$$

$$R_N^{+(12)+} = \frac{2\sqrt{\varepsilon_1}\sqrt{\varepsilon_2} k_{z2}}{\varepsilon_1 k_{z2} + \varepsilon_2 k_{z1}}, \quad R_N^{-(22)+} = \frac{\varepsilon_1 k_{z2} - \varepsilon_2 k_{z1}}{\varepsilon_1 k_{z2} + \varepsilon_2 k_{z1}}. \tag{1.72d}$$

Having derived the above expressions for the unknown coefficients in the Green's tensor expansions (1.66), one can go on and further simplify these expansions by switching to polar coordinates in the $\mathbf{k}_\rho$-plane, $\mathbf{k}_\rho = (k_\rho, k_\theta)$, and performing the k_θ integral analytically. This can be done since, as seen from Eqs. (1.72), the R-coefficients depend only on the radial, but not on the angular polar coordinate of $\mathbf{k}_\rho$. We shall give, as an example, the final expression for a single component of the scattered part of the Green's tensor, namely the zz-component, for the particular situation when the source point is in medium 1 and the target point is in medium 2, i.e. $\mathscr{G}_{zz}^{(21)}(\mathbf{r},\mathbf{s},\omega)$. This expression reads

$$\mathscr{G}_{zz}^{(21)}(\mathbf{r},\mathbf{s},\omega) = \frac{i}{4\pi}\int_0^\infty \mathrm{d}k_\rho \frac{k_\rho^3}{k_{z1}k_1k_2} R_N^{-(21)-} J_0(k_\rho|\rho-\rho_s|)\,\mathrm{e}^{-i(k_{z2}z-k_{z1}z_s)}, \tag{1.73}$$

where J_0 is the regular Bessel function of zero order and $\mathbf{r} = (\rho, z)$ and $\mathbf{s} = (\rho_s, z_s)$. This remaining integral cannot be performed analytically and must be calculated numerically.

This simple example illustrates the method of scattering superposition which we will use throughout this thesis and we will have occasion to refer to this subsection in the following chapters.

1.3.2 The free-space Green's tensor in Cylindrical coordinates

In order to calculate the Green's tensor in Cylindrical coordinates we start, once again, with the differential equation for the Green's tensor, Eq. (1.56). The vector Helmholtz equation that the VWFs satisfy is now the same as Eq. (1.57), but the corresponding scalar Helmholtz equation Eq. (1.58) can be explicitly written in Cylindrical coordinates as

$$\left(\frac{\partial^2}{\partial\rho^2} + \frac{1}{\rho}\frac{\partial}{\partial\rho} + \frac{1}{\rho^2}\frac{\partial^2}{\partial\theta^2} + \frac{\partial^2}{\partial z^2} + k^2\right)\psi(\mathbf{k},\mathbf{r}) = 0, \tag{1.74}$$

where $\mathbf{r} = (r,\theta,z)$ in Cylindrical coordinates. The solutions to this equation are

$$\psi_n(k_\rho,k_z,\mathbf{r}) = J_n(k_\rho\rho)\mathrm{e}^{in\theta}\mathrm{e}^{ik_z z}, \tag{1.75}$$

with $J_n(k_\rho\rho)$ being the regular Bessel functions of first kind and integer order n, which are regular at the origin. The VWFs solutions of Eq. (1.57) can be derived from this scalar solution, in a manner completely analogous to the case for Cartesian coordinates (hence the use of an equivalent notation), as:

$$\begin{aligned}\mathbf{M}_n(k_\rho,k_z,\mathbf{r}) &= \nabla\times\left[\psi_n(k_\rho,k_z,\mathbf{r})\right] \\ &= \left[\frac{in}{\rho}J_n(k_\rho\rho)\hat{\rho} - \frac{\partial J_n(k_\rho\rho)}{\partial\rho}\hat{\theta}\right]\mathrm{e}^{in\theta}\mathrm{e}^{ik_z z},\end{aligned} \tag{1.76a}$$

$$\begin{aligned}\mathbf{N}_n(k_\rho,k_z,\mathbf{r}) &= \frac{1}{k}\nabla\times\nabla\times\left[\psi_n(k_\rho,k_z,\mathbf{r})\right]\\ &= \frac{1}{k}\left[ik_z\frac{\partial J_n(k_\rho\rho)}{\partial\rho}\hat{\boldsymbol{\rho}} - \frac{nk_z}{\rho}J_n(k_\rho\rho)\hat{\boldsymbol{\theta}} + k_\rho^2 J_n(k_\rho\rho)\hat{\mathbf{z}}\right]\mathrm{e}^{in\theta}\mathrm{e}^{ik_z z}, \quad (1.76b)\end{aligned}$$

$$\begin{aligned}\mathbf{L}_n(k_\rho,k_z,\mathbf{r}) &= \nabla\left[\psi_n(k_\rho,k_z,\mathbf{r})\right]\\ &= \left[\frac{\partial J_n(k_\rho\rho)}{\partial\rho}\hat{\boldsymbol{\rho}} + \frac{in}{\rho}J_n(k_\rho\rho)\hat{\boldsymbol{\theta}} + ik_z J_n(k_\rho\rho)\hat{\mathbf{z}}\right]\mathrm{e}^{in\theta}\mathrm{e}^{ik_z z}. \quad (1.76c)\end{aligned}$$

These VWFs once again form an orthogonal and complete set [89], which leads to the following expansion of the Green's tensor:

$$\begin{aligned}\mathscr{G}(\mathbf{r},\mathbf{s},\omega) = \sum_{n=-\infty}^{\infty}\int_0^\infty \mathrm{d}k_\rho \int_{-\infty}^{\infty}\mathrm{d}k_z \big[&\mathbf{M}_n(k_\rho,k_z,\mathbf{r})\mathbf{m}_n(k_\rho,k_z,\mathbf{s}) +\\ &+\mathbf{N}_n(k_\rho,k_z,\mathbf{r})\mathbf{n}_n(k_\rho,k_z,\mathbf{s}) + \mathbf{L}_n(k_\rho,k_z,\mathbf{r})\mathbf{l}_n(k_\rho,k_z,\mathbf{s})\big], \quad (1.77)\end{aligned}$$

where the unknown coefficients $\mathbf{m}_n(k_\rho,k_z,\mathbf{s})$, $\mathbf{n}_n(k_\rho,k_z,\mathbf{s})$ and $\mathbf{l}_n(k_\rho,k_z,\mathbf{s})$ can again be calculated to yield

$$\begin{aligned}\mathbf{m}_n(k_\rho,k_z,\mathbf{s}) = \frac{1}{(2\pi)^2}\frac{\mathbf{M}_n^*(k_\rho,k_z,\mathbf{s})}{k_\rho(k^2-\omega^2)}, \quad \mathbf{n}_n(k_\rho,k_z,\mathbf{s}) = \frac{1}{(2\pi)^2}\frac{\mathbf{N}_n^*(k_\rho,k_z,\mathbf{s})}{k_\rho(k^2-\omega^2)}\\ \mathbf{l}_n(k_\rho,k_z,\mathbf{s}) = -\frac{1}{(2\pi)^2}\frac{k_\rho}{k^2}\frac{\mathbf{L}_n^*(k_\rho,k_z,\mathbf{s})}{\omega^2}.\end{aligned} \quad (1.78)$$

The expansion (1.77) of the Green's tensor then becomes

$$\begin{aligned}\mathscr{G}(\mathbf{r},\mathbf{s},\omega) = \frac{1}{(2\pi)^2}\sum_{n=-\infty}^{\infty}\int_0^\infty \mathrm{d}k_\rho\, k_\rho \int_{-\infty}^{\infty}\mathrm{d}k_z \Bigg[&\frac{\mathbf{M}_n(k_\rho,k_z,\mathbf{r})\mathbf{M}_n^*(k_\rho,k_z,\mathbf{s})}{k_\rho^2(k^2-\omega^2)} +\\ &+\frac{\mathbf{N}_n(k_\rho,k_z,\mathbf{r})\mathbf{N}_n^*(k_\rho,k_z,\mathbf{s})}{k_\rho^2(k^2-\omega^2)} - \frac{\mathbf{L}_n(k_\rho,k_z,\mathbf{r})\mathbf{L}_n^*(k_\rho,k_z,\mathbf{s})}{k^2\omega^2}\Bigg], \quad (1.79)\end{aligned}$$

an expression that can be further simplified by performing the k_ρ integral analytically in the complex k_ρ plane, thus extracting the pole contributions. The final expression

for the Green's tensor now becomes

$$\mathscr{G}(\mathbf{r},\mathbf{s},\omega) = -\frac{\delta(\mathbf{r}-\mathbf{s})}{\omega^2}\hat{\rho}\hat{\rho} + \frac{i}{8\pi}\sum_{n=-\infty}^{\infty}\int_{-\infty}^{\infty} \mathrm{d}k_z \frac{1}{k_\rho^2} \times$$
$$\times \begin{cases} \mathbf{M}_n^{(1)}(k_\rho,k_z,\mathbf{r})\mathbf{M}_n^*(k_\rho,k_z,\mathbf{s}) + \mathbf{N}_n^{(1)}(k_\rho,k_z,\mathbf{r})\mathbf{N}_n^*(k_\rho,k_z,\mathbf{s}), & \rho > \rho_s \\ \mathbf{M}_n(k_\rho,k_z,\mathbf{r})\mathbf{M}_n^{(1)*}(k_\rho,k_z,\mathbf{s}) + \mathbf{N}_n(k_\rho,k_z,\mathbf{r})\mathbf{N}_n^{(1)*}(k_\rho,k_z,\mathbf{s}), & \rho < \rho_s \end{cases} . \quad (1.80)$$

The superscript (1) on the VWFs in the above expression denotes that we should replace the regular Bessel functions $J_n(k_\rho\rho)$ in them with the Hankel function of first kind, $H_n(k_\rho\rho)$. This is to ensure that the radiation condition as $\rho \to \infty$ is satisfied.

1.4 An Introduction to Surface Plasmon-Polaritons

Throughout the investigations into the intermolecular or radiation-matter interactions presented in this thesis, we shall often focus on a particularly important class of electromagnetic modes, the so-called *surface plasmon-polaritons* (SPPs). In this section we shall give a very brief introduction to surface plasmons, with an illustration of SPPs on a single planar interface.

1.4.1 General introduction to surface plasmon-polaritons

Surface plasmons represent collective oscillations of the free electrons that are found in a metal; as the name suggests, these oscillations occur at the interface between a metal and a dielectric material. The main characteristic distinguishing SPPs from other electromagnetic modes is their spatial dependence. Due to their confinement to the interface or surface, SPPs decay exponentially away from and are, therefore, guided by the surface.

1.4.2 Surface plasmon-polaritons on a single planar interface

The simplest example of a geometry that supports surface plasmons is the planar interface between two half-spaces: a dielectric and a metal. In the present subsection this example is studied in some detail, as it is the starting point for understanding SPPs in planar multilayered and even cylindrical geometries.

Consider two semi-infinite regions – half-spaces – separated by an infinite planar interface in the xOy plane at $z = 0$. The region with $z > 0$ is filled up by a material with dielectric constant ε_d, while the region with $z < 0$ is filled up with a metal, having

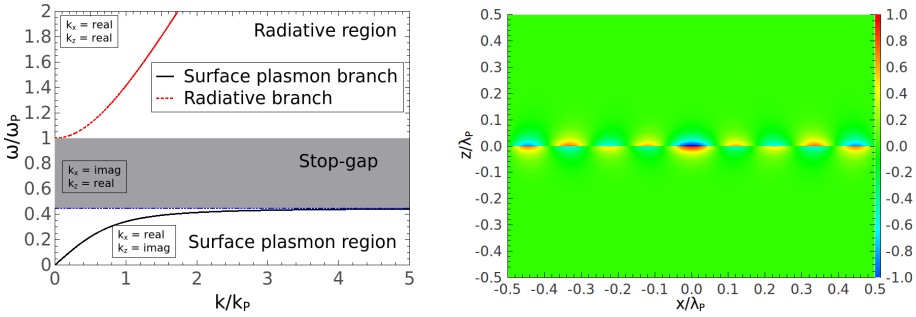

(a) *Dispersion of SPPs* **(b)** *Electric field of SPPs*

Figure 1.3: *Band structure (a) and electric field (b) of SPPs in a single-interface geometry between a dielectric with $\varepsilon_d = 4$ and a lossless Drude metal. The electric field is calculated at $\omega = 0.44\,\omega_P$; $\lambda_P = 2\pi/\omega_P$ is the wavelength corresponding to the plasma frequency ω_P.*

a frequency-dependent complex permittivity, $\varepsilon_m(\omega)$. In this thesis we use a Drude model for the permittivity of the metal:

$$\varepsilon_m(\omega) = 1 - \frac{\omega_P^2}{\omega(\omega + i\gamma)}, \tag{1.81}$$

with ω_P being the plasma frequency of the metal, and γ the linewidth, which accounts for ohmic losses in the metal. The conditions for the existence of SPPs can be derived from Maxwell's equations and the continuity conditions across the metal/dielectric interface, supplemented with the requirement that the electric field should decay exponentially away from the interface. As we have already analyzed the single interface geometry through the Green's tensor, we shall now derive the dispersion relations for SPPs on a single interface by employing the appropriate Green's tensor. We will start this subsection by disregarding the ohmic losses in the metal, setting $\gamma = 0$. Later, we shall discuss the role that these loses play and how they influence the behavior of the SPPs.

The electromagnetic field in a single planar interface geometry is completely described by the Green's tensor from Eq. (1.65) and Eqs. (1.66). The continuity conditions across the interface give rise to an inhomogeneous system of linear equations, encapsulated in the matrix equation (1.71). SPPs, as well as other electromagnetic modes are obtained by requiring that the characteristic matrix of the system, $\Delta_{M(N)}$ be singular, i.e. $\det(\Delta_{M(N)}) = 0$. This leads to the following two expressions:

$$\det(\Delta_M) = k_z^d + k_z^m = 0, \tag{1.82a}$$

$$\det(\Delta_N) \propto \varepsilon_m k_z^d + \varepsilon_d k_z^m = 0, \tag{1.82b}$$

of which only the second one, corresponding to TM modes, is interesting for SPPs. Considering that the propagation constants in the z-direction, k_z^d and k_z^m, are given by $k_z^d = \sqrt{k_d^2 - k_\rho^2}$ and $k_z^m = \sqrt{k_m^2 - k_\rho^2}$, expression (1.82b) above after some manipulations becomes

$$k_\rho = \omega \sqrt{\frac{\varepsilon_d \varepsilon_m}{\varepsilon_d + \varepsilon_m}}, \tag{1.83}$$

which constitutes a dispersion relation, i.e. $\omega = \omega(k)$. The propagation constants along the z-direction in the two media are given by

$$k_z^d = \omega \sqrt{\frac{\varepsilon_d^2}{\varepsilon_d + \varepsilon_m}}, \qquad k_z^m = \omega \sqrt{\frac{\varepsilon_m^2}{\varepsilon_d + \varepsilon_m}}. \tag{1.84}$$

The conditions for the existence of SPPs can be summarized as follows: they propagate along the interface, i.e. k_ρ is real, and they decay exponentially away from the interface, i.e. k_z^d and k_z^m are imaginary. Using expression (1.81) for the dielectric permittivity of the metal – with $\gamma = 0$ – the conditions for the existence of SPPs can be written as a constraint on their frequency as follows:

$$\omega \in (0, \omega_{\mathrm{SP}}), \tag{1.85}$$

where ω_{SP} is the *surface plasmon frequency*, defined as $\omega_{\mathrm{SP}} \equiv \dfrac{\omega_{\mathrm{P}}}{\sqrt{1+\varepsilon_d}}$. Figure 1.3a shows the dispersion relation of electromagnetic modes in a single interface geometry, with $\varepsilon_d = 4$, $\gamma = 0$ and k_P the wavenumber corresponding to the plasma frequency ω_{P}. The surface plasmon frequency in this case is $\omega_{\mathrm{SP}} = \omega_{\mathrm{P}}/\sqrt{5} \approx 0.447\,\omega_{\mathrm{P}}$. The different frequency regions are clearly delineated: the region $\omega \in (0, \omega_{\mathrm{SP}})$ can support SPPs, whose dispersion curve lies beneath the light-line in the dielectric; the region $\omega \in (\omega_{\mathrm{SP}}, \omega_{\mathrm{P}})$, denoted as the *stop-gap* region in Fig. 1.3a, does not support any electromagnetic modes, while in the region $\omega \in (\omega_{\mathrm{P}}, \infty)$ all modes are radiative, propagating freely both in the dielectric and in the metal.

The electric field distribution of a SPP in the single-interface geometry with the same parameters used in Fig. 1.3a is shown schematically in Fig. 1.3b at a frequency $\omega = 0.44\,\omega_{\mathrm{P}}$.

We have thus far neglected ohmic losses in the metal, by setting $\gamma = 0$. We shall now consider the effect of a finite linewidth on the behavior of SPPs in a single-interface geometry. Since the dielectric permittivity of the metal from (1.81) is no longer a purely real quantity, the propagation constant along the interface, k_ρ, acquires an imaginary component as well, even in the frequency interval $\omega \in (0, \omega_{\mathrm{SP}})$. It can thus be written $k_\rho = k'_\rho + ik''_\rho$ and the imaginary part leads to damping of the SPP

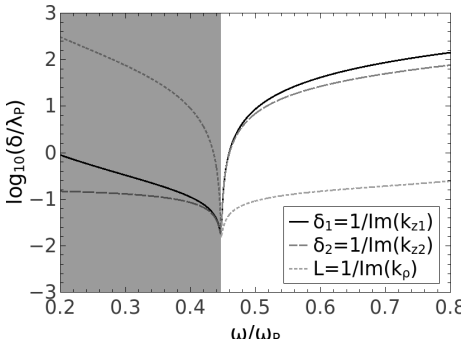

Figure 1.4: *Frequency-dependence of the penetration depths of SPPs in the dielectric and metal, δ_1 and δ_2, respectively, as well as of the propagation length L. The geometry is that of a single interface between a dielectric with $\varepsilon = 4$ and a lossy Drude metal with $\gamma = 2.288 \cdot 10^{-3}\,\omega_P$. The shaded region represents the SPP frequency region, $0 < \omega < \omega_{SP}$.*

as it propagates along the interface. Conversely, the propagation constants in the z-direction, $k_z^{d,m}$, acquire a real component, which leads to a weaker confinement of the SPP to the interface. One can now define two penetration depths inside the dielectric and metal, δ_1 and δ_2 respectively, as well as a propagation length of the SPP along the interface, L, as follows:

$$\delta_1 = \frac{1}{k''_{zd}}, \quad \delta_2 = \frac{1}{k''_{zm}}, \quad \text{and} \quad L = \frac{1}{k''_{\rho}}, \tag{1.86}$$

where the double primes signify the imaginary part of the respective components of the wavevector.

Fig. 1.4 shows the frequency dependence of these quantities for $\gamma = 2.28 \cdot 10^{-3}\,\omega_{\mathrm{P}}$ (this linewidth or collision frequency corresponds to a Drude model for silver, and we shall make use of it later in this work). In the SPP frequency region, $0 < \omega < \omega_{\mathrm{SP}}$, the SPP is confined stronger on the metal side of the interface than on the dielectric side. The propagation length along the interface also becomes finite. For this value of γ which corresponds to silver in the optical frequency region, the effect of γ on the the dispersion curve of the SPP is small enough not to alter it significantly, even near the surface plasmon frequency, ω_{SP}. A finite linewidth can, however, significantly influence the electromagnetic properties of molecules placed near the interface, as we shall see in the next chapters.

Surface plasmon-polaritons can also exist in more complex geometries, and we shall investigate them later on, referring back to this section as a model.

CHAPTER 2

Metallic Slab and Planar Waveguide

Abstract

In this chapter we investigate the spontaneous emission rate of a molecule and the energy transfer rate between two molecules placed in two types of layered geometries: a metallic slab in a dielectric host medium and a planar waveguide. We focus especially on the role played by surface plasmon-polaritons in modifying the spontaneous emission and energy transfer rates as compared to free-space. In the presence of more than one interface, the surface plasmon-polariton modes split into several branches, and each branch can contribute significantly to modifying the electromagnetic properties of atoms and molecules. Enhancements of several orders of magnitude both in the spontaneous emission rate of a molecule and the energy transfer rate between molecules are obtained and, by tuning the parameters of the geometry, one has the ability to control the range and magnitude of these enhancements. For the energy transfer rate interference effects between contributions of different plasmon-polariton branches are observed as oscillations in the distance dependence of this rate.

Published as *Phys. Rev. A*, **84**, 053824, 2011

2.1 Introduction

In this chapter we investigate the role played by surface plasmon-polaritons in modifying the decay rate of a molecule and the energy transfer rate between two molecules placed inside two types of multilayered structures: a metal slab in a dielectric host and a planar waveguide. The planar waveguide geometry has been considered before [59, 91] in a more general case, but without focusing on the role that SPPs might play in modifying the electromagnetic properties of the molecules.

The chapter is organized as follows: in the rest of this introductory section, we give the general formalism for calculating the Green's tensor in planar multilayered geometries. In Sec. 2.2 the case of a metal (Ag) slab in a dielectric (SiO_2) host is investigated by calculating the spontaneous emission and energy transfer rates and the SPP contribution to these rates. In Sec. 2.3 a planar waveguide geometry constructed by sandwiching a SiO_2 layer between two Ag plates is considered on the same lines of inquiry. Finally, Section 2.4 is reserved for conclusions.

2.1.1 The Green's tensor in a multilayered geometry

Consider a multilayered geometry, such as depicted in Fig. 2.1, consisting of a number of N layers of material, indexed by their layer number $i = 1, \ldots, N$. Each layer has a thickness d_i and dielectric permittivity ε_i. The layers are of infinite extent in the xy-plane and the z-axis is normal to the surface of each layer. To calculate the spontaneous emission and energy transfer rates in this geometry, the electromagnetic Green's tensor must be calculated first. Since the geometry is planar, one can use Cartesian coordinates to perform this calculation, starting from the expansion of the Green's tensor in terms of the VWFs of a Cartesian coordinate system, Eq. (1.64), and following the method of scattering superposition illustrated in the example from Subsection 1.4.1 of a single planar interface between two different media. Following

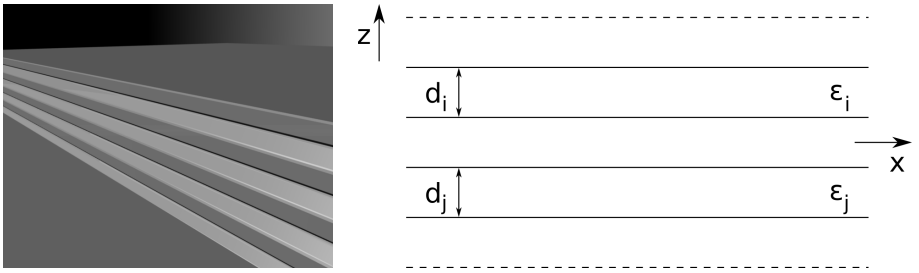

Figure 2.1: *Illustration of the multilayered geometry.*

the method outlined there, one may write the scattering term of the Green's tensor for the general case where the source (or donor) point is inside layer j and the field (or acceptor) point is inside layer i as

$$\mathscr{G}_s^{(ij)}(\mathbf{r},\mathbf{s},\omega) = \frac{i}{8\pi^2}\int \mathrm{d}^2k_\rho \frac{1}{k_{zj}k_\rho^2}\Big[R_M^{\pm(ij)\pm}\mathbf{M}(\mathbf{k}_\rho,\pm k_{zi},\mathbf{r})\otimes\mathbf{M}^*(\mathbf{k}_\rho,\pm k_{zj},\mathbf{s}) + \\ + R_N^{\pm(ij)\pm}\mathbf{N}(\mathbf{k}_\rho,\pm k_{zi},\mathbf{r})\otimes\mathbf{N}^*(\mathbf{k}_\rho,\pm k_{zj},\mathbf{s})\Big]. \tag{2.1}$$

A summation is implied over each pair of $\pm$ indices. These indices denote the direction of propagation of an electromagnetic mode at the position of the acceptor (first index) or the donor (second index). Imposing the continuity conditions across each interface and the radiation condition, as discussed in Subsection 1.4.1, one arrives at an inhomogeneous system of 2^{N-1} linear equations in 2^{N-1} unknowns, the R-coefficients. These coefficients are thus uniquely determined and solving this inhomogeneous system of linear equations leads to a solution for the scattering term of the Green's tensor and, hence, to a solution for the full electromagnetic Green's tensor. The spontaneous emission and energy transfer rates can then be calculated using the formulas of Sec. 1.3, Eqs. (1.34) and (1.54), respectively.

In the following section we shall use the theoretical framework thus built to study the SE and ET rates, as well as the effect of SPPs on these rates, for the case of a metallic slab embedded in dielectric host medium.

2.2 Metallic slab in a dielectric host medium

The first example of a multilayered planar geometry is that of a metallic slab of thickness d and dielectric permittivity $\varepsilon(\omega)$ embedded in an infinite dielectric background with dielectric permittivity ε_b. The metallic slab is characterized by the Drude model introduced in Subsection 1.4.2, expression (1.81), and is shown schematically in Fig. 2.2. The metal slab geometry being a particular example of a multilayered geometry, the method of scattering superposition presented in Sec. 2.1 can be used to calculate the Green's tensor in this geometry as well. We shall only consider the case when the donor molecule is positioned above the metal slab, in the dielectric host medium. In this case, the different expressions for the Green's tensor in Eq. (2.1) become

$$\mathscr{G}_s^{(11)}(\mathbf{r},\mathbf{s},\omega) = \frac{i}{8\pi^2}\int \mathrm{d}^2k_\rho \frac{1}{k_{z1}k_\rho^2}\Big[R_M^{+(11)-}\mathbf{M}(\mathbf{k}_\rho,k_{z1},\mathbf{r})\otimes\mathbf{M}^*(\mathbf{k}_\rho,-k_{z1},\mathbf{s}) + \\ + R_N^{+(11)-}\mathbf{N}(\mathbf{k}_\rho,k_{z1},\mathbf{r})\otimes\mathbf{N}^*(\mathbf{k}_\rho,-k_{z1},\mathbf{s})\Big] \tag{2.2a}$$

$$\mathscr{G}_s^{(21)}(\mathbf{r},\mathbf{s},\omega) = \frac{i}{8\pi^2}\int \mathrm{d}^2k_\rho \frac{1}{k_{z1}k_\rho^2}\Big[R_M^{\pm(21)-}\mathbf{M}(\mathbf{k}_\rho,\pm k_{z2},\mathbf{r})\otimes\mathbf{M}^*(\mathbf{k}_\rho,-k_{z1},\mathbf{s}) + \\ + R_N^{\pm(21)-}\mathbf{N}(\mathbf{k}_\rho,\pm k_{z2},\mathbf{r})\otimes\mathbf{N}^*(\mathbf{k}_\rho,-k_{z1},\mathbf{s})\Big] \tag{2.2b}$$

$$\mathscr{G}_s^{(31)}(\mathbf{r},\mathbf{s},\omega) = \frac{i}{8\pi^2}\int \mathrm{d}^2k_\rho \frac{1}{k_{z1}k_\rho^2}\Big[R_M^{-(31)-}\mathbf{M}(\mathbf{k}_\rho,-k_{z1},\mathbf{r})\otimes\mathbf{M}^*(\mathbf{k}_\rho,-k_{z1},\mathbf{s}) + \\ + R_N^{-(31)-}\mathbf{N}(\mathbf{k}_\rho,-k_{z1},\mathbf{r})\otimes\mathbf{N}^*(\mathbf{k}_\rho,-k_{z1},\mathbf{s})\Big] \tag{2.2c}$$

where, again, the index $\pm$ denotes a sum over $+$ and $-$ for that particular index position. As in the case of the single planar interface discussed in the example of Subsection 1.4.1, the expressions above can be further simplified by performing the angular k_θ integral analytically. An example of such a simplified expression can be given:

$$\mathscr{G}_{zz}^{(21)}(\mathbf{r},\mathbf{s},\omega) = \frac{i}{4\pi}\int_0^\infty \mathrm{d}k_\rho \frac{k_\rho}{k_{z1}k_1k_2} J_0(k_\rho|\rho-\rho_s|)R_N^{\pm(21)-}\mathrm{e}^{-i(\pm k_{z2}z - k_{z1}z_s)}, \tag{2.3}$$

where the above-mentioned summation convention applies.

The continuity conditions on the electric and magnetic field components across the two interfaces at $z = d/2$ and $z = -d/2$ lead to the following continuity conditions for the Green's tensor:

$$\hat{\mathbf{z}}\times\Big[\mathscr{G}^{(11)}(\mathbf{r},\mathbf{s},\omega) - \mathscr{G}^{(21)}(\mathbf{r},\mathbf{s},\omega)\Big]\Big|_{z=d/2} = 0 \tag{2.4a}$$

$$\hat{\mathbf{z}}\times\Big[\mathscr{G}^{(21)}(\mathbf{r},\mathbf{s},\omega) - \mathscr{G}^{(31)}(\mathbf{r},\mathbf{s},\omega)\Big]\Big|_{z=-d/2} = 0 \tag{2.4b}$$

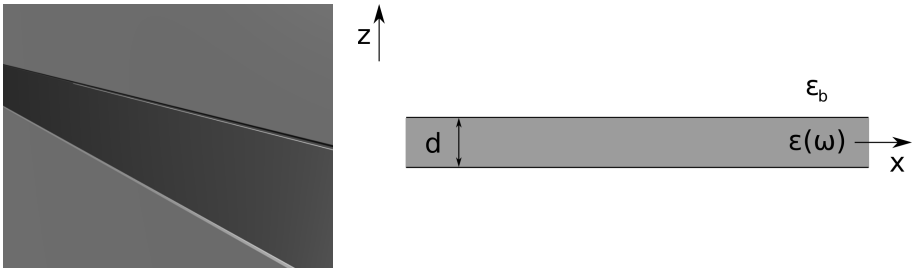

Figure 2.2: *Illustration of the metal slab in a dielectric host geometry.*

$$\hat{\mathbf{z}}\times\left[\nabla\times\mathscr{G}^{(11)}(\mathbf{r},\mathbf{s},\omega)-\nabla\times\mathscr{G}^{(21)}(\mathbf{r},\mathbf{s},\omega)\right]\Big|_{z=d/2}=0 \tag{2.4c}$$

$$\hat{\mathbf{z}}\times\left[\nabla\times\mathscr{G}^{(21)}(\mathbf{r},\mathbf{s},\omega)-\nabla\times\mathscr{G}^{(31)}(\mathbf{r},\mathbf{s},\omega)\right]\Big|_{z=-d/2}=0 \tag{2.4d}$$

As we mentioned in Subsection 2.1.1, these continuity conditions lead to an inhomogeneous system of linear equations in the unknown R-coefficients. In the present case of the metallic slab, one can consider that the geometry is formed by three layers: the slab itself, and the two semi-infinite dielectrics forming the background. In this case, then, $N=3$ and we must solve an inhomogeneous system of 4 ($=2^{3-1}$) linear equations in 4 unknowns. The characteristic matrices of the system, for the two polarizations, TE and TM, are given by:

$$\Delta_M=\begin{pmatrix} \mathrm{e}^{\frac{i}{2}k_{z1}d} & -\mathrm{e}^{\frac{i}{2}k_{z2}d} & -\mathrm{e}^{-\frac{i}{2}k_{z2}d} & 0 \\ k_{z1}\,\mathrm{e}^{\frac{i}{2}k_{z1}d} & -k_{z2}\,\mathrm{e}^{\frac{i}{2}k_{z2}d} & k_{z2}\,\mathrm{e}^{-\frac{i}{2}k_{z2}d} & 0 \\ 0 & \mathrm{e}^{-\frac{i}{2}k_{z2}d} & \mathrm{e}^{\frac{i}{2}k_{z2}d} & -\mathrm{e}^{\frac{i}{2}k_{z1}d} \\ 0 & k_{z2}\,\mathrm{e}^{-\frac{i}{2}k_{z2}d} & -k_{z2}\,\mathrm{e}^{\frac{i}{2}k_{z2}d} & k_{z1}\,\mathrm{e}^{\frac{i}{2}k_{z1}d} \end{pmatrix}, \tag{2.5a}$$

and

$$\Delta_N=\begin{pmatrix} \frac{k_{z1}}{k_1}\,\mathrm{e}^{\frac{i}{2}k_{z1}d} & -\frac{k_{z2}}{k_2}\,\mathrm{e}^{\frac{i}{2}k_{z2}d} & \frac{k_{z2}}{k_2}\,\mathrm{e}^{-\frac{i}{2}k_{z2}d} & 0 \\ k_1\,\mathrm{e}^{\frac{i}{2}k_{z1}d} & -k_2\,\mathrm{e}^{\frac{i}{2}k_{z2}d} & -k_2\,\mathrm{e}^{-\frac{i}{2}k_{z2}d} & 0 \\ 0 & \frac{k_{z2}}{k_2}\,\mathrm{e}^{-\frac{i}{2}k_{z2}d} & -\frac{k_{z2}}{k_2}\,\mathrm{e}^{\frac{i}{2}k_{z2}d} & \frac{k_{z1}}{k_1}\,\mathrm{e}^{\frac{i}{2}k_{z1}d} \\ 0 & k_2\,\mathrm{e}^{-\frac{i}{2}k_{z2}d} & k_2\,\mathrm{e}^{\frac{i}{2}k_{z2}d} & -k_1\,\mathrm{e}^{\frac{i}{2}k_{z1}d} \end{pmatrix}. \tag{2.5b}$$

while the unknown coefficient vectors are:

$$\mathbf{R}_M^{(i)\pm}=\begin{pmatrix} R_M^{+(1i)\pm} \\ R_M^{+(2i)\pm} \\ R_M^{-(2i)\pm} \\ R_M^{-(3i)\pm} \end{pmatrix}, \qquad \mathbf{R}_N^{(i)\pm}=\begin{pmatrix} R_N^{+(1i)\pm} \\ R_N^{+(2i)\pm} \\ R_N^{-(2i)\pm} \\ R_N^{-(3i)\pm} \end{pmatrix}, \tag{2.6}$$

and a couple of the free-terms vectors (we will not write them all down) are:

$$\mathbf{V}_M^{(1)-} = \begin{pmatrix} -\mathrm{e}^{-\frac{i}{2}k_{z1}d} \\ k_{z1}\,\mathrm{e}^{-\frac{i}{2}k_{z1}d} \\ 0 \\ 0 \end{pmatrix}, \qquad \mathbf{V}_N^{(2)+} = \begin{pmatrix} \frac{k_{z2}}{k_2}\,\mathrm{e}^{\frac{i}{2}k_{z2}d} \\ k_2\,\mathrm{e}^{\frac{i}{2}k_{z2}d} \\ 0 \\ 0 \end{pmatrix}. \tag{2.7}$$

The continuity conditions (2.4) can now be written in matrix form as

$$\Delta_{M(N)} \cdot \mathbf{R}_{M(N)}^{(i)\pm} = \mathbf{V}_{M(N)}^{(i)\pm}. \tag{2.8}$$

As previously (Subsection 1.4.1), index i denotes the layer where the donor molecule is embedded, and index $\pm$ denotes the direction of propagation at the donor's position.

Equation (2.8) above allows us to calculate the R-coefficients in the presence of a point dipolar source. If, on the other hand, one wishes to obtain the normal modes of the geometry under consideration, one must set the free-term vectors to zero and solve the resulting homogeneous system of linear equations. Such a system has a non-trivial solution only when the determinant of its characteristic matrix ($\Delta_{M(N)}$ in this case) is set to zero. As we are specifically interested only in surface plasmons, and do not intend to calculate the full mode structure of the geometry, we are only interested in the condition $\det(\Delta_N) = 0$. After some straightforward algebraic manipulations, this condition reduces to two independent equations:

$$\varepsilon(\omega)k_{z1} + \varepsilon_b k_{z2} \tanh(-ik_{z2}d/2) = 0 \tag{2.9a}$$

$$\varepsilon(\omega)k_{z1} + \varepsilon_b k_{z2} \coth(-ik_{z2}d/2) = 0 \tag{2.9b}$$

where ε_b and $\varepsilon(\omega)$ are the dielectric permittivities of the background and metal slab, respectively, as introduced at the beginning of this section. Solving these two equations numerically, one arrives at two dispersion curves of the general form $\omega = \omega(k_x)$, where k_x is the component of the wavevector parallel to the interface, which is conserved, and hence the same on either side of the two interfaces. The two curves differ in the symmetry with respect to the mirror plane at $z = 0$ that the electric field of the SPP exhibits. Eq. (2.9a) corresponds to the antisymmetric branch, while Eq. (2.9b) corresponds to the symmetric branch. Fig. 2.3a shows the dispersion curves of these two types of SPPs for two slab thicknesses, $d = 0.01\,\lambda_P$ and $d = 0.20\,\lambda_P$, where λ_P is the wavelength associated with the plasma frequency ω_P of the Drude metal. For Ag, the plasma frequency is $\omega_P^{\mathrm{Ag}} = 9.176$ eV, corresponding to a wavelength

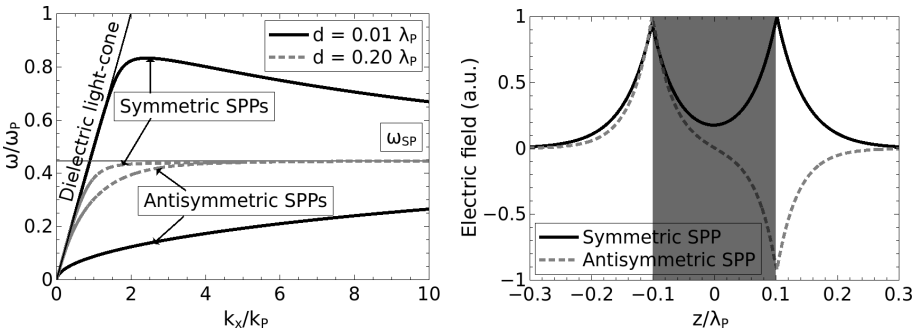

(a) *Dispersion diagram* **(b)** *Electric field*

Figure 2.3: *(a) Dispersion diagram of SPPs in a slab geometry with $d = 0.20\,\lambda_P$ and $d = 0.01\,\lambda_P$. (b) Electric field distribution of SPPs on a slab of thickness $d = 0.20\,\lambda_P$.*

of $\lambda_P^{\mathrm{Ag}} = 135.12$ nm [92]. The two corresponding slab thicknesses are, therefore $d = 0.01\,\lambda_P^{\mathrm{Ag}} = 1.35$ nm and $d = 0.20\,\lambda_P^{\mathrm{Ag}} = 27.02$ nm.

As is visible from Fig. 2.3a, the symmetric branch of the SPP exists partially in the stop-gap between ω_{SP} and ω_{P}, where no modes exist on a single interface between a metal and a dielectric (see Fig. 1.3). This happens, however, only when the thickness of the metallic slab is small enough so that the SPP dispersion relation splits into the two branches of Eqs. (2.9). When $-ik_{z2}\,d/2 \gtrsim 2.0$, or $d \gtrsim 4.0\,\delta_m$, where $\delta_m = 1/\mathrm{Im}(k_{z2})$ is the penetration depth of the SPPs inside the Drude metal slab, then $\tanh(-ik_{z2}d/2) \approx \coth(-ik_{z2}d/2) \approx 1$ and the two distinct SPP dispersion relations reduce to the dispersion relation for SPPs on a planar interface between a metal and a dielectric half-space, Eq. (1.83). For a Ag slab embedded in SiO_2, the SPP frequency is $\omega_{SP}^{\mathrm{Ag}} \approx 4.103$ eV, with a corresponding wavelength of $\lambda_{SP}^{\mathrm{Ag}} = 302.13$ nm. Close to this frequency, namely at $\omega = 0.40\,\omega_{\mathrm{P}}^{\mathrm{Ag}} = 3.67$ eV, the penetration depth of SPPs inside silver is $\delta^{\mathrm{Ag}} = 1/\mathrm{Im}(k_z^{\mathrm{Ag}}) \approx 80$ nm. When the slab thickness is larger than this penetration depth, the SPPs on the two interfaces of the slab decouple, and each SPP is localized at a single interface.

In the next subsection we calculate the SE rate of a molecule placed above a Drude slab and investigate the effect of SPPs on the rate.

2.2.1 Spontaneous Emission

We first consider a molecule with a molecular transition dipole along the z axis and placed above a Drude metal slab of thickness d, embedded in a dielectric medium with constant dielectric permittivity, $\varepsilon_d = 4$. Fig. 2.4 presents the various decay rates

of the molecule for several slab thicknesses as a function of both distance to the slab and frequency. Panels 2.4a and 2.4b show, in a logarithmic scale, a contour plot of the total emission rate of the molecule as a function of both frequency ω and distance z to the slab, for two slab thicknesses, $d = 0.01\,\lambda_P$ and $d = 0.20\,\lambda_P$. Panels 2.4c and 2.4d show the distance dependence of the different contributions to the emission rate at a frequency close to the surface plasmon frequency, $\omega = 0.40\,\omega_{\rm P}$, or $\omega_{\rm Ag} = 3.67$ eV ($\lambda_{\rm Ag} = 337.8$ nm) in a Ag/SiO_2 environment, and for the same two slab thicknesses. The contributions of the two types of SPPs, symmetric and antisymmetric are clearly shown, as is the radiative emission rate, i.e. the emission into photons freely propagating in the dielectric medium. A further contribution to the decay rate of the molecule, via the *lossy surface waves* (LSW), is also present at very small distances from the surface of the slab. This contribution, which, unlike SPPs, is completely absent in the case of a lossless Drude metal, comes about because of the presence of losses in the metal and it is related to excitation of electron-hole pairs [93]. Finally, panels 2.4e and 2.4f show the frequency-dependence of the total emission rate of a molecule at different distances from a slab of the same two thicknesses as in the previous four panels. The frequency range spans the interval $\omega \in (0, \omega_{\rm P})$, encompassing both what in Figs. 2.4a and 2.4b we have called the *surface plasmon region*, where SPPs can be excited, and the *stop-gap*, where no SPPs exist on a single interface.

In panels 2.4a and 2.4b it is evident that the largest enhancement of the emission rate occurs when the molecule is very close to the interface and its frequency ω is very close to the surface plasmon frequency, ω_{SP}, although, for the case of the thinner slab in 2.4a, the enhancement is still appreciable even at relatively larger distances from the slab and at frequencies far from ω_{SP}. We shall discuss this effect further when we analyze panels 2.4e and 2.4f.

Panels 2.4c and 2.4d break down the emission rate at $\omega = 0.40\,\omega_{\rm P}$ into individual contributions coming from the radiative emission rate, as well as from SPPs. As one would expect by considering the dispersion curves for SPPs from Fig. 2.3a, as the slab thickness increases, the contributions from the two types of SPPs become more and more similar to one another and to the contribution of a SPP on a single interface between a dielectric and a metal. For smaller slab thicknesses, (Fig. 2.4c), there is a marked difference between the two contributions. At the frequency that we use, $\omega = 0.40\,\omega_{\rm P}$, the antisymmetric SPP has a very large parallel component of the wavevector and hence, a very small penetration depth inside both the dielectric and the Drude slab. Its contribution to the decay rate is, therefore, significant only when the molecule is very close to the slab (below 5 nm for the Ag/SiO_2 geometry). The dispersion curve of the symmetric SPP, on the other hand, lies very close to the light line in the dielectric (Fig. 2.3a) and the symmetric SPP is, therefore, weakly confined to the interface, contributing significantly to the decay rate even when the molecule is several wavelengths distant from the slab. In all cases, the total decay rate of the molecule at

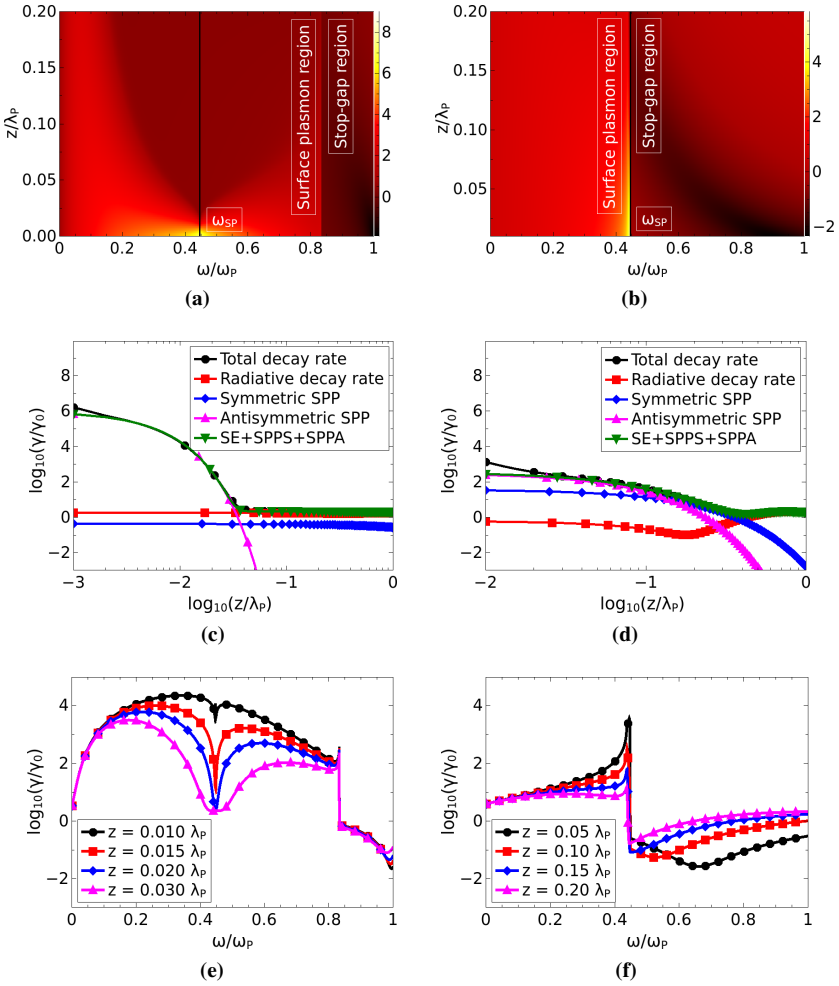

Figure 2.4: *Relative decay rates of a molecule above a Drude slab with* $\gamma = 2.288 \times 10^{-3}\,\omega_P$*. The thickness of the slab is* $d = 0.01\,\lambda_P$ *for the three panels on the left column and* $d = 0.20\,\lambda_P$ *for the three panels on the right column. This corresponds, in a Ag/SiO*$_2$ *environment, to* $d = 1.36$ *nm and* $d = 27.02$ *nm, respectively. (a) and (b) show the decay rates as a function of both frequency and distance to the upper surface of the slab; (c) and (d) show the different contributions to the relative decay rate as a function of distance to the slab at a frequency* $\omega = 0.40\,\omega_P$*; (e) and (f) show the frequency dependence of the relative decay rate for several molecule-slab separations.*

sufficiently large distances from the slab reverts to its value in a homogeneous medium of dielectric permittivity $\varepsilon_d = 4$. The difference between the curves representing the total decay rate, and the sum of the contributions from the radiative decay rate and the SPP decay rates comes from the contribution of Lossy Surface Waves, and, as we mentioned previously, is absent for a lossless Drude metal. The LSW contribution is significant only when the molecule is very close to the surface of the slab, and is more marked for the thicker slab (Fig. 2.4d).

The last two panels in Fig. 2.4, panels 2.4e and 2.4f, depict the frequency dependence of the total emission rate of a molecule at several distances above a slab of thickness $d = 0.01\,\lambda_P$ (2.4e) and $d = 0.20\,\lambda_P$ (2.4f). For the smaller of the two thicknesses (2.4e), the frequency range where SPPs can be excited is larger, as seen from the dispersion curves in Fig. 2.3a. Correspondingly, there is an increase in the emission rate of the molecule in this frequency range. Two peaks in the emission rate are clearly present. At small molecule-slab separations, the near-field of the molecule can successfully excite SPPs of very large wavevectors, whose frequency is very close to the surface plasmon frequency ω_{SP}. As the molecule-slab separation is increased, the near-field of the molecule, due to its evanescent nature, can only couple to wavevectors with smaller in-plane components, and thus can excite SPPs with a smaller wavevector, whose frequency is further away from ω_{SP}. The peak of the emission rate is then shifted away from the surface plasmon frequency, towards lower frequencies (antisymmetric SPP) and higher frequencies (symmetric SPP), respectively. As the frequency is increased and exits the region where SPPs can be excited, the emission rate drops abruptly and is essentially equal to the radiative emission rate.

For the larger of the two slab thicknesses, $d = 0.20\,\lambda_P$, no SPPs can be excited above the surface plasmon frequency ω_{SP} (see also Fig. 2.3a) and the surface plasmon frequency region is delimited by ω_{SP}, as illustrated in panel 2.4b as well. As the molecule-slab separation is increased, the shift of the peak in the emission rate occurs only towards lower frequencies, and above ω_{SP}, the emission rate is once again equal to the radiative emission rate.

2.2.2 Energy Transfer

We turn now to calculating the ET rate between two molecules placed near a Drude metal slab. Fig. 2.5 shows the two configurations of molecules that we use in calculating the ET rate. The fact that SPPs can be excited at the two surfaces of the slab has interesting consequences. For the first configuration, Fig. 2.5a, one can calculate the ET through the slab, and investigate how excitation of SPPs influences this transfer. As was mentioned before, for small slab thicknesses both symmetric and antisymmetric SPPs can be excited; their electromagnetic field extends between the two surfaces of the slab, thus being able to facilitate the energy transfer between molecules placed

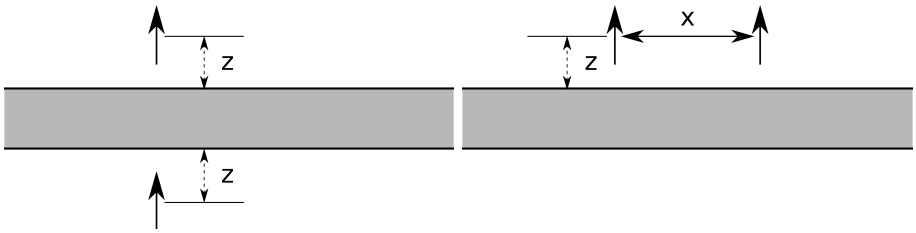

(a) *Molecules on opposite sides of the slab* **(b)** *Molecules on the same side of the slab*

Figure 2.5: *Two configurations of molecules used in calculating the ET rate in the presence of the Drude metallic slab.*

on opposite sides of the slab.

Fig. 2.6 shows the ET rate for slabs of different thicknesses, when the two molecules are in the two configurations of Fig. 2.5. Fig. 2.6a shows the ET rate through the slab for the configuration in Fig. 2.5a. The molecules are placed on the same z-axis, and their dipole moments are oriented along z as well. For all the curves in this figure, the relative ET rate drops off monoexponentially for small values of z, with a decay distance roughly equal to the characteristic decay distance of the antisymmetric SPP. This suggests that the transfer of energy occurs predominantly through the antisymmetric SPP. For thicknesses even larger than those shown in Fig. 2.6a, the ET rate through the slab is negligible, since the two extended SPPs now become localized at each interface, failing to reach across the slab.

Fig. 2.6b shows the ET rate along the slab, for the configuration in Fig. 2.5b. The molecules are placed on the same side of the slab, at a distance of $z = 0.01\,\lambda_P = 1.35$ nm from its surface, and with their dipole moments oriented along the z-axis. The ET rate is plotted as a function of the x-distance between the molecules in the plane of the slab. If the molecules are placed on the same side of the slab, one can investigate how excitation of the two different types of SPPs influences the transfer of energy along the metal slab. Depending on the thickness of the slab, d, the symmetric and antisymmetric SPPs can have very different propagation lengths along the surface of the slab, just as their penetration depth inside the slab can be markedly different, especially near the surface plasmon frequency, ω_{SP} (see also the discussion in subsection 2.2.1).

If we consider the x-dependence of the SPPs, in addition to the dampening due to ohmic losses in the metal slab, there also exists a (much larger for the linewidth γ considered here) dampening due to the circular symmetry of the geometry. The SPPs are excited by a point dipole and, therefore, they propagate along the interface from one single point, leading to this dampening. The symmetric SPP, whose wavevector is the smaller of the two, has a long characteristic wavelength, while the characteristic wave-

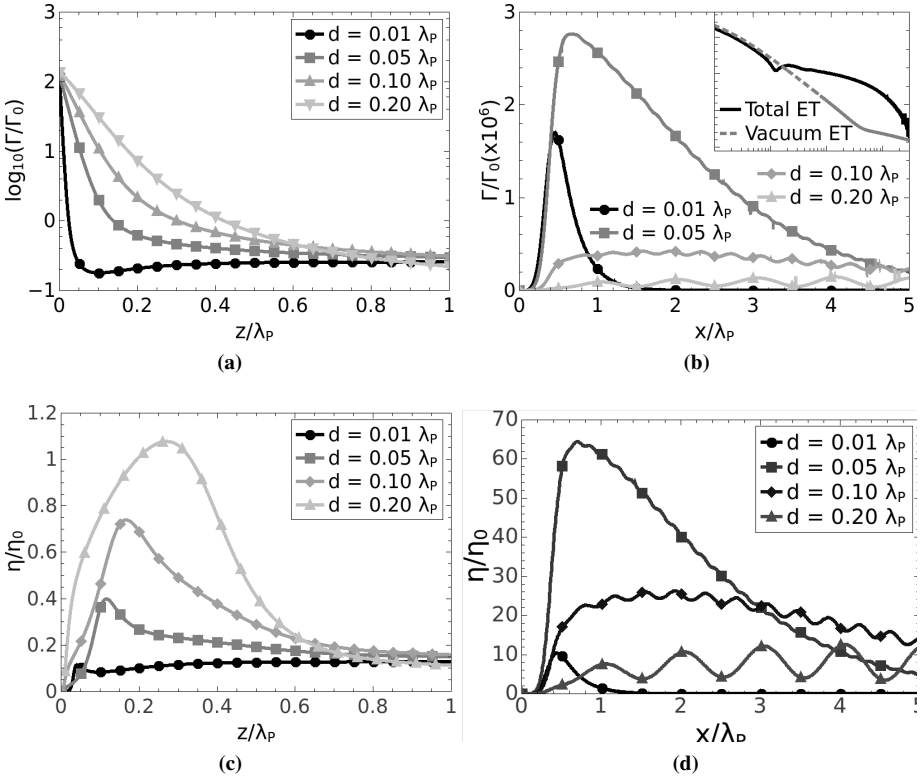

Figure 2.6: *Relative ET rate between two molecules in the configurations of Fig. 2.5; (a) configuration from Fig. 2.5a, with the ET rate plotted as a function of the distance z between a molecule and its corresponding surface of the slab; (b) configuration from Fig. 2.5b, with the ET rate plotted as a function of the distance x between the molecules, when the molecules are at a distance $z = 0.01\,\lambda_P$ from the upper surface of the slab. ; (c) $\tilde{\eta}$ ratio for the configuration from Fig.2.5a; (d) $\tilde{\eta}$ ratio for the configuration from Fig. 2.5b. The frequency is $\omega = 0.40\,\omega_P$, the linewidth is $\gamma = 2.288 \times 10^3\,\omega_P$.*

length of the antisymmetric SPP is shorter. This mismatch in wavelength between the SPPs, coupled to the fact that the ET rate from Eq. (1.54) depends on the square of the Green's tensor, and therefore includes interference terms between different contributions to this tensor, accounts for the oscillations visible in the curves in Fig. 2.6b. For the thicker slabs ($d = 0.10\,\lambda_P$ and $d = 0.20\,\lambda_P$), the characteristic wavelengths of the two SPPs at $\omega = 0.40\,\omega_P$ are comparable in magnitude, while still differing. The amplitude of the two contributions is also comparable, which leads to pronounced interference effects between them and a clearly discernible oscillatory behavior of the

relative ET rate. For the thinner slabs ($d = 0.01\,\lambda_P$ and $d = 0.05\,\lambda_P$), the dispersion curves of the two SPPs differ dramatically from each other. The characteristic wavelengths of the SPPs at $\omega = 0.40\,\omega_P$ are, hence, also markedly different, as are their individual contributions to the ET rate. The interference effects are still present, but much weaker, and the main contribution to the ET rate comes, in this case, from the short-wavelength antisymmetric SPP, as the less pronounced oscillations modulating the ET rate curves in Fig. 2.6b illustrate.

In addition to considering the SE and ET rates relative to their values in free space, another useful comparison is between the SE and ET rates themselves, in the same geometry. The reason is that the energy transfer rate can only be measured if it is comparable to or larger than the decay rate of the donor due to other channels. Assuming that the decay of the donor due to vibrational interactions is small (so that the donor's quantum yield in vacuum is large), we compare the ET rate to the SE rate, which includes decay due to all electromagnetic interactions (i.e., also due to SPPs). Thus, we define $\eta \equiv \Gamma/\gamma$; if $\eta > 1$, ET is the dominant channel for the donor to lose its energy. In Figs. 2.6c and 2.6d, we plot the ratio,

$$\tilde{\eta} \equiv \frac{\eta}{\eta_0} = \frac{\Gamma/\gamma}{\Gamma_0/\gamma_0} = \tilde{\Gamma}/\tilde{\gamma}, \tag{2.10}$$

corresponding to the situation of Figs. 2.6a and 2.6b, respectively. Thus, these plots show the role of the geometry (and implicitly SPPs) in favoring one decay channel of the donor (excitation transfer to the acceptor) over another (spontaneous decay), when compared to free space. From Fig. 2.6c we observe that for the molecular configuration of Fig. 2.5a for almost all slab thicknesses, the ratio $\tilde{\eta}$ is smaller than unity, expressing the fact that the enhancement of the ET rate in the presence of the metal slab is smaller than the enhancement of the SE rate in the presence of the metal slab. Consequently, it may be difficult to experimentally observe the energy transfer in this particular geometry.

The situation is quite different for the molecular configuration from Fig. 2.5b. For this case, we observe that the ratio $\tilde{\eta}$ can be much greater than unity, which means that the effect of the metal slab may strongly favor energy transfer from the donor to the acceptor over the spontaneous decay of the donor. We note that, since in the geometry of Fig. 2.5b the SE rate does not depend on x, the curves in Fig. 2.6d are just scaled versions of those in Fig. 2.6b (now plotted in a linear scale); the same does not hold for Figs. 2.6c and 2.6a, in which corresponding curves really are functionally different from each other, because the SE rate depends on z.

The results presented in Fig. 2.6 have been obtained when both the donor and acceptor are oriented along the z-direction, perpendicular to the metal slab. It is straightforward to generalize them for different orientations of the molecules as well as for rotational averages.

2.3 Planar Waveguide

This section is dedicated to investigating the role of SPPs in the electromagnetic interactions of molecules (i.e. spontaneous emission and energy transfer) placed inside a planar waveguide. The planar waveguide is shown in Fig. 2.7 and it consists of a dielectric slab with permittivity $\varepsilon_2 = 4$ and thickness d_2 sandwiched between two Drude metal slabs of thickness d_1. Analogous to the case of the single Drude slab,

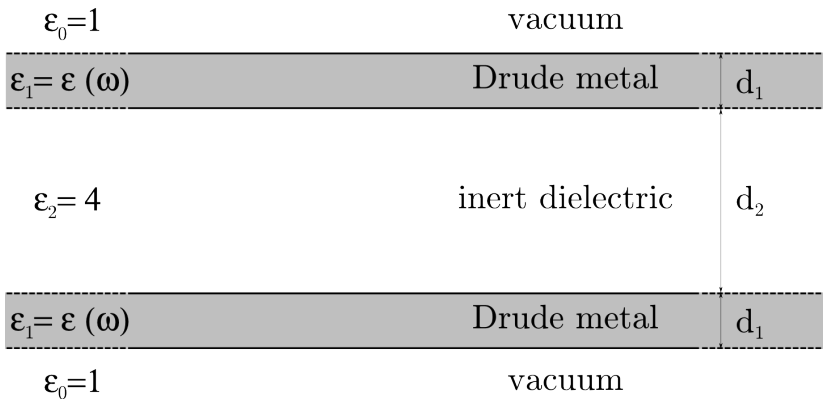

Figure 2.7: *Geometry of the waveguide.*

the symmetry plane at $z = 0$ for this geometry splits the dispersion relation of the SPP of this geometry into four distinct branches: two groups of symmetric and antisymmetric SPPs, associated with the two types of interfaces comprising the geometry: an external interface between the Drude slab and the vacuum outside the waveguide, and an internal interface, between the Drude slab and the material comprising the interior of the waveguide [94, 95]. These dispersion diagrams are shown in Fig. 2.8 for several parameters of the waveguide. The four different branches of the dispersion relation are: *External Antisymmetric SPP* (EASPP), *External Symmetric SPP* (ESSPP), *Internal Antisymmetric SPP* (IASPP) and *Internal Symmetric SPP* (ISSPP).

2.3.1 Spontaneous Emission

In this subsection we present calculations of the emission rates of molecules placed in the vicinity of and inside a waveguide, emphasizing the contribution of SPPs to these rates. Fig. 2.9 shows the total SE rate of a molecule placed above the waveguide of Fig. 2.8, as well as the radiative emission rate and the emission rate into the different types of SPPs mentioned in the beginning of this section. The log-log scale employed here makes these different contributions to the SE rate plainly visible. The

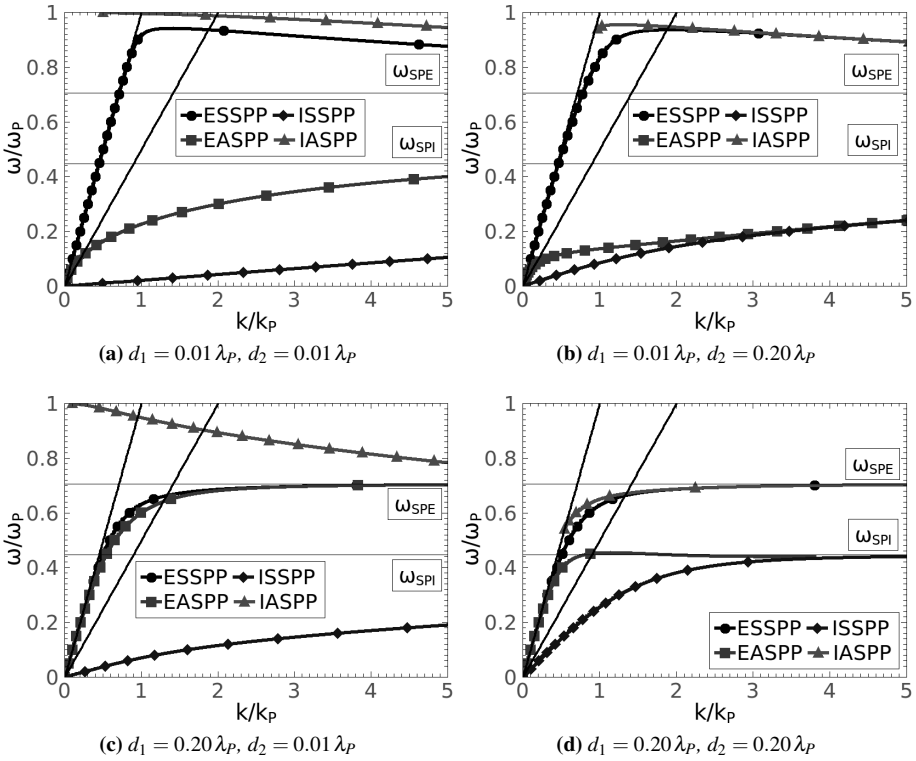

(a) $d_1 = 0.01\,\lambda_P$, $d_2 = 0.01\,\lambda_P$ **(b)** $d_1 = 0.01\,\lambda_P$, $d_2 = 0.20\,\lambda_P$

(c) $d_1 = 0.20\,\lambda_P$, $d_2 = 0.01\,\lambda_P$ **(d)** $d_1 = 0.20\,\lambda_P$, $d_2 = 0.20\,\lambda_P$

Figure 2.8: *Dispersion relations for SPPs in a planar waveguide geometry with* $\gamma = 0$.

frequency used for these calculations is $\omega = 0.40\,\omega_{\mathrm{P}}$, close to the *internal surface plasmon frequency*, $\omega_{\mathrm{SPI}} = 1/\sqrt{5}\,\omega_{\mathrm{P}} \approx 0.447\,\omega_{\mathrm{P}}$.

Panel 2.9a corresponds to thicknesses $d_1 = d_2 = 0.01\,\lambda_P$, for which the difference in the contributions of the different types of SPPs is maximum (see Fig. 2.8). The ESSPP, lying closest to the light-line in vacuum, has the smallest contribution to the decay rate. The main contribution to the decay rate of the molecule comes from the EASPP, which, though more confined to the external surface of the waveguide than the ESSPP, couples much stronger to the molecule. Finally, the ISSPP, with its larger parallel component of the wavevector, is the strongest confined to an interface, and its contribution is relevant only very close to the surface of the waveguide.

If we now increase the thickness of the material inside the waveguide, making $d_2 = 0.20\,\lambda_P$, (see Fig. 2.9b), the EASPP and ISSPP become virtually indistinguishable,

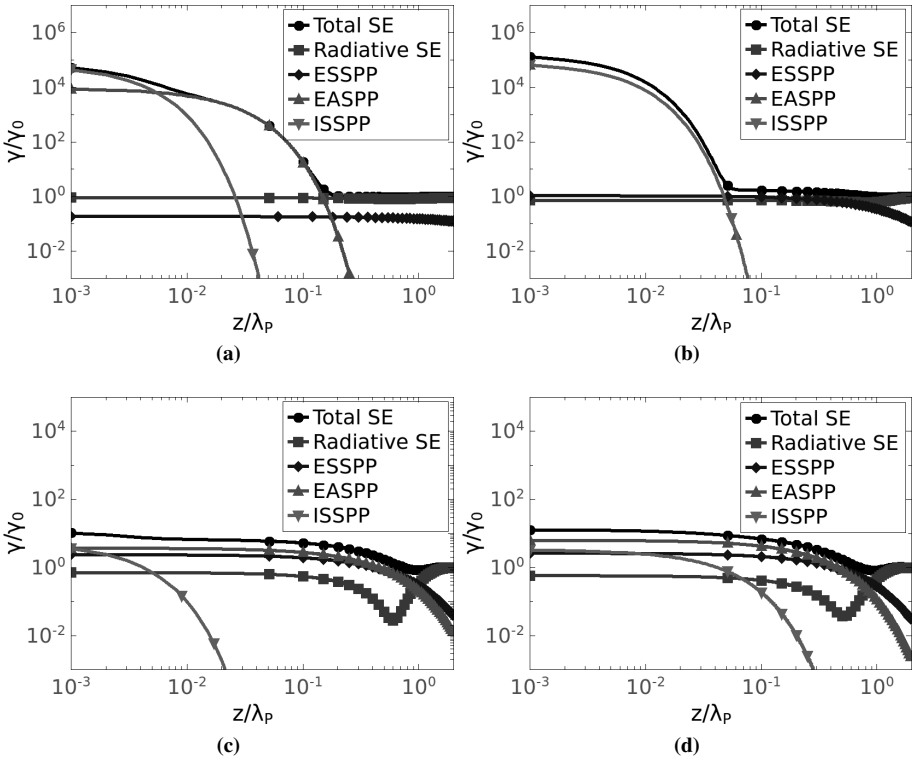

Figure 2.9: *Relative decay rates of molecules above a planar waveguide, as a function of the distance to the surface of the waveguide, for $\gamma = 0$. (a) $d_1 = 0.01\,\lambda_P$, $d_2 = 0.01\,\lambda_P$; (b) $d_1 = 0.01\,\lambda_T$, $d_2 = 0.20\,\lambda_T$, (c) $d_1 = 0.20\,\lambda_P$, $d_2 = 0.01\,\lambda_P$, (d) $d_1 = 0.20\,\lambda_P$, $d_2 = 0.20\,\lambda_P$. The frequency is $\omega = 0.40\,\omega_P$, where no IASPP can be excited (see Fig. 2.8).*

(see Fig. 2.8b), and their contributions to the decay rate are the same and constitute the dominant channels through which the molecule decays.

If, on the other hand, the thickness of the metal slabs is increased to $d_1 = 0.20\,\lambda_P$, while keeping the dielectric material inside the waveguide to a thickness of $d_2 = 0.01\,\lambda_P$ (see Fig. 2.9c), it is the ESSPP and EASPP that start to coincide (see Fig. 2.8c) and, hence, it is their contribution that is dominant and roughly the same, while the ISSPP contribution, though comparable to the others at very short distances from the waveguide, falls off abruptly as this distance increases.

Finally, when both thicknesses involved in the problem are set to $d_1 = d_2 = 0.20\,\lambda_P$, all types of SPPs have a relatively small parallel component of the wavevector (see

Fig. 2.8d), and hence, larger penetration depths in the materials (see Fig. 2.9d). It is worth pointing out that in the last two panels in Fig. 2.9, where $d_1 = 0.20\,\lambda_P$, the enhancement of the decay rate is much smaller than in the first two panels, where $d_1 = 0.01\,\lambda_P$.

For all the panels in Fig. 2.9, the frequency used, $\omega = 0.40\,\omega_{\rm P}$, forbids excitation of the IASPP, whose dispersion branch, Fig. 2.8 shows, lies completely above the internal SPP frequency, $\omega_{\rm SPI}$.

We next consider a molecule placed inside the dielectric material of the waveguide, and investigate how the SPPs contribute to the SE rate of such a molecule. Fig. 2.10 shows the SE rates of a molecule placed inside the waveguide as a function of its position along the z-axis. Comparing the results from Fig. 2.10 to those from Fig. 2.9, there

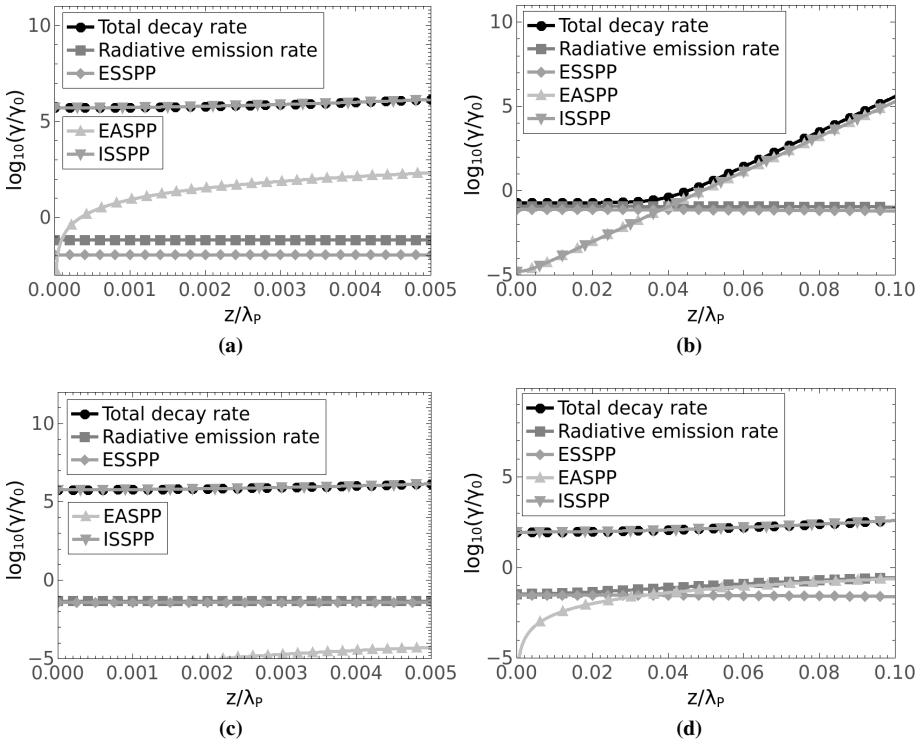

Figure 2.10: *Relative decay rates of molecules inside a planar waveguide, as a function of the distance to the center of the waveguide, for $\gamma = 0$; (a) $d_1 = 0.01\,\lambda_P$, $d_2 = 0.01\,\lambda_P$; (b) $d_1 = 0.01\,\lambda_P$, $d_2 = 0.20\,\lambda_P$, (c) $d_1 = 0.20\,\lambda_P$, $d_2 = 0.01\,\lambda_P$, (d) $d_1 = 0.20\,\lambda_P$, $d_2 = 0.20\,\lambda_P$. The frequency is $\omega = 0.40\,\omega_P$.*

are a number of differences present. The relevant comparison between the two figures is panel-by-panel, since there is a one-to-one correspondence between the panels of Fig. 2.10 and those of Fig. 2.9, as far as the parameters of the geometry are concerned. Whereas in Fig. 2.9a it is the ESSPP that has the largest contribution, in Fig. 2.10a the IASPP contributes the most to the SE rate. These two contributions are indistinguishable from one another in both Fig. 2.9b and Fig. 2.10b. In the remaining two panels, Fig. 2.10c and 2.10d, the IASPP is again strongly dominant, while the external SPPs (EASPP and ESSPP) have negligible and comparable contributions. One could envision tailoring the emission properties of a molecule placed inside the waveguide by, for example, placing it in a symmetric situation, such that coupling to the antisymmetric SPPs, internal and external, is forbidden and only coupling to the ESSPP is allowed, thus facilitating extraction of the emitted radiation to the outside of the waveguide.

2.3.2 Energy Transfer

This subsection is dedicated to investigating the ET rate between two molecules when placed inside and around the planar waveguide. Fig. 2.11 shows the relative ET rate between the two molecules (donor and acceptor) as a function of their separation along the waveguide, for several z-positions of the donor and acceptor, and two frequencies close to the two surface plasmon frequencies associated with the structure, $\omega_{\mathrm{SPI}} = 1/\sqrt{5}\,\omega_{\mathrm{P}} \approx 0.447\,\omega_{\mathrm{P}}$ and $\omega_{\mathrm{SPE}} = 1/\sqrt{2}\,\omega_{\mathrm{P}} \approx 0.707\,\omega_{\mathrm{P}}$. One can thus investigate the transfer of excitation energy within the waveguide, as well as to the outside medium. The calculations are performed when both molecules have their transition dipole moments perpendicular to the plane of the waveguide, or along the z-axis, and the two frequencies considered are $\omega = 0.40\,\omega_{\mathrm{P}}$ and $\omega = 0.70\,\omega_{\mathrm{P}}$. In a Ag/$SiO_2$/Ag waveguide these correspond to wavelengths of $\lambda = 337.8$ nm, and $\lambda = 193$ nm, respectively. The calculations in Fig. 2.11 have been performed for several thicknesses of the metallic plates and heights of the dielectric interior of the waveguide. In panel 2.11a, the relevant parameters are $d_1 = d_2 = 0.01\,\lambda_P$. A large enhancement of the ET rate occurs from the inner to the outer surface of metal plate, caused by excitation of the ISSPP by the near-field of the donor located at $(x_s = 0, z_s = 0.004\,\lambda_P)$. The acceptor molecule couples to this SPP with its near- field, resulting in a large enhancement of the ET rate. The fact that the maximum of the relative ET rate occurs when the intermolecular separation along the waveguide, x, is approximately $x \approx 0.5\,\lambda_P$ can be accounted for by the fact that what is plotted in Fig. 2.11 is the *relative* ET rate, i.e. the ET rate in the planar waveguide normalized to its value in free-space. When the intermolecular separation is very small, the ET rate is in its Förster regime and, inside the waveguide, is dominated by the direct interaction between the molecules, i.e. the energy transfer occurs mainly through exchange of virtual photons which do

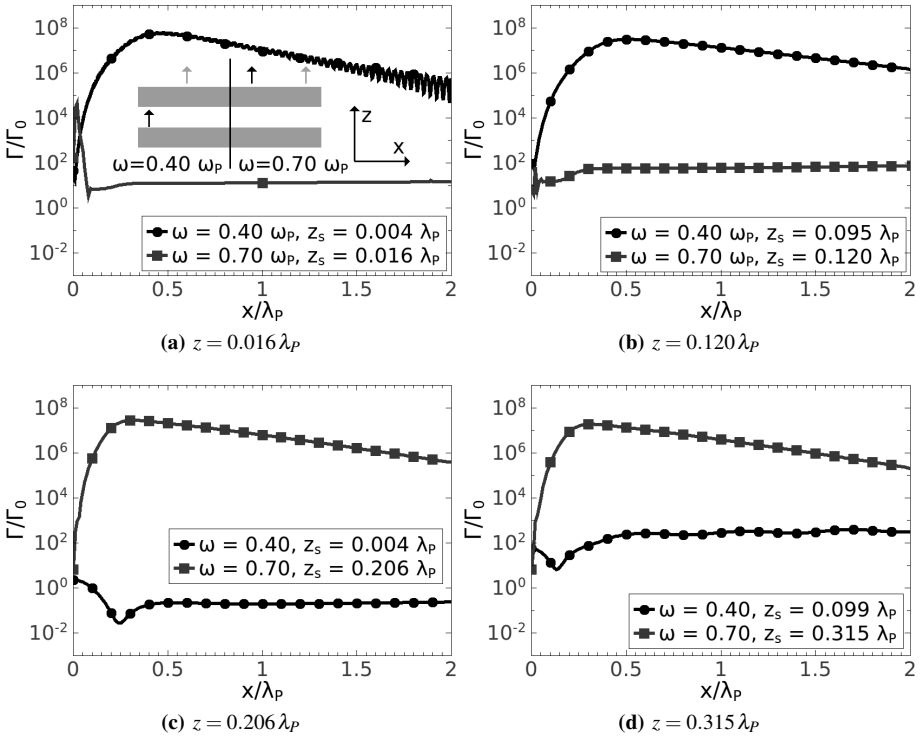

(a) $z = 0.016\,\lambda_P$ **(b)** $z = 0.120\,\lambda_P$

(c) $z = 0.206\,\lambda_P$ **(d)** $z = 0.315\,\lambda_P$

Figure 2.11: *(Color online) Relative ET rates between molecules in a planar waveguide geometry, as a function of their mutual separation along the x-axis, for* $\gamma = 2.288 \cdot 10^{-3}$. *In the inset, which is the same for all four subfigures, the black arrow represents the donor molecule, fixed at* z_s *and* $x_s = 0$*, the gray arrow represents the acceptor molecule, fixed at z and with varying x-position; (a)* $d_1 = 0.01\,\lambda_P$, $d_2 = 0.01\,\lambda_P$*; (b)* $d_1 = 0.01\,\lambda_P$, $d_2 = 0.20\,\lambda_P$*, (c)* $d_1 = 0.20\,\lambda_P$, $d_2 = 0.01\,\lambda_P$*, (d)* $d_1 = 0.20\,\lambda_P$, $d_2 = 0.20\,\lambda_P$.

not scatter of the waveguide surfaces. As the intermolecular distance increases, the direct interaction contributes less, and the main contribution comes from the ISSPP. The rapid oscillations in the ET rate can be attributed, as in the case of a single metal plate, to interference between the different pathways of ET. In this case, it is the interference between the ISSPP and the EASPP which leads to these oscillations. At the frequency which is used, $\omega = 0.40\,\omega_P$, the dispersion curves of these two SPPs show the largest wavevector (see Fig. 2.8a), with the ISSPP wavevector the largest of the two. By contrast, when both molecules are placed outside the waveguide, and the frequency is close to the external plasmon frequency, i.e. $\omega = 0.70\,\omega_P$, there is almost no enhancement of the ET rate. At this particular frequency the EASPP dispersion curve

is very close to the light-line and no other SPPs are excited (see Fig. 2.8a again).

As the height of the dielectric interior of the waveguide is increased, the transfer rate from the inner to the outer surface of the metal plate is seen not to depend strongly on the height of the waveguide interior (see panel 2.11b, the curve for $\omega = 0.40\,\omega_{\rm P}$). It is noticeable, however, that the oscillations in the ET rate are no longer present. The reason for this is that for this particular height of the waveguide interior, $d = 0.20\,\lambda_P$, the ISSPP and EASPP dispersion curves nearly overlap (see Fig. 2.8b). As such, the interference between these two pathways of energy transfer is always constructive, which leads to the absence of oscillations in the ET rate. Near the external plasmon frequency, at $\omega = 0.70\,\omega_{\rm P}$, the enhancement of the ET rate is much smaller, for the same reason as discussed in the above paragraph.

If, on the other hand, it is the thickness of the metal plate that is increased, as in Fig. 2.11c, transfer from the interior to the exterior of the metal plate is actually suppressed near the internal plasmon frequency, $\omega = 0.40\,\omega_{\rm P}$. In this case, even though the ISSPP still has a large wavevector, the acceptor molecule located on the outside of the waveguide can no longer couple to it efficiently. The EASPP, on the other hand, although capable of coupling to the donor molecule, has a wavevector very close to the light-line and, hence, a very small contribution. Near the external plasmon frequency, at $\omega = 0.70\,\omega_{\rm P}$, however, the wavevector corresponding to both the EASPP and the ESSPP are much larger – they nearly coincide – and the ET transfer between two molecules close to the outer surface of the metal plates is considerably enhanced.

When both the thickness of the metal plates and the height of the waveguide interior are rather large (see Fig. 2.11d), there is a slight enhancement of the ET rate to the outside of the waveguide. On top of this enhancement there is a slight oscillation of the ET rate, due to interference between the IASPP and the ESSPP (see Fig. 2.8d) which, at $\omega = 0.40\,\lambda_P$, have wavevectors of the same order of magnitude. As in the previous case, the largest enhancement of the ET rate occurs when both molecules are close to the outer surface of the metal plate, mediated by the ESSPP at $\omega = 0.70\,\omega_{\rm P}$.

Finally, we have also calculated the $\tilde{\eta}$-ratio from Eq. (2.10) for Fig. 2.11 and have observed effects similar to those discussed for Fig. 2.6. Since the position of the donor is kept fixed, the curves obtained have the same shape as those of Fig. 2.11, only scaled by the relative SE rate of the donor, and for this reason we do not present them here.

2.4 Summary and conclusions

In this Chapter we have investigated the role that SPPs play in modifying the electromagnetic properties of atoms and molecules placed near a metallic slab embedded in a dielectric host, and in a planar waveguide. In these and other multilayered geometries, the presence of multiple interfaces gives rise to several branches in the dispersion relations of SPPs. These branches can be distinguished by their symmetries and their

influence on the spontaneous emission rate and the energy transfer rate has been investigated.

In a slab geometry, the dispersion relation of surface plasmons splits into two branches: symmetric and antisymmetric, which differ markedly from one another when the thickness of the slab is suitably small. Their influence on the SE and ET rates can, consequently, also differ appreciably, and we have been able to investigate this influence and relate it to specific properties of the SPPs, i.e. wavelength and frequency. It is close to the surface plasmon frequency of the slab geometry, ω_{SP}, that the effect of the SPPs on the SE and ET rates is the strongest. At these frequencies, the wavelength of the SPPs (the antisymmetric SPP, to be precise) can be much smaller than that of light of the same frequency, which leads to subwavelength effects in the behavior of the SE and ET rates, such as very fast oscillations in the ET rate, for example.

If we consider the geometry of the planar waveguide, the SPP dispersion relation now splits into four branches: external symmetric and antisymmetric and internal symmetric and antisymmetric, with two surface plasmon frequencies, associated with the external, ω_{SPE}, and internal, ω_{SPI}, SPPs. Depending on the positioning of molecules inside or around the planar waveguide, and on the molecule's characteristic frequency, they can be made to selectively couple to one or more of these SPPs and their spontaneous emission or energy transfer rates can be dramatically modified. We have been able to identify the SPP branches that affect these rates the most for several particular parameters of the geometry and configurations of molecules.

This intricate dependence of the electromagnetic properties of molecules on geometrical parameters and frequency extends the space of possibilities for tailoring these properties.

CHAPTER 3

Intermolecular interactions and energy transfer near a circular cylinder

Abstract

In this chapter we investigate the rate of resonance electronic energy transfer between two molecules near a metallic cylinder. Both the case of a real and frequency independent dielectric permittivity ε and the case of a Drude model for a metal cylinder are considered. If the donor is placed at a fixed position near the cylinder, we find that the energy transfer rate to the acceptor is enhanced compared to its vacuum value in a number of discrete hot-spots, centered at the cylinder's surface. In the absence of dispersion and absorption the rate of energy transfer may be enhanced at most a few times. On the other hand, for the Drude model the enhancement may be huge (up to six orders of magnitude) and the hot-spots are sharply localized at the surface. We show that these observations can be explained from the fact that in the resonance region of the Drude metal surface plasmons can be excited, and these play the dominant role in transferring the electronic energy between the donor and the acceptor. The dependence of the energy transfer rate on the molecular transition frequency is investigated as well. For small intermolecular distances, the cylinder hardly affects the transfer rate, independent of frequency. At larger distances, the frequency dependence is quite strong, in particular in the stop-gap region. The role of the intermolecular distance in the frequency dependence may be explained qualitatively using the energy-time "uncertainty" relations to calculate the spread in the frequencies of the intermediate photons.

Published as *Phys. Rev. A*, **79**, 053816 (2009)

3.1 Introduction

In this chapter we investigate the modifications of the spontaneous emission rate of a molecule and the energy transfer rate between two molecules placed close to a metallic cylinder. The cylinder is a suitable model for a nanowire and a frequently used building block for 2D photonic crystals [96, 97]. The SE and ET rates are calculated using the Green's tensor method outlined in Section 1.3 of the Introduction. For calculating the Green's tensor of the cylinder, we employ the method of scattering superposition also outlined in the Introduction, specifically Subsection 1.4.1. We observe both enhancement and inhibition of the SE and ET rates as compared to their free-space values.

This chapter is organized as follows: in section 3.2 we give a derivation of the expression for the Green's tensor of an infinitely long dielectric cylinder, giving also a glimpse at its numerical implementation. Section 3.3 is dedicated to the results obtained and their discussion, while section 3.4 is reserved for conclusions.

3.2 The Green's Tensor for an infinite cylinder

3.2.1 Formalism

Consider a cylinder of radius a and complex dielectric function $\varepsilon(\mathbf{r}, \omega)$, coaxial with the z-axis and embedded in an infinite medium with a constant dielectric permittivity ε_b (b for background, see Fig. 3.1). Due to the cylindrical symmetry of the prob-

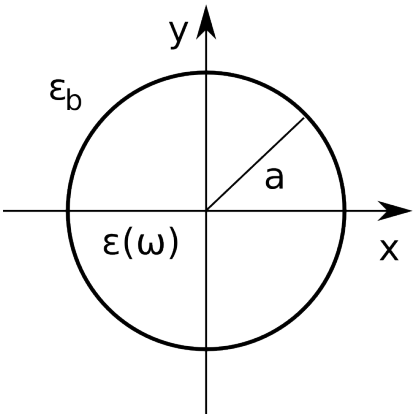

Figure 3.1: *Geometry of the cylinder in a dielectric background.*

lem, Cylindrical coordinates present a natural choice ($\mathbf{r} = (\rho, \theta, z)$ and $\mathbf{s} = (\rho_s, \theta_s, z_s)$, respectively). We have derived the expression for the Green's tensor in cylindrical coordinates and have arrived at formula (1.80). We can now apply the method of scattering superposition to find the Green's tensor for the geometry under consideration here. We write down the decomposition of the Green's tensor into the homogeneous and scattering part as follows:

$$\mathscr{G}(\mathbf{r},\mathbf{s},\omega) = \mathscr{G}_h(\mathbf{r},\mathbf{s},\omega) + \mathscr{G}_s(\mathbf{r},\mathbf{s},\omega). \tag{3.1}$$

Labeling the medium inside the cylinder by 1 and the medium outside it by 2, the above decomposition now takes the form

$$\begin{cases} \mathscr{G}^{(11)}(\mathbf{r},\mathbf{s},\omega) = \mathscr{G}_h^{(11)}(\mathbf{r},\mathbf{s},\omega) + \mathscr{G}_s^{(11)}(\mathbf{r},\mathbf{s},\omega) \\ \mathscr{G}^{(21)}(\mathbf{r},\mathbf{s},\omega) = \mathscr{G}_s^{(21)}(\mathbf{r},\mathbf{s},\omega) \end{cases}, \tag{3.2a}$$

$$\begin{cases} \mathscr{G}^{(12)}(\mathbf{r},\mathbf{s},\omega) = \mathscr{G}_s^{(12)}(\mathbf{r},\mathbf{s},\omega) \\ \mathscr{G}^{(22)}(\mathbf{r},\mathbf{s},\omega) = \mathscr{G}_h^{(22)}(\mathbf{r},\mathbf{s},\omega) + \mathscr{G}_s^{(22)}(\mathbf{r},\mathbf{s},\omega) \end{cases}, \tag{3.2b}$$

where the first superscript on the Green's tensor indicates the target position (acceptor molecule), while the second superscript indicates the source position (donor molecule). The homogeneous term in the above expressions has a simple expansion in terms of the Cylindrical vector wavefunctions (1.76), derived as Eq. (1.80). Given that the VWFs form a basis in Cylindrical coordinates, one is justified in expanding the scattering terms in Eqs. (3.2) in the same way. These expansions can be written as

$$\begin{aligned} \mathscr{G}_s^{(11)}(\mathbf{r},\mathbf{s},\omega) &= \frac{i}{8\pi}\sum_{n=-\infty}^{\infty}\int_{-\infty}^{\infty} \mathrm{d}k_z \frac{1}{k_{\rho 1}^2}\times \\ &\times\Big\{\Big[R_{MM}^{11}\mathbf{M}_n(k_{\rho 1},k_z,\mathbf{r}) + R_{NM}^{11}\mathbf{N}_n(k_{\rho 1},k_z,\mathbf{r})\Big]\otimes\mathbf{M}_n^*(k_{\rho 1},k_z,\mathbf{s}) + \\ &+\Big[R_{MN}^{11}\mathbf{M}_n(k_{\rho 1},k_z,\mathbf{r}) + R_{NN}^{11}\mathbf{N}_n(k_{\rho 1},k_z,\mathbf{r})\Big]\otimes\mathbf{N}_n^*(k_{\rho 1},k_z,\mathbf{s})\Big\}, \end{aligned} \tag{3.3a}$$

$$\begin{aligned} \mathscr{G}_s^{(21)}(\mathbf{r},\mathbf{s},\omega) &= \frac{i}{8\pi}\sum_{n=-\infty}^{\infty}\int_{-\infty}^{\infty} \mathrm{d}k_z \frac{1}{k_{\rho 1}^2}\times \\ &\times\Big\{\Big[R_{MM}^{21}\mathbf{M}_n^{(1)}(k_{\rho 2},k_z,\mathbf{r}) + R_{NM}^{21}\mathbf{N}_n^{(1)}(k_{\rho 2},k_z,\mathbf{r})\Big]\otimes\mathbf{M}_n^*(k_{\rho 1},k_z,\mathbf{s}) + \\ &+\Big[R_{MN}^{21}\mathbf{M}_n^{(1)}(k_{\rho 2},k_z,\mathbf{r}) + R_{NN}^{21}\mathbf{N}_n^{(1)}(k_{\rho 2},k_z,\mathbf{r})\Big]\otimes\mathbf{N}_n^*(k_{\rho 1},k_z,\mathbf{s})\Big\}, \end{aligned} \tag{3.3b}$$

$$\mathscr{G}_s^{(12)}(\mathbf{r},\mathbf{s},\omega) = \frac{i}{8\pi}\sum_{n=-\infty}^{\infty}\int_{-\infty}^{\infty} \mathrm{d}k_z \frac{1}{k_{\rho 2}^2}\times$$
$$\times\left\{\left[R_{MM}^{12}\mathbf{M}_n(k_{\rho 1},k_z,\mathbf{r}) + R_{NM}^{12}\mathbf{N}_n(k_{\rho 1},k_z,\mathbf{r})\right]\otimes\mathbf{M}_n^{(1)*}(k_{\rho 2},k_z,\mathbf{s}) + \right.$$
$$\left. + \left[R_{MN}^{12}\mathbf{M}_n(k_{\rho 1},k_z,\mathbf{r}) + R_{NN}^{12}\mathbf{N}_n(k_{\rho 1},k_z,\mathbf{r})\right]\otimes\mathbf{N}_n^{(1)*}(k_{\rho 2},k_z,\mathbf{s})\right\}, \tag{3.3c}$$

$$\mathscr{G}_s^{(22)}(\mathbf{r},\mathbf{s},\omega) = \frac{i}{8\pi}\sum_{n=-\infty}^{\infty}\int_{-\infty}^{\infty} \mathrm{d}k_z \frac{1}{k_{\rho 2}^2}\times$$
$$\times\left\{\left[R_{MM}^{22}\mathbf{M}_n^{(1)}(k_{\rho 2},k_z,\mathbf{r}) + R_{NM}^{22}\mathbf{N}_n^{(1)}(k_{\rho 2},k_z,\mathbf{r})\right]\otimes\mathbf{M}_n^{(1)*}(k_{\rho 2},k_z,\mathbf{s}) + \right.$$
$$\left. + \left[R_{MN}^{22}\mathbf{M}_n^{(1)}(k_{\rho 2},k_z,\mathbf{r}) + R_{NN}^{22}\mathbf{N}_n^{(1)}(k_{\rho 2},k_z,\mathbf{r})\right]\otimes\mathbf{N}_n^{(1)*}(k_{\rho 2},k_z,\mathbf{s})\right\}, \tag{3.3d}$$

where $k_{\rho 1} = \sqrt{k_1^2 - k_z^2}$, $k_{\rho 2} = \sqrt{k_2^2 - k_z^2}$, $k_1 = \omega\sqrt{\varepsilon_b}$ and $k_2 = \omega\sqrt{\varepsilon(\omega)}$. It should be noted that above expressions involve combinations of the **M** and **N** VWFs; the reason for this is that, in the presence of the cylinder, the normal modes of the field do not separate into pure TM and TE modes but have a hybrid nature. As we have pointed out in Section 1.4.2 of the Introduction, the superscript (1) on the VWFs denotes that the regular Bessel function of the first kind, J_n should be replaced by the Hankel function of the first kind, $H_n^{(1)}$, in order to satisfy the radiation condition at infinity. This radiation condition is already implicitly satisfied by the expressions in Eq. (3.3). The regularity condition of the Green's tensor at $\rho = 0$ is also implicitly satisfied by expanding the Green's tensor inside the cylinder only in terms of the Bessel functions J_n, which are regular at the origin.

In what follows, we shall give a detailed derivation of the expansion coefficients R that appear in the expressions above, for the case when the source molecule is located outside the cylinder (medium 2). To this end, we impose the following continuity conditions on the Green's tensor at the surface of the cylinder:

$$\hat{\boldsymbol{\rho}}\times\left[\mathscr{G}^{(12)}(\mathbf{r},\mathbf{s},\omega) - \mathscr{G}^{(22)}(\mathbf{r},\mathbf{s},\omega)\right]\Big|_{\rho=a} = 0, \tag{3.4a}$$

$$\hat{\boldsymbol{\rho}}\times\left[\nabla_{\mathbf{r}}\times\mathscr{G}^{(12)}(\mathbf{r},\mathbf{s},\omega) - \nabla_{\mathbf{r}}\times\mathscr{G}^{(22)}(\mathbf{r},\mathbf{s},\omega)\right]\Big|_{\rho=a} = 0. \tag{3.4b}$$

Unpacking these continuity conditions, one arrives at two inhomogeneous systems of linear equations, one for each of the two polarizations of the source molecule, TE and TM. In a shorthand, one can write these systems in matrix form as:

$$\Delta(n,k_z)\cdot\mathbf{R}_{M(N)}(n,k_z) = \mathbf{V}_{M(N)}(n,k_z), \tag{3.5}$$

where $\Delta(n,k_z)$ represents the characteristic matrix common to the two systems, $\mathbf{R}_M(n,k_z)$ and $\mathbf{R}_N(n,k_z)$ are the unknown coefficients vectors and $\mathbf{V}_M(n,k_z)$ and $\mathbf{V}_N(n,k_z)$ are the free term vectors. The expressions for the characteristic matrix, Δ is

$$\Delta = \begin{pmatrix} k_{\rho 1}^2 J_n(k_{\rho 1}a) & 0 & -k_{\rho 2}^2 H_n(k_{\rho 2}a) & 0 \\ 0 & \frac{k_{\rho 1}^2}{k_1} J_n(k_{\rho 1}a) & 0 & -\frac{k_{\rho 2}^2}{k_2} H_n(k_{\rho 2}a) \\ \frac{nk_z}{a} J_n(k_{\rho 1}a) & k_1 k_{\rho 1} J_n'(k_{\rho 1}a) & -\frac{nk_z}{a} H_n(k_{\rho 2}a) & -k_2 k_{\rho 2} H_n'(k_{\rho 2}a) \\ k_{\rho 1} J_n'(k_{\rho 1}a) & \frac{nk_z}{k_1 a} J_n(k_{\rho 1}a) & -k_{\rho 2} H_n'(k_{\rho 2}a) & -\frac{nk_z}{k_2 a} H_n(k_{\rho 2}a) \end{pmatrix}, \quad (3.6)$$

while the unknown coefficient and free term vectors are given by:

$$\mathbf{R}_M = \begin{pmatrix} R_{MM}^{12} \\ R_{NM}^{12} \\ R_{MM}^{22} \\ R_{NM}^{22} \end{pmatrix}, \mathbf{R}_N = \begin{pmatrix} R_{MN}^{12} \\ R_{NN}^{12} \\ R_{MN}^{22} \\ R_{NN}^{22} \end{pmatrix}, \mathbf{V}_M = \begin{pmatrix} -k_{\rho 2}^2 J_n \\ 0 \\ -\frac{nk_z}{a} J_n \\ -k_{\rho 2} J_n' \end{pmatrix}, \mathbf{V}_N = \begin{pmatrix} 0 \\ -\frac{k_{\rho 2}^2}{k_2} J_n \\ -k_2 k_{\rho 2} J_n' \\ -\frac{nk_z}{k_2 a} J_n \end{pmatrix}, \quad (3.7)$$

where the argument of the Bessel J_n functions in the free term vectors is $k_{\rho 2}a$. All the individual quantities in expressions (3.6) and (3.7) can be easily calculated, and one can, therefore, calculate the expansion coefficients from (3.3), and hence the Green's tensor in the presence of the cylinder. A completely analogous calculation can be undertaken for the case where the source point $\mathbf{s}$ is located inside the cylinder, i.e. in medium 1.

As an example of the form that the components of the scattering term in the Green's tensor take, we give its zz-component for the case when the source point is outside the cylinder, and the field point is inside it:

$$\mathscr{G}_{s(zz)}^{(12)}(\mathbf{r},\mathbf{s},\omega) = \frac{i}{8\pi} \sum_{n=0}^{\infty} \int_{-\infty}^{\infty} \mathrm{d}k_z (2-\delta_0) \frac{k_{\rho 1}^2}{k_1 k_2} R_{NN}^{12} J_n(k_{\rho 1}\rho) H_n(k_{\rho 2}\rho_s) \cos(n\theta)\, \mathrm{e}^{ik_z z}, \quad (3.8)$$

where $\delta_0 = 1$ if $n = 0$ and $\delta_0 = 0$ otherwise. In this expression, we have made several simplifications which we shall briefly discuss. First of all, the integrand does not depend on θ_s and z_s; this is due to the rotational symmetry around the cylinder's axis and the translational symmetry along this axis. Hence, we can choose the coordinate system we use such that $\theta_s = z_s = 0$. Furthermore, the integrand in Eq. (3.3c) is even in

n, and therefore the summation from $n=-\infty$ to ∞ can be replaced with a summation from $n=0$ to ∞, which leads to the cosine function in Eq. (3.8).

The double-valued nature of the square root in $k_\rho = \sqrt{k^2-k_z^2}$ generates branch cuts in the complex k_z plane, defined by $\mathrm{Im}(k_\rho)=0$. There are two branch cuts, corresponding to $k_{\rho 1}$ and $k_{\rho 2}$, each branch cut starting in a branch point at $k_z=\pm k_1$ and $k_z=\pm k_2$ and spanning the real axis towards $\pm\infty$. When performing the k_z integration, we need to choose a path around the branch cut such that the Sommerfeld radiation condition is satisfied, i.e. the integrand vanishes at infinity. The proper path runs below the real axis [37].

In addition to the branch points and branch cuts mentioned above, the integrand in Eq. (3.8) can also have poles due to the scattering coefficient R_{NN}^{12}. Denoting these poles by k_{zp}, they correspond to scattering resonances or *whispering gallery modes* (WGMs) when $\mathrm{Re}(k_{zp}) \leqslant k_2$, to *guided modes* when $k_2 < \mathrm{Re}(k_{zp}) \leqslant k_1$ and to SPPs when $\mathrm{Re}(k_{zp}) > k_1, k_2$. This statement assumes that $|k_2| < |k_1|$.

In the following subsection we focus on the numerical calculation of the Green's tensor.

3.2.2 Numerical implementation

Due to the rather complicated form of the expansion coefficients of the scattering terms, calculations can only be performed numerically. Furthermore, since the homogeneous part of the Green's tensor has a specific analytical expression (see also (1.55)):

$$\mathscr{G}_h^{ij}(\mathbf{r},\mathbf{s},\omega) = -\frac{1}{k^2}\frac{\mathrm{e}^{ikR}}{4\pi R^3}\left[(1-ikR)(\delta_{ij}-3\hat{R}_i\hat{R}_j)-k^2R^2(\delta_{ij}-\hat{R}_i\hat{R}_j)\right] \tag{3.9}$$

with $\mathbf{R}=\mathbf{r}-\mathbf{s}$, we only need to calculate numerically the scattering part of the Green's tensor.

Numerically the task consists in performing one integration and a summation (see Eqs. (3.3)). The integrand in this expression is symmetric in k_z and we can "fold" the integral so that we integrate only from 0 to ∞. As mentioned in the previous subsection, to satisfy the radiation condition, we must choose a contour that runs *below* the real axis, in the fourth quadrant of the complex k_z-plane towards ∞. Because of the existence of poles in the first quadrant and close to the real axis in the region $k_z < k_\rho$, we choose the contour shown in Fig. 3.2 [37].

As observed above, the summation also exhibits a symmetry with respect to n (the multipole order) and can thus be "folded". The number of terms required for the series to converge depends strongly on the position of the two molecules: the closer they are to the boundary of the cylinder, the more terms are needed. We stop the summation

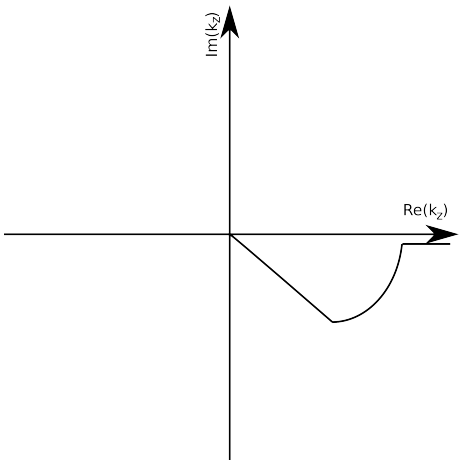

Figure 3.2: *Integration contour in the complex k_z-plane.*

when the relative error satisfies the criterion:

$$\frac{|\mathscr{G}_{N_m+1} - \mathscr{G}_{N_m}|}{|\mathscr{G}_{N_m}|} \leqslant 10^{-6}.$$

Here N_m is the number of multipole terms already included in the summation. The maximum number of multipole terms needed for the criterion above to be satisfied ranges from less than 10 when the molecules are far away from the cylinder's surface to a few hundred when the molecules are close both to each other and to the cylinder.

We have tested this method by calculating the relative SE rate of a molecule in this geometry. In terms of the Green's tensor, the emission rate of a molecule is given by Eq. (1.34). Using this expression (with a constant $\varepsilon(\omega) = 2.0$ and $\varepsilon_b = 1.0$) we have obtained results that are numerically indistinguishable from the ones reported in Ref. [22] where a mode expansion method was employed to calculate the spontaneous emission rate.

3.3 Results and Discussion

Using the formalism presented above, we calculate the energy transfer rate between two molecules placed near a cylinder. We consider two different cases, namely a frequency-independent dielectric function (Subsection 3.3.1) and a metal with a Drude dielectric function (Subsection 3.3.2 and 3.3.3). In all cases considered, the

two molecules are located in the same xy-plane perpendicular to the cylinder axis. The results will be presented by giving the normalized energy transfer rate $\tilde{\Gamma}$ defined in Eq. (1.54). In most plots this is done by keeping one of the molecules – the donor – fixed at some position on the x-axis and scanning the other molecule – the acceptor – throughout the xy-plane (outside and inside the cylinder). All results reported here were obtained for transition dipoles (of both molecules) oriented along the cylinder axis. Changing these orientations does not lead to qualitatively different conclusions.

3.3.1 Frequency-independent dielectric permittivity

We first consider the energy transfer rate for cylinders of real and frequency-independent dielectric function $\varepsilon(\omega) = 2.0$. In this case, the natural length scale in the problem is the vacuum wavelength of the $0-0$ transition of molecule A, $\lambda_0 = 2\pi/\omega_A$.

Fig. 3.3 shows the relative ET rate $\tilde{\Gamma}$ between two molecules for four different cylinder radii, (a) $a = 0.20\,\lambda_0$, (b) $a = 0.50\,\lambda_0$, (c) $a = 1.00\,\lambda_0$, and (d) $a = 2.00\,\lambda_0$. In all cases, the donor molecule (indicated by the white cross) is placed on the x-axis outside the cylinder, close to its surface, at $\rho_s = 0.22\,\lambda_0$, $0.55\,\lambda_0$, $1.05\,\lambda_0$, and $2.2\,\lambda_0$ respectively. As is observed, $\tilde{\Gamma}$ may be larger or smaller than unity, implying that both enhancement and reduction of the transfer rate are possible due to the presence of the cylinder. With increasing cylinder radius, a number of interesting "hot-spots" – places where the rate is increased appreciably – is observed centered at the surface of the cylinder. Clearly, these hot-spots result from interference of the various direct and scattered waves. Interference effects are expected to arise when the differences in the lengths of various electromagnetic propagation pathways between donor and acceptor are of the order of the typical wavelength of these intermediate waves. This explains why the number of hot-spots grows with the cylinder's circumference. The presence of focusing points on the boundary of the cylinder is similar to the focusing effect of the interaction between two molecules placed at antipodal positions near a dielectric sphere [60].

We notice that the typical distance between hot-spots is of the order of $\lambda_0/2$, implying that λ_0 defines the typical scale for the intermediate waves. At first sight, this may seem quite natural, but it should be kept in mind that the intermediate photons do not necessarily conserve energy, as they only live for a short time (see Introduction). In order to estimate the minimal spread in photon energies, we consider the maximum travel distance between donor and acceptor close to the cylinder's surface. The photon travel time for this distance is πa. Using the energy-time "uncertainty" relation $\Delta\omega\Delta t \approx \pi$, this results in a spread of frequencies of the intermediate photons of the order of $\Delta\omega = 1/a$, which in turn translates into a spread in the wavelength of the intermediate photons given by $\Delta\lambda = \lambda^2/(2\pi a)$. Using $\lambda = \lambda_0$ as the central wavelength for the intermediate photons, we arrive at $\Delta\lambda \approx 0.8\,\lambda_0$ for $a = 0.2\,\lambda_0$ and

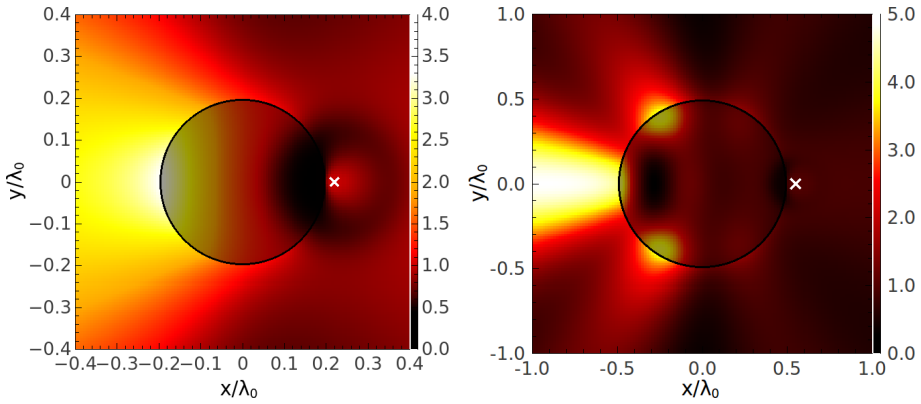

(a) $a = 0.2\,\lambda_0$, $\rho_s = 0.22\,\lambda_0$ **(b)** $a = 0.5\,\lambda_0$, $\rho_s = 0.55\,\lambda_0$

(c) $a = 1.0\,\lambda_0$, $\rho_s = 1.10\,\lambda_0$ **(d)** $a = 2.0\,\lambda_0$, $\rho_s = 2.20\,\lambda_0$

Figure 3.3: *Relative energy transfer rate between two molecules placed near a dielectric cylinder ($\varepsilon = 2$) with (a) $a = 0.2\,\lambda_0$, $\rho_s = 0.22\,\lambda_0$, (b) $a = 0.5\,\lambda_0$, $\rho_s = 0.55\,\lambda_0$, (c) $a = 1.0\,\lambda_0$, $\rho_s = 1.10\,\lambda_0$ and (d) $a = 2.0\,\lambda_0$, $\rho_s = 2.20\,\lambda_0$. Both the donor and the acceptor transition dipole moments are oriented along the z-axis.*

$\Delta\lambda \approx 0.08\,\lambda_0$ for $a = 2\,\lambda_0$. From this we conclude that the distribution of photons contributing to the energy transfer in the case $a = 0.2\,\lambda_0$ is very broad. For $a = 2\,\lambda_0$ this distribution is relatively narrow already and the central wavelength λ_0 may well be used to rationalize interference effects.

The enhancement of the energy transfer rate in the various hot-spots near the circumference increases with increasing cylinder radius (from $\tilde{\Gamma} \approx 3$ for $a = 0.2\,\lambda_0$ to $\tilde{\Gamma} \approx 12$ for $a = 2\,\lambda_0$). This may be explained by the fact that for increasing radius,

the spread in intermediate wavelengths decreases, leading to better defined interference patterns. Similarly, the fact that hot-spots are much less pronounced (or barely present) on the donor's side of the cylinder, may also be explained from a larger spread in wavelength, owing to the smaller distances between donor and acceptor.

The enhancement of energy transfer at specific points near the circumference is of potential interest for sensing and microscopy applications. It should be noticed, however, that the vacuum (Förster) transfer rate over distances of 100 nm or more is very small for most donor-acceptor pairs, implying that even after enhancement it may be difficult to observe energy transfer across the cylinder, except for truly narrow cylinders, $a \lesssim 0.1\,\lambda_0$.

To conclude this section, we illustrate the intricate build-up of the hot-spot pattern by considering contributions from individual multipole orders n to the Green's tensor $\mathscr{G}_s$, Eq. (3.8). Fig. 3.4 shows these contributions to the total rate for $n = 3$ and $n = 5$ for a cylinder of radius $a = 0.2\,\lambda_0$, placing the donor at $\rho_s = 0.22\,\lambda_0$. As before, the result is normalized to the (total) energy transfer rate for the same molecules in the absence of the cylinder. Of course, the individual multipole terms are dominated by the $\cos^2 n\theta$ factor, leading to $2n$ nodes in the enhancement patterns near the circumference. More surprising are the enormous enhancements seen for individual multipole orders (10^3 and more for the current case). Only after summing over tens of multipole contributions, does one converge to the full pattern, where (for $a = 0.2\,\lambda_0$, $\rho_s = 0.22\,\lambda_0$) only one clear (antipodal) hot-spot occurs with a modest enhancement of a factor of 3 (cf. Fig. 3.3a). We have found that this convergence occurs faster for larger radii.

To gain mathematical insight into the interference effect responsible for the cancellation of the large enhancement observed for individual multipole terms, we rewrite Eq. (3.8) as:

$$\mathscr{G}^{(12)}_{s(zz)}(\mathbf{r},\mathbf{s},\omega) = \frac{i}{8\pi}\sum_{n=0}^{\infty}\frac{2-\delta_0}{k_1 k_2}\cos(n\theta) f_n(\rho,\rho_s,z), \tag{3.10}$$

where

$$f_n(\rho,\rho_s,z) = \int_{-\infty}^{\infty} \mathrm{d}k_z \mathrm{e}^{ik_z z} k_{\rho 1}^2 R^{12}_{NN} J_n(k_{\rho 1}\rho) H_n(k_{\rho 2}\rho_s). \tag{3.11}$$

From the numerical calculations that we have performed, we find that the function $f_n(\rho,\rho_s,z)$ is a slowly varying and monotonous function of n. In addition, it has no θ dependence, this being exclusively embodied in the $\cos(n\theta)$ term in Eq. (3.10). Hence, for a fixed θ, the interference is given predominantly by the cos term. For $\theta = 0$ the successive terms in Eq. (3.10) interfere constructively and it would be expected that the largest enhancement of the energy transfer rate would occur for $\theta = 0$. In fact, from Fig. 3.3a it can be seen that the largest enhancement of the energy transfer rate actually occurs for $\theta = \pi$ where $\cos(n\theta) = \cos(n\pi) = \pm 1$ and the successive multipole terms have alternating sings.

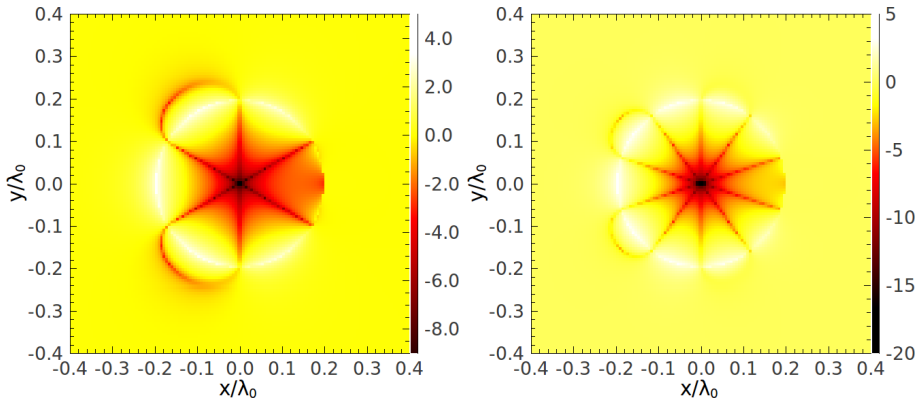

(a) $n = 3$ **(b)** $n = 5$

Figure 3.4: *Energy transfer rate through individual multipole terms between two molecules placed near a cylinder of radius $a = 0.2\lambda_0$, normalized to the total energy transfer rate in free-space. The dielectric constant is $\varepsilon = 2.0$. (a) The multipole term of order $n = 3$; (b) The multipole term of order $n = 5$. The color map is logarithmic in scale.*

This fact can easily be explained if we keep in mind that what is plotted in Fig. 3.3a is the relative energy transfer rate, normalized to its value in free-space. For $\theta = 0$ the different multipole terms do indeed interfere constructively and this is the position where the *absolute* energy transfer rate has its maximum value. However, the free-space energy transfer rate at this position is also large (it behaves as R^{-6} for the distances involved in this particular example) and hence the relative energy transfer rate is small. On the other hand, when $\theta = \pi$, the successive multipole terms cancel each other almost completely, due to the weak dependence of f_n on n. What remains after this cancellation is of the order of the energy transfer rate in free-space at that distance, giving the modest enhancement of the total normalized energy transfer rate observed in Fig. 3.3a.

3.3.2 Drude dielectric permittivity

A more realistic model for the dielectric properties of the cylinder is to use a complex, frequency-dependent dielectric permittivity. As an example, we use the Drude form of Eq. (1.81)

$$\varepsilon(\omega) = 1 - \frac{\omega_P^2}{\omega^2 + i\gamma\omega}, \tag{3.12}$$

where ω_P is the plasma frequency. In this case we shall express all the relevant lengths, including the transition wavelength of the molecules, λ_0, in terms of the plasma wavelength, $\lambda_P = 2\pi/\omega_P$, of the Drude model. We have chosen the medium outside the cylinder to have a constant dielectric permittivity of $\varepsilon_b = 4.0$.

We calculate the energy transfer rate between two molecules placed near a Drude metallic cylinder with $\gamma = 2.288 \cdot 10^{-3}\,\omega_P$, for a transition frequency of $\omega = 0.40\,\omega_P$. At this frequency, the dielectric permittivity has the value $\varepsilon(\omega) \approx -5.25 + i0.03$. The relative ET rate for two cylinder radii, $a = 0.2\,\lambda_P$ and $a = 1.0\,\lambda_P$, is presented in Fig. 3.5 (linear scale in the upper panels and logarithmic scale in the lower ones).

As is observed, the enhancement of the energy transfer rate due to the presence of the cylinder now reaches values that are considerably higher (up to a factor of 10^5) than in the case of a constant ε (cf. Fig. 3.3). Moreover, the pattern of the enhancement is also changed, being peaked around the cylinder's circumference much more sharply than in Fig. 3.3 and more reminiscent of individual multipole patterns.

The reason for the large enhancements in a narrow shell around the cylinder lies in the role of surface plasmon-polaritons. As mentioned in the Introduction, these localized waves can be excited at the interface between a Drude metal with a dielectric permittivity $\varepsilon(\omega)$ given by Eq. (3.12) and a dielectric medium ($\varepsilon_b = 4.0$ in this case), in the frequency interval $\omega < \omega_{\rm SP}$, with $\omega_{\rm SP} = \omega_P/\sqrt{1+\varepsilon_b} = \omega_P/\sqrt{5} \approx 0.447\,\omega_P$ [98]. The transition frequency we have used in the calculations for Fig. 3.5, $\omega = 0.40\,\omega_P$, lies very close to the surface plasmon frequency, $\omega_{\rm SP} \approx 0.447\,\omega_P$, and it is close to this upper limit that we expect the effect of the SPPs to be more apparent. The amplitude of the SPPs drops off exponentially, both inside the cylinder, as well as outside it, with a length scale given by the inverse of the imaginary part of the propagation constant in the direction perpendicular to the interface ($\mathrm{Im}\,k_\rho$ in the case of the cylinder) [64]. For the parameters considered here, at $\omega = 0.4\,\omega_P$, the decay distances of the field amplitude on both sides of a planar interface equal roughly $0.20\,\lambda_P$; this implies a decay distance of $0.04\,\lambda_P$ for the square of the amplitude, which is the relevant quantity for the energy transfer rate. The contribution of surface plasmons to the energy transfer rate between two molecules was first recognized by Philpott [98] for the case of a planar interface.

In both situations considered in Fig. 3.5, the donor is located within the decay distance of the amplitude squared from the cylinder surface. As in this range the amplitudes of the surface plasmons are much larger than those of the extended waves, the donor preferentially excites the former. These intermediate surface plasmons have a high interaction cross section with acceptors that are placed within their decay range. This explains both the large value of the maximal enhancements and the sharp nature of the hot-spots. Making cross sections perpendicular to the cylinder's surface through the enhancement patterns of Fig. 3.5, reveals that the hot-spots decay exponentially when moving away from the cylinder, with a decay distance of the order of $0.04\lambda_P$.

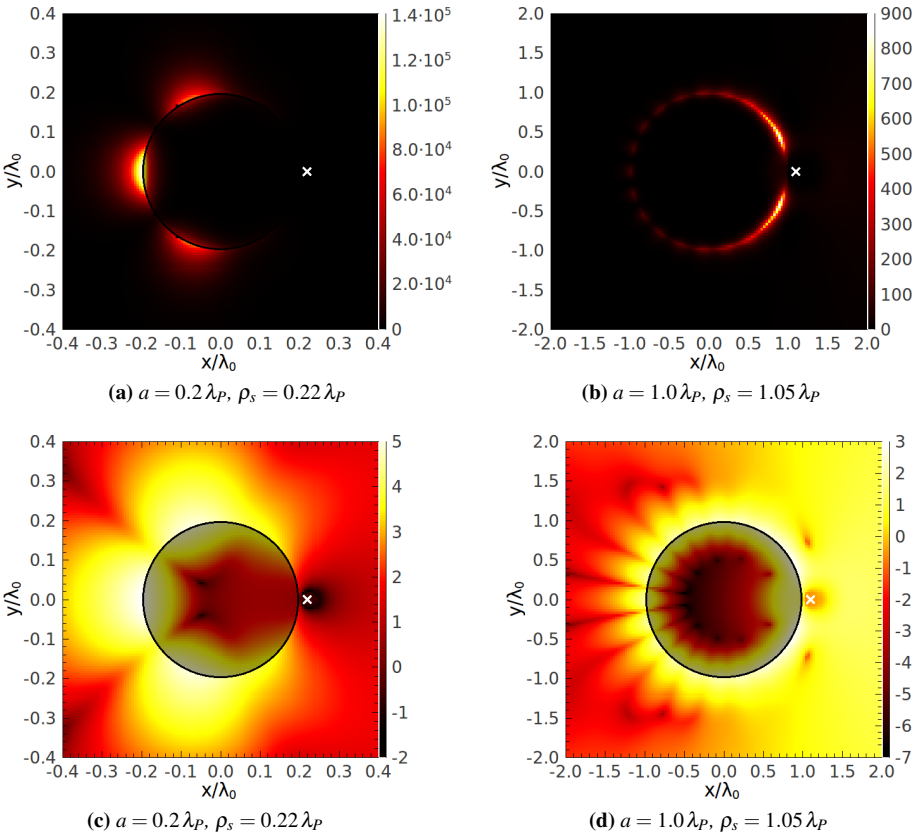

(a) $a = 0.2\,\lambda_P$, $\rho_s = 0.22\,\lambda_P$ **(b)** $a = 1.0\,\lambda_P$, $\rho_s = 1.05\,\lambda_P$

(c) $a = 0.2\,\lambda_P$, $\rho_s = 0.22\,\lambda_P$ **(d)** $a = 1.0\,\lambda_P$, $\rho_s = 1.05\,\lambda_P$

Figure 3.5: *Relative energy transfer rate between two molecules placed near a cylinder with a Drude dielectric permittivity, Eq.* (3.12)*, with* $\gamma = 2.288 \times 10^{-3}\,\omega_P$*. Both the donor and the acceptor are oriented along the z-axis. (a)* $a = 0.2\,\lambda_P$*,* $\rho_s = 0.22\,\lambda_P$ *and (b)* $a = 1.0\,\lambda_P$*,* $\rho_s = 1.05\,\lambda_P$*. Panels (c) and (d) are the logarithmic correspondents of (a) and (b), respectively.*

This cross width of the hot-spots agrees well with the above quoted decay distance for the amplitudes of the surface plasmons, lending further support to the conjecture that these are responsible for the enhancement patterns observed.

Figs. 3.6 shows the dispersion relation of SPPs on a cylinder of radii $a = 0.20\,\lambda_P$ and $a = 1.00\,\lambda_P$, respectively. In these figures we have plotted the dispersion relations for SPPs for several orders $n = 0, \ldots, 5$. We see that only the $n = 0$ SPP reaches $\omega = 0$ for $k_\rho = 0$. All higher order modes intersect the light-line in the dielectric at a finite $\omega_{n0} \neq 0$, which grows with n. For the cylinder of radius $a = 0.2\,\lambda_P$, we see that

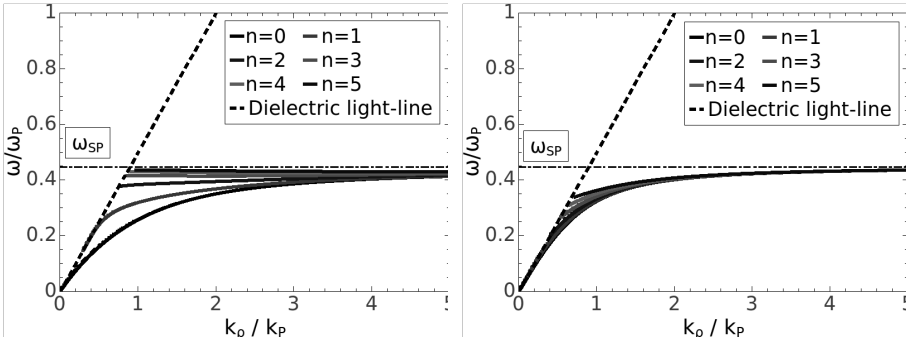

(a) $a = 0.2\,\lambda_P$ **(b)** $a = 1.0\,\lambda_P$

Figure 3.6: *Dispersion relations of SPPs on Drude cylinders of radii (a) $a = 0.2\,\lambda_P$ and (b) $a = 1.0\,\lambda_P$, in a dielectric environment with $\varepsilon_b = 4.0$.*

the dispersion relations for the SPPs with $n > 2$ lie completely above the transition frequency of the donor molecule used in our calculations, $\omega = 0.4\,\omega_P$. As such, the donor molecule cannot excite these SPPs and they do not contribute to the ET rate between the donor and acceptor molecules along the surface of the cylinder. The dispersion curves of SPPs on the larger cylinder, $a = 1.0\,\lambda_P$, on the other hand, are spaced much closer together, and they intersect the $\omega = 0.4\,\omega_P$ frequency line up to larger orders, $n > 10$. The donor molecule can, therefore, excite these additional SPPs, and they do contribute to the ET rate along the surface of the cylinder.

The total ET rate between donor and acceptor is primarily determined by the interference between the SPPs that the donor can excite. We have ascertained this by performing partial multipole sums – summing only the first n multipole terms in the series expansion (3.8) – and observing that the series converges after $n = 2$ for $a = 0.2\,\lambda_P$ and $n \approx 10$ for $a = 1.0\,\lambda_P$. Additional multipole terms above these values do not change the pattern of hot-spots, but they do slightly smooth out the sharp peaks in the ET rate close to the surface of the cylinder.

3.3.3 Frequency-dependence of the energy transfer rate

In the previous subsection all calculations were performed for the case of a Drude dielectric permittivity at a specific transition frequency, $\omega = 0.4\,\omega_P$. It is interesting to know how the energy transfer rate depends on this frequency, in particular how sensitive it is to the value of ω relative to the stop-gap and what is the role played by the distance between donor and acceptor. In this subsection we present the results of such calculations.

We consider a cylinder of radius $a = 0.2\,\lambda_P$ and two molecules placed near it, both at a distance $\rho = \rho_s = 0.22\,\lambda_P$ from the cylinder's axis. Fig. 3.7 shows the energy transfer rate as a function of frequency for intermolecular distances $d = 0.001\,\lambda_P$, $0.01\,\lambda_P$, $0.1\,\lambda_P$ and $0.2\,\lambda_P$. In all cases, the frequency range considered extends from

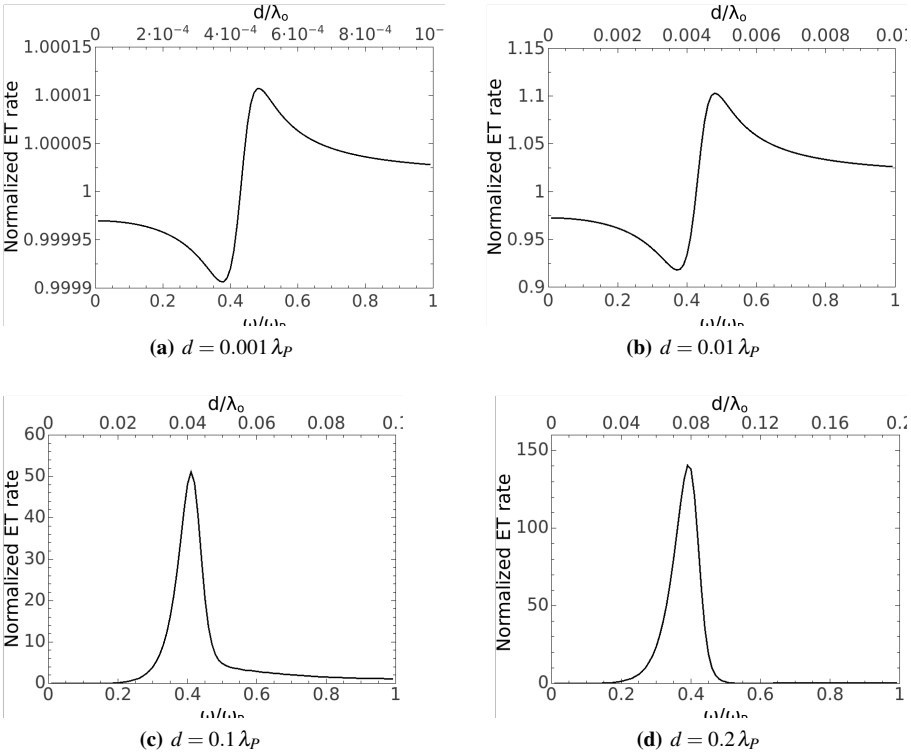

(a) $d = 0.001\,\lambda_P$ **(b)** $d = 0.01\,\lambda_P$

(c) $d = 0.1\,\lambda_P$ **(d)** $d = 0.2\,\lambda_P$

Figure 3.7: *Relative energy transfer rate as a function of frequency for fixed distance to the cylinder's surface ($\rho = \rho_s = 0.22\,\lambda_P$) and several intermolecular distances. Other relevant parameters: $a = 0.2\,\lambda_P$ and $\gamma = 0.1\,\omega_P$. The ET rates are normalized to a homogeneous medium with $\varepsilon_b = 4$.*

$\omega = 0$ to $\omega = \omega_P$, encompassing the stop-gap. The distance between the two molecules in terms of their transition wavelength, $d/\lambda_0 = (\omega/\omega_P)(d/\lambda_P)$, is given on the top x-axis. We have chosen a linewidth $\gamma = 0.1\,\omega_P$ which is larger than the one used in the previous section, in order to make the features of Fig. 3.7 less sharp and easier to see. No qualitative changes occur due to increasing γ.

As is observed from Fig. 3.7, for small intermolecular separations the modification of the energy transfer rate induced by the presence of the dielectric cylinder is very

small for all frequencies. The effect of the cylinder increases with growing separation in particular in the stop-gap region of the spectrum. In the first two panels of Fig. 3.7, the distance between the molecules is smaller than their distance to the cylinder's surface, and also than the transition wavelength of the donor, λ_0. Because of this, the homogeneous term in the Green's tensor is in its d^{-6} dependence regime. The scattering term, on the other hand, depends on the positions of the two molecules relative to the cylinder's axis ($\rho = \rho_s = 0.22\,\lambda_P$) and on the cylinder's radius ($a = 0.2\,\lambda_P$) and is much smaller than the homogeneous term, giving therefore a small contribution to the energy transfer rate. The normalized rate for this case, when both molecules are in the vacuum outside the cylinder, will be very close to unity. One could say that, in this particular arrangement, the molecules exchange their excitation before they have time to notice the presence of the cylinder nearby.

If the distance between the two molecules is increased (Figs. 3.7c and 3.7d) the homogeneous term of the Green's tensor will decrease as d^{-6} while the scattering term will be roughly constant (we keep ρ, ρ_s, and a constant, and we only modify θ); hence, the relative contribution of this scattering term increases in importance. This underlies the quite dramatic change in the normalized transfer rate for ω close to the surface plasmon frequency ω_{SP}, even for distances as small as $d = 0.1\,\lambda_P$ and $d = 0.2\,\lambda_P$. In this case, the presence of the cylinder is felt very strongly by the two molecules and it is predominantly through excitation of surface plasmons on the surface of the cylinder that they transfer the excitation between them. This is illustrated by the sharp peaks in the normalized energy transfer rate for these distances, close to ω_{SP}. As we have seen in the previous subsection 3.3.2, surface plasmons dominate the energy transfer between donor and acceptor if both are placed close to the cylinder's surface.

This behaviour of the energy transfer rate is in qualitative accordance with what one would expect to obtain using the heuristic approach of the energy-time "uncertainty" relations described in the Introduction. If the separation between the two molecules is much smaller than the wavelength associated with their optical transition, the permissible spread in the frequency of the virtual photons exchanged between them is large. In fact it can be as large as or larger than the frequency interval over which the dielectric function varies appreciably, i.e. the band width of the surface plasmons, with the result that contributions from photons of different frequencies will, in general, cancel each other, leading to a smoothing of the dependence of the energy transfer rate on frequency. This is well illustrated in Figs. 3.7a and 3.7b where the intermolecular separation is less than 2% of the transition wavelength. As soon as the intermolecular separation increases (Figs. 3.7c and 3.7d), the virtual photon frequencies span a smaller interval and the energy transfer rate becomes more sensitive to the dielectric properties at or close to the molecular transition frequency. This accounts for the fact that the frequency-dependence of the energy transfer rate is less smooth at these separations, in particular if the molecular transition is close to a resonance – the

surface plasmon frequency ω_{SP} in this case.

3.4 Summary and Conclusions

In this Chapter, we have calculated the rate of incoherent electronic energy transfer between two molecules in the presence of a circular cylinder. We have calculated the Green's tensor of the cylinder using the methods of vector wave functions and scattering superposition outlined in the Introduction. Two distinct cases were analyzed, one with a nondispersive dielectric cylinder with $\varepsilon = 2$ and one using a Drude model for the material of the cylinder. We have found large differences between these two models as regards the ET rate of molecules.

In all cases we have found that the presence of the cylinder may enhance the energy transfer rate at certain hot-spots on the cylinder's surface. In the case of a real dielectric permittivity, these hot-spots are rather weak (enhancements smaller than 10 for the cases considered), and separated by about half the transition wavelength of the molecules. They are clearly the result of interference of various waves on the dielectric interface. We expect that the net picture is that whispering gallery modes, generated by such interference effects, play a dominant role in the occurrence of the hot-spots, but this is difficult to corroborate, as the Green's tensor method does not enable us to separate contributions from different classes of intermediate photons used to exchange the energy.

For a Drude dielectric permittivity, the enhancement values are much larger (up to six orders of magnitude) and the hot-spots are localized much more sharply on the cylinder's surface. We have shown that surface plasmons, which occur in an energy interval within the stop-gap of the Drude model, are responsible for these high and sharply peaked enhancement patterns. Both the width of the hot-spots measured perpendicular to the surface and the fact that they disappear for growing cylinder radius when moving away from the donor molecule, can be explained quantitatively from the dominant role of surface plasmons. We have also found that for small separations between donor and acceptor molecules the effect of the cylinder is small, independent of the position of the molecular transition frequency relative to the stop-gap. This may be attributed to the fact that for small separations the direct interaction between donor and acceptor is more important than scattering contributions. On the other hand, for increasing donor-acceptor distance (if both molecules are still close to the cylinder), the effect can be very large. The enhancement of the transfer rate due to the cylinder then is strongly frequency dependent and peaks at the surface plasmon frequency, ω_{SP}. These observations are in qualitative agreement with heuristic arguments based on the energy-time "uncertainty" relations that small (large) transfer distances require a broad (narrow) distribution of photons used to exchange the energy. For small distances, this smooths out any structure in the frequency dependence of the dielectric

properties, effectively returning to the vacuum situation.

While in our theory we used a particular form of the dielectric permittivity (the Drude model), it should be pointed out that our general approach may be applied to any form of $\varepsilon(\omega)$. For a given cylinder material with known $\varepsilon(\omega)$, one may simply use its tabulated or parametrized form in the numerical analysis to evaluate the normalized transfer rate. The analysis is not complicated by this in any particular way. Because, as far as we know, no experiments have been performed to probe intermolecular energy transfer near cylinders, we have chosen the generic Drude model in our studies, which allows for the existence of surface plasmons and, thus, for the most interesting effects we have predicted. We thus believe that these effects are generic, and may indeed be observed in experiment. One issue which in a comparison to experiment should be kept in mind, is that in defining the normalized transfer rate $\tilde{\Gamma}$ (Eq. (1.54)), we have assumed that the Green's tensor does not vary appreciably over the frequency range of the emission and absorption linewidths of the molecules considered. For molecules with broad spectra, this may easily be corrected by first integrating the energy transfer rate over the spectra (Eq. (1.50)), before normalizing it.

Finally, we note that the predicted occurrence of localized hot-spots in the normalized energy transfer rate may be of interest for microscopy and sensing devices based on electronic energy transfer [99, 100]. This holds in particular if one can make use of the huge enhancements that may arise due to surface plasmons.

CHAPTER 4

Intermolecular interactions and energy transfer in Photonic Crystal Slabs

Abstract

In this Chapter we consider the decay and energy transfer rates in a square and triangular lattice Photonic Crystal Slab (PhCS) of cylindrical air-holes in a dielectric host placed on top of a gold (Au) substrate. Using FDTD methods, we calculate the modification of the decay rate of a molecule and the energy transfer rate between molecules placed inside the Photonic Crystal Slab and we investigate the effect of the band-structure of the Photonic Crystal Slab and of the surface plasmon-polaritons excited at the surface of the Au substrate on these rates. We find that, in the absence of the Au substrate, the existence of band-gaps in the band-structures leads to a suppression of the spontaneous decay rate of a quantum emitter whose emission frequency lies inside these band-gaps. The addition of the Au substrate enhances the decay rate of the emitter at the surface plasmon-polariton frequency, even when this frequency lies inside the band-gap of the Photonic Crystal Slab. When considering the energy transfer rate between molecules located inside a Photonic Crystal Slab, we find that energy transfer between distant molecules is suppressed inside the band-gap, but when the molecules are brought closer to one another, the effect of the band-gap gradually disappears, owing to the virtual nature of the photons that exchange the energy over short distances.

In preparation

4.1 Introduction

The history of *Photonic Crystals* (PhCs) begins, strictly speaking, with the introduction of the term by Yablonovitch and John [101, 102] in 1987. Before this time, it was Lord Rayleigh who began the study of periodic multi-layered structures (one-dimensional PhCs) and showed that they exhibit a one-dimensional band-gap [103]. Later on, a more in-depth theoretical study of one-dimensional structures was performed by Bykov [104, 105] in the context of the spontaneous emission of an atom embedded in such a structure. These ideas began to gain traction only after the publication of Yablonovitch's and John's papers and, since then, research in Photonic Crystals has advanced by leaps and bounds, fueled in part by the numerous applications these structures have in optical communications and information processing. PhCs are periodic dielectric structures, whose period is comparable to the wavelength of electromagnetic radiation. This periodic modulation of the dielectric properties plays the same role for photons as the regular crystalline structure of a semiconductor does for electrons: it gives rise to discrete bands in the dispersion diagram of light in the structure [106–108]. It can also introduce band-gaps in the dispersion diagram of a PhC, where no light propagation in certain directions is permitted for frequencies inside the band-gap. These band-gaps can be either partial, existing only for certain propagation directions (e.g. the guided-mode band gaps we shall discuss later), or complete, in the sense that they hold for every direction of propagation and frequencies inside the band-gap. The existence of total or partial band-gaps can, therefore, greatly influence the electromagnetic properties of atoms and molecules placed inside these PhC structures.

The spontaneous decay rate of quantum emitters is directly proportional to the *local density of states* of the electromagnetic field at the position of the emitter. When considering this in the light of the existence of band-gaps in periodic structures, where the density of states vanishes, much work has been done, both theoretically and experimentally, that shows the effect of periodic structures on the spontaneous decay rate of emitters [33–36, 109–120].

As far as the transfer of energy between molecules in structures with a photonic band-gap, studies on the matter are less numerous [121, 122]. A feature of the energy transfer process is that, when the two interacting entities are more than several wavelengths apart, transfer occurs through exchange of a real photon that must match the mode structure of the geometry. When the intermolecular distance is much smaller than the wavelength, the exchanged photon is virtual and need not match the mode structure. From this, one can predict that, inside the band-gap, energy transfer is inhibited for molecules more than a few periods apart, but not necessarily for molecules that are closer to each other.

All these properties of Photonic Crystals are very interesting in and of themselves.

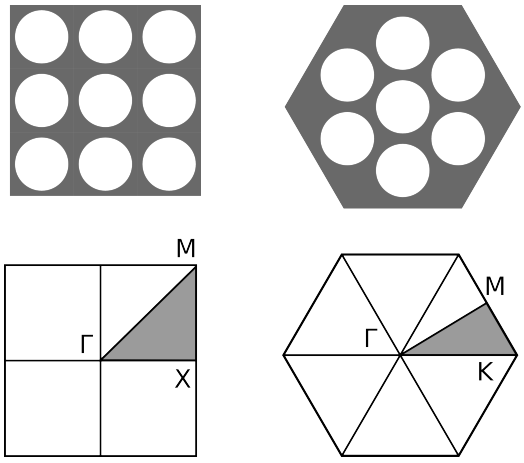

(a) *Square lattice* **(b)** *Triangular lattice*

Figure 4.1: *Geometry and reciprocal lattice of 2D Photonic Crystals (PhCs) of cylindrical air holes of radius $r = 0.42a$ in a dielectric with $\varepsilon = 12.0$; (a) Square lattice PhC and (b) Triangular lattice PhC.*

In this Chapter we consider a further addition to the geometry of a Photonic Crystal Slab, namely that of a metallic (Au) substrate. This introduces the possibility of exciting surface plasmon-polaritons at the interface between a Photonic Crystal Slab and the Au substrate. By adjusting the lattice constant of the Photonic Crystal Slab, the surface plasmon frequency can be brought close to the band-gap of the Photonic Crystal Slab. Consequently, the interesting area of overlap between plasmonics and Photonic Crystals can be investigated. We do so in this chapter by calculating the effect of the Photonic Crystal Slab with and without the Au substrate on the decay and energy transfer rates of molecules embedded in the structure.

This Chapter is organized as follows: in Section 4.2 we present a theoretical framework for calculating the decay and ET rates of a molecule in a Photonic Crystal Slab, different from the one we have used so far in the previous chapters. We also give a brief overview of the band-structures of 2D Photonic Crystals as well as the Photonic Crystal Slabs used in calculations. Section 4.3 is dedicated to presenting the results obtained from FDTD simulations of the rates of decay and energy transfer, as well as to the the discussion of these results. Finally, Section 4.4 is reserved for conclusions.

Fig. 4.1 schematically shows the geometry in real space and the reciprocal lattice for the square and triangular lattice Photonic Crystals we investigate in the course of this chapter.

4.2 Theoretical Framework

4.2.1 The Finite-Difference Time-Domain Method

In this chapter we depart from the formalism used thus-far in this work and we shall employ a different method for calculating the decay and energy transfer rates. We do this because the geometry of the 2D Photonic Crystal Slab we consider here is complex enough to preclude us from directly calculating its Green's tensor.

The method employed in this chapter is the *finite-difference time-domain* (FDTD) method [123]. In this subsection we shall briefly sketch out the FDTD technique, outlining its most salient features. This technique for solving the Maxwell equations in the time-domain was first introduced by Yee in 1966 [124]. Its advantages over other numerical techniques, including the Green's Tensor technique thus far used in previous chapters are as follows:

– The ability to deal with arbitrarily complex finite geometries;

– The ability to calculate either single-frequency or large bandwidth responses;

– Highly parallelizable.

The FDTD technique starts with the source-free Maxwell equations in the time-domain. Using finite differences, these equations are discretized on a rectangular grid (Yee grid), the $\mathbf{B}/\mathbf{H}$ fields being shifted from the $\mathbf{E}/\mathbf{D}$ fields by half a grid step in each (spatial and temporal) direction. This relative staggering of the fields has the drawback that interpolation may be required when the fields are needed at same location in space, e.g. for intensity or power flow calculations. In practice this is not a huge problem, as the fields usually vary slowly in space. To the above equations one must add the constitutive relations between $\mathbf{E}/\mathbf{D}$ and $\mathbf{B}/\mathbf{H}$, as well as the appropriate boundary conditions (we use open boundary conditions, implemented via *perfectly matched layers* PMLs). The whole system of fields is then propagated in time, monitoring and recording the desired physical quantities calculated from the fields.

This exposition of the FDTD technique is, by design, on the short side, as the technique is well-documented in the literature [123]. Given that the technique is in the time-domain, while we are focused on the frequency-domain, or steady-state response of a system, in the simulations presented in this chapter we propagate the fields for a long time until the steady-state regime is attained. This can constitute a heavy numerical burden, but it is the price we pay for being able to simulate more complex geometries.

In the next subsection we present a short alternative derivation of the decay and energy transfer rates in terms of quantities calculable from a FDTD simulation, i.e. power flows.

4.2.2 Decay rates, energy-transfer and FDTD calculations

Following the more in-depth presentation of [88], in this subsection we shall derive the decay rate of an emitter, Eq. (1.31), beginning from the definition of the decay rate as

$$\Gamma(\mathbf{r}_A, \omega_A) = \frac{\langle P(t) \rangle}{\omega_A} \tag{4.1}$$

where $\langle P(t) \rangle$ is the cycle-averaged power flow through a closed surface containing the emitter. This power flow through the surface can be written as an integral of the Poynting vector:

$$P(t) = \oint \mathrm{d}\mathbf{s} \cdot [\mathbf{E}(\mathbf{r},t) \times \mathbf{B}(\mathbf{r},t)], \tag{4.2}$$

which, using the divergence theorem and Maxwell's equations (1.1), becomes

$$P(t) = -\int \mathrm{d}V \left[\mathbf{H} \cdot \frac{\partial \mathbf{B}}{\partial t} + \mathbf{j} \cdot \mathbf{E} + \mathbf{E} \cdot \frac{\partial \mathbf{D}}{\partial t} \right]. \tag{4.3}$$

where the field vectors and the current density vectors are in the time-domain. Each of these vectors can be split, in the frequency-domain, into their positive and negative frequency components

$$\mathbf{A}(\mathbf{r},t) = \int_0^\infty \mathrm{d}\omega \left[\mathbf{A}^+(\mathbf{r},\omega)\, \mathrm{e}^{-i\omega t} + \mathbf{A}^-(\mathbf{r},\omega)\, \mathrm{e}^{i\omega t} \right]. \tag{4.4}$$

Since the emitter can be approximated by an electric point dipole located at $\mathbf{r}_A$ and with a sharp transition frequency, ω_A, the positive and negative frequency components of the current density $\mathbf{j}(\mathbf{r},t)$ can be written as [88]

$$\mathbf{j}^\pm(\mathbf{r},\omega) = \mp i\omega\mu\, \delta(\omega - \omega_A)\, \delta(\mathbf{r} - \mathbf{r}_A), \tag{4.5}$$

whereby the current density becomes

$$\mathbf{j}(\mathbf{r},t) = -i\omega_A \mu\, \mathrm{e}^{-i\omega_A t}\, \delta(\mathbf{r} - \mathbf{r}_A) + \mathrm{c.c.} \tag{4.6}$$

If one now performs a cycle-average of the power flow from Eq. (4.3) making use of the expression above for the current density, and the constitutive relations for the Maxwell equations,

$$\mathbf{H}^\pm(\mathbf{r},\omega) = \mathbf{B}^\pm(\mathbf{r},\omega), \quad \mathbf{D}^\pm(\mathbf{r},\omega) = \varepsilon(\omega)\mathbf{E}^\pm(\mathbf{r},\omega), \tag{4.7}$$

one obtains:

$$\langle P(t) \rangle = -\int \mathrm{d}V \left[\mathbf{j}^+ \cdot \mathbf{E}^- + \mathbf{j}^- \cdot \mathbf{E}^+ + 2\omega_A \varepsilon''(\omega_A) \mathbf{E}^+ \cdot \mathbf{E}^- \right], \tag{4.8}$$

where $\varepsilon''(\omega_A)$ is the imaginary part of the dielectric permittivity of the medium in which the molecule is embedded. As we only consider cases where the radiating molecule itself is embedded in an inert medium with a real dielectric permittivity, and only adjacent to absorbing media, the last term in the above expression drops out and we are left with:

$$\langle P(t)\rangle = -\int \mathrm{d}V \left[\mathbf{j}^{+}\cdot\mathbf{E}^{-}+\mathbf{j}^{-}\cdot\mathbf{E}^{+}\right]. \tag{4.9}$$

Considering the Maxwell equations Eq. (1.6) for the positive and negative frequency components,

$$\nabla\times\mathbf{E}^{\pm}(\mathbf{r},\omega) = \pm i\omega\mathbf{B}^{\pm}(\mathbf{r},\omega), \tag{4.10a}$$

$$\nabla\times\mathbf{H}^{\pm}(\mathbf{r},\omega) = \mathbf{j}^{\pm}(\mathbf{r},\omega)\mp i\omega\mathbf{D}^{\pm}(\mathbf{r},\omega), \tag{4.10b}$$

using the constitutive relations (4.7), and combining the above two expressions, one obtains for the electric field the following equation:

$$\nabla\times\nabla\times\mathbf{E}^{\pm}(\mathbf{r},\omega) - \omega^2\varepsilon(\omega)\mathbf{E}^{\pm}(\mathbf{r},\omega) = \pm i\omega\mathbf{j}^{\pm}(\mathbf{r},\omega). \tag{4.11}$$

This differential equation is usually solved by introducing the Green's tensor for the electric field [125, 126], in terms of which the electric field becomes

$$\mathbf{E}^{\pm}(\mathbf{r},\omega) = \pm i\omega\int \mathrm{d}^3s\,\mathscr{G}^{\pm}(\mathbf{r},\mathbf{s},\omega)\cdot\mathbf{j}^{\pm}(\mathbf{s},\omega). \tag{4.12}$$

Using the fact that $\mathscr{G}^{+}(\mathbf{r},\mathbf{s},\omega)\equiv\mathscr{G}(\mathbf{r},\mathbf{s},\omega)$, $\mathscr{G}^{-}(\mathbf{r},\mathbf{s},\omega)=\mathscr{G}(\mathbf{r},\mathbf{s},-\omega)=\mathscr{G}^{*}(\mathbf{r},\mathbf{s},\omega)$ together with expressions (4.5) for the current density, and (4.12) for the electric field, the cycle-averaged power flow from (4.8) now becomes

$$\langle P(t)\rangle = 2\omega_A^3\mu_i\mathrm{Im}\mathscr{G}_{ij}(\mathbf{r}_A,\mathbf{r}_A,\omega_A)\mu_j. \tag{4.13}$$

Taking Eq. (4.1) into account, the decay rate becomes

$$\Gamma(\mathbf{r}_A,\omega_A) = 2\omega_A^2\mu_i\mathrm{Im}\mathscr{G}_{ij}(\mathbf{r}_A,\mathbf{r}_A,\omega_A)\mu_j, \tag{4.14}$$

which is, evidently, identical with Eq. (1.31). It follows that the decay rate can be calculated by monitoring the power flow away from the emitter.

When we turn to the ET rate between two molecules in a FDTD formulation, the connection is even more straightforward. As Eq. (1.51) shows, the ET rate between two molecules is proportional to the absolute-value squared of the Green's tensor in the geometry into which the molecules are embedded. The Green's tensor, on the other hand, gives the Cartesian components of the electric field produced by a point dipole charge density (see Eqs. (4.5) and (4.12)), so that the ET rate can be directly calculated from the electric field produced by the donor molecule at the position of the acceptor.

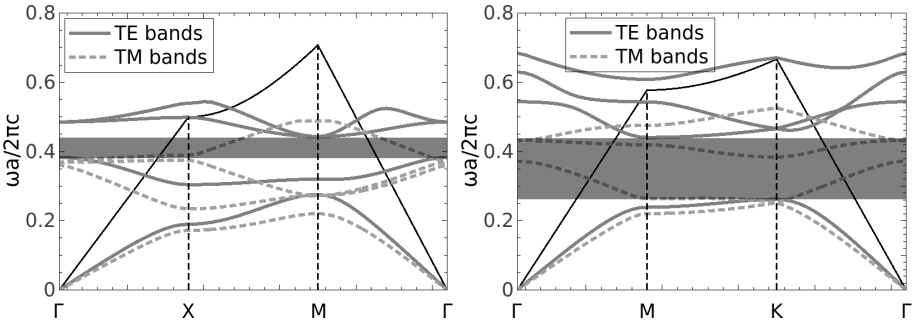

(a) *Square lattice PhC* **(b)** *Triangular lattice PhC*

Figure 4.2: *Band diagrams of 2D Photonic Crystals of cylindrical air holes of radius $r = 0.42a$ in a dielectric with $\varepsilon = 12.0$; (a) Square lattice PhC and (b) Triangular lattice PhC. The solid curve represents the light-line in vacuum and band-gaps are represented as gray shaded regions.*

Having build the framework for calculating the decay and ET rates in a FDTD formalism, we next consider the band diagrams of several photonic crystal structures, focusing on band-gaps, as these can strongly influence both the decay rate of a molecule and the ET rates between molecules embedded in such structures.

4.2.3 Photonic Crystals and band structures

In this subsection we shall give an overview of the band structure of 2D Photonic Crystals of circular air-holes in a dielectric medium, paying particular attention to the presence or absence of photonic band-gaps in the band-diagram of the structure. Fig. 4.2 shows the band diagrams for a square (Fig. 4.2a) and a triangular (Fig. 4.2b) 2D Photonic Crystal of infinitely long air-holes drilled in a material of permittivity $\varepsilon_b = 12.0$ (Silicon), with both transverse electric (TE) and transverse magnetic (TM) bands being shown. The square 2D structure has a TE band gap between $\omega a/2\pi c = 0.382$ and $\omega a/2\pi c = 0.443$, while the triangular lattice has a larger band-gap, also for TE modes, between $\omega a/2\pi c = 0.261$ and $\omega a/2\pi c = 0.441$, where a is the lattice constant of each structure. These band diagrams have been calculated using the MIT Photonic-Bands package [127].

The 2D Photonic Crystal considered above is periodic in the xy-plane, i.e. the infinitely long air-holes are along the z-axis. If this structure is now truncated in the z-direction, such that it now has a finite thickness h, it will lose its translational invariance along the z-axis, but will still be periodic in the xy-plane. In this case, the structure effectively forms a *Photonic Crystal Slab* (PhCS), as shown in Fig. 4.3. Fig. 4.4 shows the band diagrams of square and triangular lattice Photonic Crystal

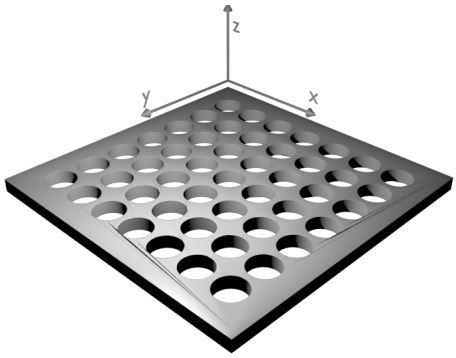

Figure 4.3: *Schematic geometry of a Photonic Crystal Slab with a square lattice.*

Slabs, for the same parameters as in Fig. 4.2 and two slab thicknesses. The shaded regions in these band diagrams represent the interior of the light-cone in vacuum, where *radiation modes* live, i.e. modes that propagate freely inside the slab, as well as in the surrounding vacuum. Below the light-cone in vacuum is the region of *guided modes*. These modes propagate inside the Photonic Crystal Slab, and are evanescent in the surrounding vacuum. Since the translational invariance along the z-axis is now lost, the modes that can be excited in the slabs can no longer be categorized as either TE or TM. However, there exists now a mirror symmetry with respect to the plane $z = 0$ which bisects the Photonic Crystal Slab in half and the modes supported by the slab can be categorized according to their symmetry with respect to this plane as either *even* (TE-like) or *odd* (TM-like). The electric field of the even modes is symmetric with respect to the $z = 0$ plane, while the electric field of the odd modes is antisymmetric. Panels. 4.4a and 4.4c, for which the PhCS thickness is $h = 0.5\,a$, show several photonic band-gaps for guided modes in the two types of lattices, square and triangular. As for the case of a 2D Photonic Crystal, where the TE band-gap was largest, the triangular lattice exhibits the largest band-gap in even modes. When the thickness of the slab is increased to $h = 1.0\,a$, the bands are packed closer together, the band-gaps shrink and can even disappear (Panels. 4.4b and 4.4d). The dependence of the band-gap size on slab thickness is, however, not monotonous, and the 2D band structure is recovered in the limit of an infinitely thick slab [128].

4.3 Results and Discussion

In the present chapter we will consider *finite* structures only. That is, the periodicity in the plane of the PhC is broken as we consider geometries consisting of a finite

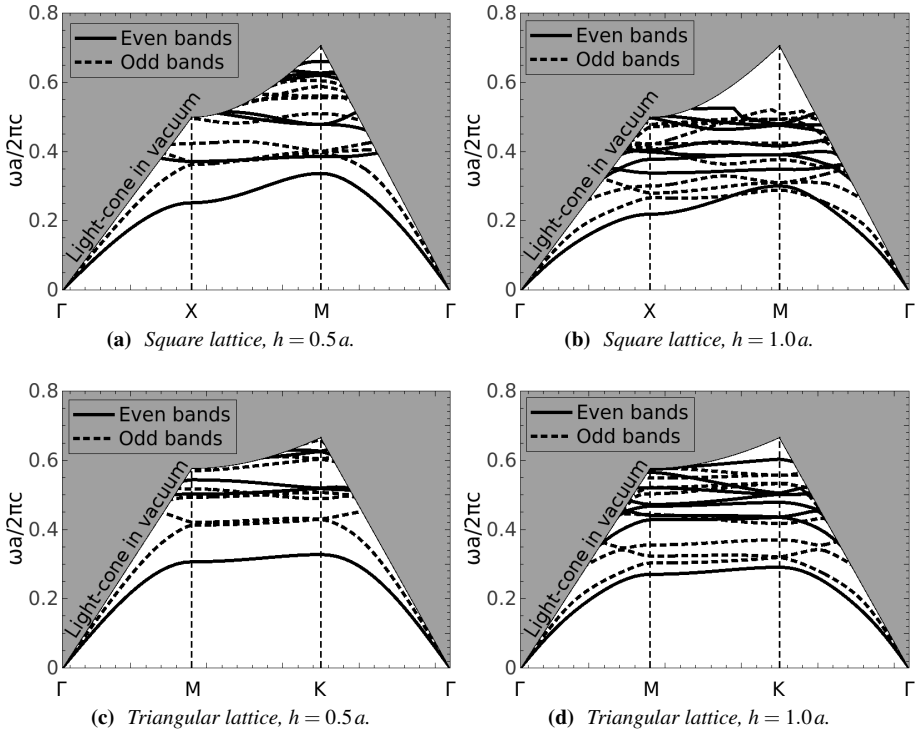

(a) *Square lattice, $h = 0.5a$.* **(b)** *Square lattice, $h = 1.0a$.*

(c) *Triangular lattice, $h = 0.5a$.* **(d)** *Triangular lattice, $h = 1.0a$.*

Figure 4.4: *Band diagram of Photonic Crystal Slabs with a square and triangular lattice of air-holes of radius $r = 0.42a$ in a dielectric with permittivity $\varepsilon_b = 12$ (Silicon). The shaded region represents radiation modes, above the light-line in vacuum.*

number of air-holes in a dielectric background. If the number of air-holes is sufficiently large (approx 7×7 for the parameters we use here [129]), the band diagram of the geometry does not differ appreciably from that of an infinite PhC slab.

4.3.1 Decay rates

We now consider the decay rate of a molecule placed inside Photonic Crystal Slabs with square and triangular lattices. We calculate the decay rate for a molecule placed in the middle of Photonic Crystal Slabs formed by 7×7 air-holes in a dielectric slab (thus, the molecule is located at the center of the structure's central air-hole). Fig. 4.5 shows the decay rate of a molecule in a Photonic Crystal Slab with a square lattice (Figs. 4.5a and 4.5b) and a triangular lattice (Figs. 4.5c and 4.5d), when the molecular

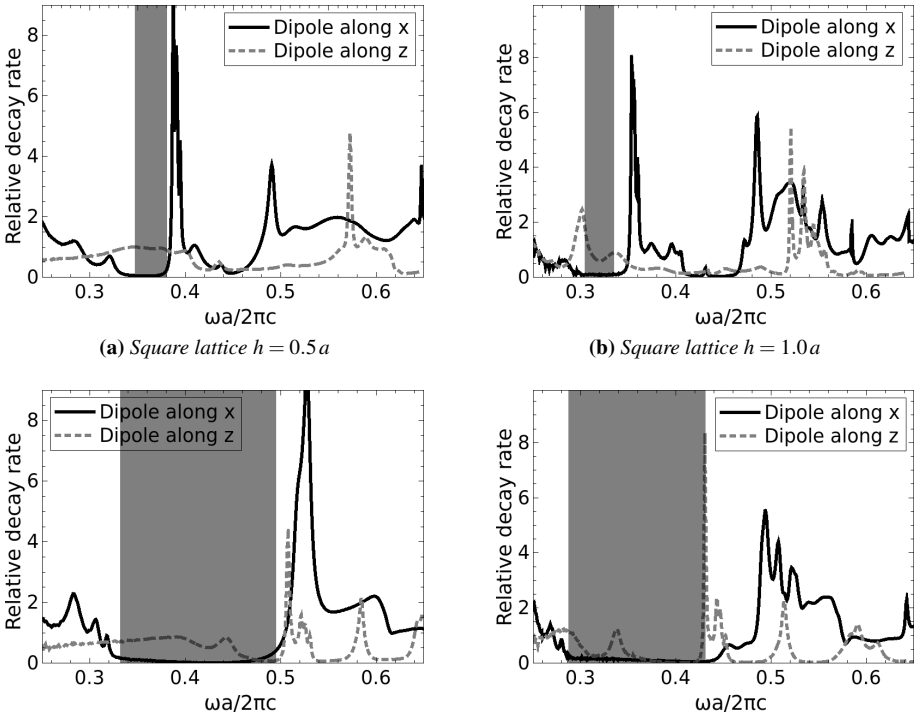

(a) *Square lattice* $h = 0.5a$ **(b)** *Square lattice* $h = 1.0a$

(c) *Triangular lattice,* $h = 0.5a$ **(d)** *Triangular lattice,* $h = 1.0a$

Figure 4.5: *Decay rate relative to free-space for an emitter at the center of a* 7×7 *square and triangular lattice PhC slab with* $h = 0.5a$ *and* $h = 1.0a$*, respectively. The air-hole radius is* $r = 0.42a$*, the dielectric permittivity of the background is* $\varepsilon_b = 12$ *(Silicon). The shaded regions indicate the guided-mode band-gaps.*

dipole is polarized along the z-axis (perpendicular to the slab and along the axis of the air-holes) and along the x-axis (in the plane of the slab), and for two slab heights, $h = 0.5a$ and $h = 1.0a$, respectively. When the molecular dipole is polarized in the plane of the slab, it can only couple to even modes in the geometry, and hence, its emission properties are influenced by the band diagram corresponding to even modes from Figs. 4.4. As such, the decay rate is inhibited in the frequency range corresponding to even-mode band-gaps (between $\omega a/2\pi c = 0.346$ and $\omega a/2\pi c = 0.421$ for $h = 0.5a$ and the square lattice and between $\omega a/2\pi c = 0.332$ and $\omega a/2\pi c = 0.495$ for $h = 0.5a$ and the triangular lattice) and it is enhanced at the edges of these band-gaps, where the density of states is relatively large. The finite size of the Photonic Crystal Slabs

used in our calculations (7×7) somewhat smooths out these effects, but they can be clearly seen. The decay rate is not completely inhibited, since the band-gap holds for guided modes only (modes below the light-cone in vacuum) and the emitter is still capable of coupling to radiation modes (modes above the light-cone in vacuum). This tends to increase the decay rate in the region of the guided-mode band-gap, and the effect is stronger for the square lattice than for the triangular one, whose band-gap is the largest.

For odd-modes, the guided mode band-gaps are smaller and, therefore, the inhibition of the decay rate is much less pronounced, for both the square and triangular lattices. The relevant curves in Fig. 4.5 are those corresponding to a dipole oriented along the z axis.

When the thickness of the slab is increased to $h = 1.0\,a$, Fig. 4.4b shows that the band structures of the square lattice is compressed, while roughly keeping its shape. As such, one would expect that the decay rate for this second case should be similar to the decay rate from Figs. 4.5a. Furthermore, since now the thickness of the slab is larger and the molecule is placed in the middle of the slab, coupling to radiation modes is weaker in this case. The expectation is that the features of the decay rate are sharper, as the bands and band-gaps are better defined. This is indeed what Fig. 4.5b shows: the structure of the decay rate is compressed towards lower frequencies and the peaks in the decay rate are sharper and more pronounced than in the case of the thinner slab from Fig. 4.5a. A triangular structure Photonic Crystal slab of thickness $h = 1.0\,a$ behaves in a similar manner (compare Figs. 4.5c and 4.5d).

We now consider the effect that the addition of a gold (Au) substrate to the Photonic Crystal Slab has on the decay rate of an emitter embedded in the slab. The Au substrate is semi-infinite, extending out from the bottom surface of the Photonic Crystal slab, towards $z \to -\infty$. We consider two positions of the emitter molecule, at the center of the central air hole of the Photonic Crystal Slab, and an off-center position, 15 nm away from the surface of the Au substrate, on the z-axis of the central air-hole. Because Maxwell's equations are scale invariant, i.e. there is no absolute length scale, in Fig. 4.5 we have used the lattice constant of the Photonic Crystal Slab, a, as a normalization length. When introducing the Au substrate, however, described by a frequency-dependent (or wavelength-dependent) dielectric permittivity [92], this frequency-dependence introduces a length scale in the problem, i.e. the surface-plasmon wavelength, and we have chosen the lattice constant a of the Photonic Crystal Slab such that $a = 200$ nm. Fig. 4.6 shows the relative decay rates of an emitter in the presence and absence of the Au substrate, for two orientations and for the two positions of the emitter. The solid curve in all the panels shows the relative decay rate for an emitter in the center of the air-hole, in the absence of the Au substrate. This is the same curve as plotted in Fig. 4.5, now as a function of wavelength instead of frequency. The dotted curve corresponds to an emitter 15 nm away from the bottom

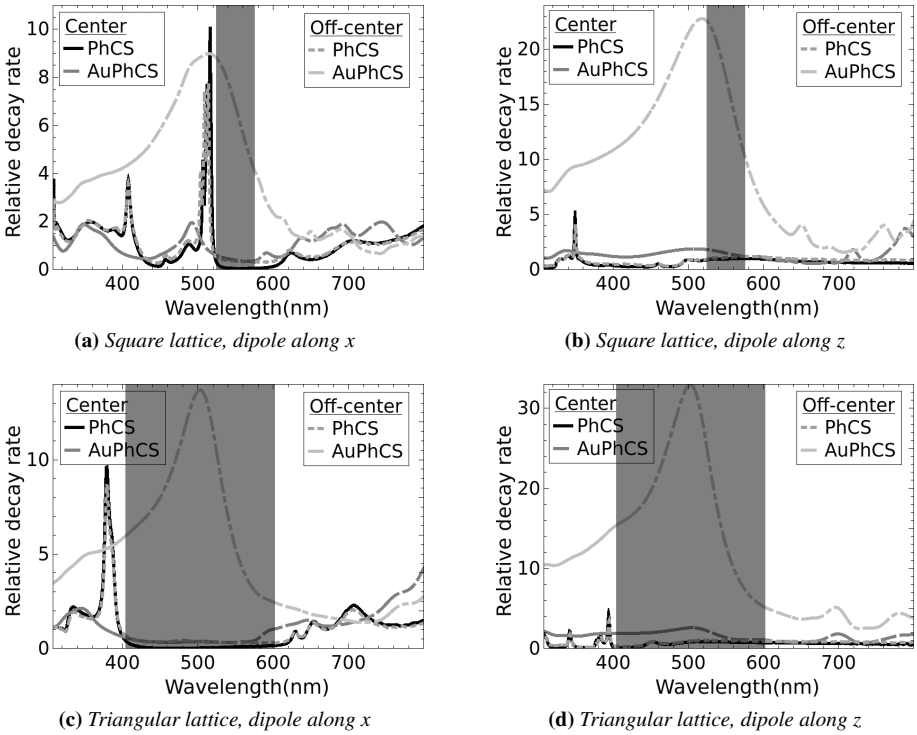

(a) *Square lattice, dipole along x*

(b) *Square lattice, dipole along z*

(c) *Triangular lattice, dipole along x*

(d) *Triangular lattice, dipole along z*

Figure 4.6: *Relative decay rate of a molecule at the center of a* 7×7 *square and triangular lattice Photonic Crystal Slab with* $h = 0.5a$ *on top of a Au substrate (AuPhCS). The air-hole radius is* $r = 0.42a$*, the dielectric permittivity of the background is* $\varepsilon_b = 12$ *(Silicon). The shaded regions indicate the guided-mode band-gaps.*

interface of the PhCS, also in the absence of the Au substrate. As is apparent from all the panels in Fig. 4.6, this change in the position of the emitter does not appreciably change its relative decay rate, except inside the band-gap, due to coupling to radiation modes. Otherwise, the two relative decay rate curves closely follow each-other. The addition of the Au substrate, on the other hand, has quite an appreciable effect on the relative decay rate, particularly for the off-center position of the emitter. The relative decay rate has a pronounced peak around 500 nm, which corresponds to the surface plasmon wavelength of Au. Furthermore, this peak is more pronounced for the off-center position of the emitter, where its near field can couple to the surface plasmon at the surface of the Au substrate. As further confirmation of the presence of the surface plasmon, we point to the fact that the peak is twice as large when the emitter dipole

moment is perpendicular to the substrate (Figs. 4.6b and 4.6d) as compared to the case when the emitter dipole moment is parallel to the substrate (Figs. 4.6a and 4.6c). A perpendicular dipole couples more strongly to a surface plasmon than a parallel one, due to smaller momentum mismatch.

4.3.2 Energy Transfer rates

We now consider the *Energy Transfer* (ET) rate between two molecules, a donor and an acceptor. The donor is at a fixed position inside the unit cell of the Photonic Crystal Slab, and we consider the energy transfer rate between this donor and an acceptor placed at different positions within the slab. Fig. 4.7 shows the frequency dependence of the relative ET rate in a PhC Slab for several donor-acceptor arrangements. Fig. 4.7a depicts the relative ET rate as a function of frequency for a donor placed at the center of the unit cell and polarized along the y axis and four positions of the acceptor along the x-direction of a square lattice Photonic Crystal Slab, $d = 0.15\,a$, $d = a$, $d = 3\,a$ and $d = 5\,a$, with a being the lattice constant. It can be clearly seen that, inside the band-gap of this structure, as depicted in Fig. 4.4a, energy transfer between the donor and acceptor is strongly inhibited for large intermolecular separations (e.g. $d = 5\,a$). This inhibition of the energy transfer rate becomes less pronounced for smaller intermolecular distances (vanishing completely for closely spaced donor-acceptor pairs, e.g. $d = 0.15\,a$), confirming the prediction we made in the introduction to this chapter. Furthermore, the region where this inhibition occurs agrees very well with the band-gap shown in Fig. 4.4a, despite the fact that we are dealing here with a finite structure, of 7×7 air-holes in the dielectric slab. This suggests that, as in the case of the decay rate from Fig. 4.5, the energy transfer rate is not particularly sensitive to the finite-size of the structure, provided this is large enough.

In Fig. 4.7c the frequency-dependence of the relative ET rate in a triangular lattice Photonic Crystal Slab is depicted. The donor is polarized along the y axis, and the positions of the acceptor are on the x-direction. From Fig. 4.4c, the band-gap for the triangular lattice is seen to be much larger than for the square lattice. The same effect of this band-gap on the relative energy transfer rate is present in the case of the triangular lattice, as it was for the square lattice, except appreciably stronger, due to the larger band-gap of the triangular lattice.

Panels 4.7b and 4.7d show the ET rate as a function of donor-acceptor distance along the x-direction and for several frequencies. The shaded regions represent the higher index host medium of the PhCS. As is apparent from these panels the ET rate for frequencies inside the respective band-gaps of the square and triangular lattices diminishes as the donor-acceptor distance is increased. Given that the panels depict the *relative* ET rate, i.e. normalized to the free-space value, this is entirely an effect of the band-gap. This proposition is further supported by the fact that, for frequencies

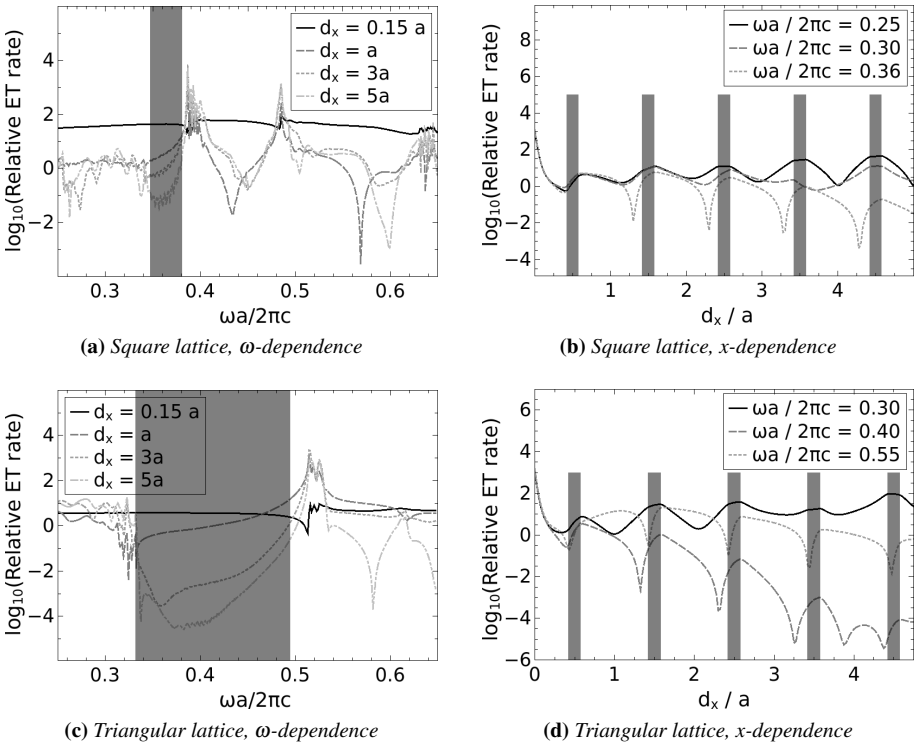

(a) *Square lattice, ω-dependence*

(b) *Square lattice, x-dependence*

(c) *Triangular lattice, ω-dependence*

(d) *Triangular lattice, x-dependence*

Figure 4.7: *Frequency and distance dependence of the relative ET rate for a donor molecule at the center of a unit cell of a PhC slab of thickness $h = 0.5a$ and an acceptor molecule displaced over a distance d_x along the x-axis from the donor. The donor dipole moment is oriented along the x-axis, while an average is performed over the orientations of the acceptor dipole moment. The shaded regions in panels (a) anc (c) indicate the guided-mode band-gaps.*

outside the band-gaps, no such trend is discernible.

One can make the above analysis more quantitative by explicitly considering the energy-time "uncertainty" relations, according to which $\Delta\omega\Delta t \approx \pi$. When the donor-acceptor distance is d, the *minimum* distance a (real or virtual) photon must travel is d (this travel distance is larger due to multiple scatterings in the PhC). The corresponding travel time is $\Delta t \gtrapprox d/c$. From this, the *maximum* spread in angular frequency is $\Delta\omega \lessapprox \pi c/d$ or, in terms of the *reduced* angular frequency, $\Delta\tilde{\omega} = \Delta\omega a/(2\pi c) \lessapprox a/2d$. When $d = 0.15\,a$, we have $\Delta\tilde{\omega} \lessapprox 3.3$, which is, in any case, much larger than the band-gap for either the square ($\Delta\tilde{\omega} \approx 0.075$) or the triangular ($\Delta\tilde{\omega} \approx 0.163$) lattice. As such, the spread in photon frequencies is much larger than the band-gap and, therefore, the

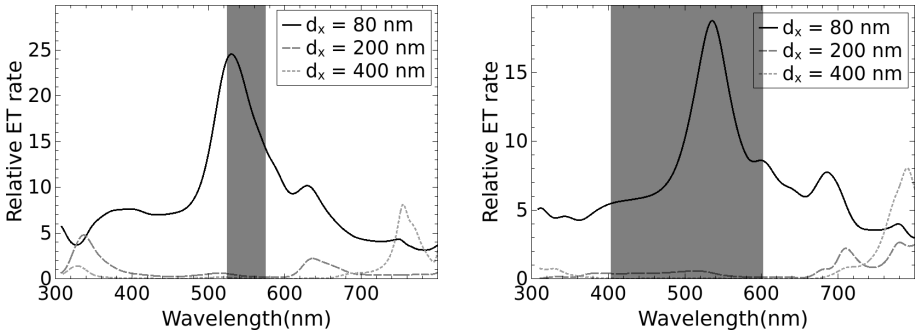

(a) *Square lattice* **(b)** *Triangular lattice*

Figure 4.8: *Wavelength dependence of the relative ET rate for a donor molecule located 15 nm above the Au substrate, at the center of a unit cell of a PhCS slab of thickness $h = 100$nm and an acceptor molecule displaced over a distance d_x along the x-axis from the donor. The donor dipole moment is oriented along the x-axis, while an average is performed over the orientations of the acceptor dipole moment. The shaded regions indicate the guided-mode band-gaps.*

band-gaps have a negligible effect on the ET rate. As the donor-acceptor separation is increased ($d = a, 3a, 5a$), the maximum spread in frequencies for the intermediate photons becomes smaller ($\Delta\tilde{\omega} \lessapprox 0.5, 0.16, 0.1$) and comparable to the size of the band-gaps. It becomes progressively more probable that nearly all intermediate photons have frequencies inside the band-gap, which leads to an inhibition of the ET rate for donor emission frequencies inside the band-gap.

If the Photonic Crystal Slab is now positioned on a Au substrate, the possibility of exciting surface plasmon-polaritons at the surface of the Au again presents itself. Figs. 4.8a and 4.8b show the relative ET rate between a donor located at the center of a PhCS on top of a Au substrate and at a height of 15 nm above the Au substrate, as a function of donor emission wavelength, for several positions of the acceptor along the x-direction and the square and triangular lattice considered before. In the presence of the Au substrate, an additional channel for energy transfer between donor and acceptor is opened, the SPP channel. When the transition wavelength of the donor is close to the SPP wavelength (around 500 nm), the SPP acts as a successful mediator of the energy transfer process between donor and acceptor, considerably enhancing the energy transfer rate. This effect is most striking when one considers that, as Fig. 4.8b particularly shows, the SPP wavelength overlaps with the band-gap of the PhCS and, therefore, the energy transfer rate is considerably reduced in the absence of the Au substrate.

4.4 Summary and Conclusions

Using an FDTD method we have calculated the decay rate of a molecule and the ET rates between two molecules in a PhC Slab with a square and triangular lattice in air and placed on top of a Au substrate. We have started by calculating the band-diagrams of the PhC slab and have seen the presence of several band-gaps for guided modes. The triangular lattice exhibits the largest such band-gaps, especially when the thickness of the PhC Slab is relatively small. Calculations of the decay rate of a molecule in a finite version of the PhC Slab in air show that the emission rate of the molecule is indeed inhibited for frequencies inside the band-gap, even when the structure is only 7×7 unit cells large. Enhancement of the decay rate is also observed at the edges of the band-gaps, due to the large local density of states here. When the PhCS is placed on top of a Au substrate, the surface plasmon supported by the interface leads to an appreciable enhancement of the decay rate at the surface plasmon frequency, which we have tuned to be inside the band-gap of the PhCS. This effect is more readily apparent for the triangular lattice PhCS, which has a larger band-gap.

We next calculated the ET rates between two molecules placed inside the PhCS. The donor was kept fixed at the center of a unit cell of the PhC Slab, and several positions of the acceptor were chosen. We were able to show that energy transfer inside the band-gap can be strongly inhibited if the intermolecular separation is larger than a few periods of the lattice. For smaller separations, the effect of the band-gap on the energy transfer rate disappears. This confirms a prediction made from a heuristic argument concerning real and virtual photons. When the PhCS is placed on top of the Au substrate, excitation of the surface plasmon at the interface leads to an enhancement of the ET rate for wavelengths inside the band-gap.

Conclusions

We begin this concluding chapter with a short summary of the work presented in this thesis, regarding which we will go into more detail as the chapter progresses. We have investigated in some detail the effect that certain nanoscale geometries have on the electromagnetic properties of atoms and molecules, such as the spontaneous emission rate of a molecule, and the electronic energy transfer rate between two molecules.

It has been known for close to three quarters of a century that the spontaneous emission rate of a molecule, the so-called Einstein A-coefficient, is not a coefficient at all, i.e. not a constant, but can depend on the environment in which the molecule is embedded (the Purcell effect). This effect has been harnessed in improving the efficiency of such opto-electronic devices as light-emitting diodes (LEDs) and micro-lasers. A striking example of the ability of the environment to control the emission properties of atoms and molecules can be encountered when one considers *photonic crystals*. These devices work for photons of light analogously to the way a semiconductor crystal works for electrons: due to Bragg scattering, propagation in certain directions, at certain energies, can be completely suppressed. This leads to discrete bands in the dispersion diagram of such crystals and, possibly, to the formation of partial or complete band-gaps. In these band-gaps, propagation in a wide range of directions is not permitted, effectively forming a photonic trap. When an excited molecule is placed in such a trap, it can no longer radiate away its energy in the form of a photon, and can be kept indefinitely in the excited state. The opposite of this effect is exploited in manufacturing LEDs. In this case, the emission probability of the molecule can be dramatically increased by the environment, thus improving the efficiency of LEDs.

The electronic transfer of excitation energy between two molecules can likewise be influenced by the environment in which the molecules find themselves embedded. As

the main channel by which an excited molecule transfers its excitation to a neighboring one, the ability to control this transfer of energy is obviously of great importance. Its applications include microscopy, biophysics, solar cells, etc. The possibility of using such states of the electromagnetic field as surface plasmon-polaritons to greatly increase the efficiency of the energy transfer becomes very exciting when one envisions electrically exciting a donor system, have it efficiently and rapidly transfer its excitation energy to an acceptor, and have the acceptor emit the energy in the form of a photon, whose properties could thus be precisely tailored. The same process in reverse would have the energy of a photon efficiently transferred and afterward converted into an electrical current. Evidently, what we have described is, in the first place, efficient and on-demand lighting, and, in the second place, photovoltaic cells. The story in the case of energy transfer, however, is more complex. If the spontaneous emission rate of a molecule is directly proportional to the local density of states at the position of the molecule and, hence, depends directly on the states of the electromagnetic field available to the emitting molecule, there exists no such simple relationship between the rate of transfer of energy and any local density of states, if the molecules are close enough to each other.

The work described in this thesis lies close to the basis of this technology. We have endeavored to investigate how environments that are structured at the nanoscale influence and affect the rate of energy transfer between donor and acceptor, as well as the spontaneous emission rate of emitters.

In the General Introduction chapter, we have given a general introduction to the subject of our work in this thesis, putting it in its proper context and outlining its purely scientific, as well as technological importance.

In Chapter 1 we have set up a framework for calculating both the energy transfer and the spontaneous emission rates of molecules from the frequency-domain Green's tensor of the geometry under investigation. The advantage of a Green's tensor formalism is that the Green's tensor encapsulates several quantities of interest, such as spontaneous emission rates, level shifts (not discussed in this work), and energy transfer rates in one quantity. In the same chapter we have introduced surface plasmon-polaritons, which play a significant role in the work we have done.

In Chapter 2 we have investigated two different planar multilayered geometries: a metallic slab embedded in an inert dielectric environment, and a planar waveguide made up of a dielectric slab between two metallic plates. In both geometries, the presence of multiple planar interfaces and the symmetry of the structure leads to the dispersion relation for surface plasmon-polaritons splitting into several branches, one for each planar interface. This happens when the distance between these interfaces is smaller than the penetration depth of the surface plasmons in the respective media. These branches reflect the symmetry of the geometry. Thus, one has symmetric and antisymmetric surface plasmon-polariton branches, and their symmetry properties

determine how and whether molecules with different polarizations of their transition dipoles couple to these surface modes. For the case of a metallic slab embedded in a dielectric host, the influence of the SPPs on the SE and ET rates is greater close to the surface plasmon frequency, ω_{SP}, where the wavevector of SPPs is much larger than the wavevector of photons of the same frequency. This leads to subwavelength effects such as fast oscillations of the ET rate as a function of the molecule's position along the slab, and to several orders of magnitude enhancements of the rates when compared to free-space. The situation for the planar waveguide is similar in some aspects, except that the SPP dispersion relation now splits into four branches, corresponding to symmetric and antisymmetric SPPs, associated with the two types of interfaces present in this geometry: metal-dielectric and metal-vacuum. The presence of two types of interfaces leads to two surface plasmon frequencies, ω_{SPI} and ω_{SPE}; accordingly, the frequencies and polarizations of the molecules can be chosen in such a way that they preferentially couple only to one branch of the SPPs. Energy transfer and emission can thus be channeled quite precisely and, as in the case of the metallic slab, enhancements of several orders of magnitude have been obtained for these rates, when compared to free-space. Thus, even in the case of such relatively simple geometries as metallic slabs or planar waveguides, the SE and ET rates can be reasonably well tailored and large enhancements of these rates can be obtained.

Chapter 3 considers the case of an infinitely long circular cylinder and investigates the effect that such a cylinder has on the ET rates of molecules. When the cylinder considered is made up of an inert dielectric material, the enhancement of the ET rate is rather modest, up to an order of magnitude. This enhancement is mostly concentrated at the surface of the cylinder, forming "hot-spots" separated along the angular direction (along the circumference of the cylinder) by approximately half the transition wavelength of the molecules. We have attributed this pattern of hot-spots to interference between modes with different angular index n. When we considered a metallic cylinder, the enhancement of the ET rate is several orders of magnitude, and also more localized at the surface of the cylinder. We have been able to show that this large enhancement and strong localization is due to excitation of SPPs at the surface of the cylinder, by considering the radial size of the hot-spots, and seeing that it accords well with the penetration depth of SPPs. Furthermore, the finite number of hot-spots localized at the surface of the cylinder can now be seen in a new light, as interference between SPPs with a small circular index n. Finally, we have considered the frequency dependence of the ET rate, and we have seen that the largest enhancement of the ET rate occurs close the the surface plasmon frequency ω_{SP}. Furthermore, the enhancement compared to free-space is appreciable only when the intermolecular distance is not too small compared to the transition wavelength of the molecules. This is in qualitative accordance with the argument from Heisenberg's uncertainty principle we have presented in the introductory chapter of this work.

Finally, in Chapter 4, we have considered a Photonic Crystal geometry and its effect on the spontaneous decay and the energy transfer rate between molecules. For these calculations, we have departed from the formalism presented in the Introduction and have employed a *finite-difference time-domain* method to calculate the SE and ET rates. The reason for this is that, in the case of the photonic crystal geometry, the Green's tensor method has only a limited usefulness, in some special cases. The FDTD method, on the other hand, is much more broadly applicable, although the disadvantage is that one gives up some of the analytical power this way. Using this method, we have calculated the spontaneous decay and ET rates of molecules embedded in square and triangular lattice Photonic Crystal Slabs of circular air-holes drilled in a dielectric background, both for the case when the PhCS is in air, and on top of a Au substrate. After obtaining the band-diagrams of the Photonic Crystal Slabs, we have calculated the spontaneous decay rate of a molecule in the middle of a finite 7×7 structure and have obtained results consistent with the band-diagram of the infinite periodic structure, for both the square and triangular lattice. The decay rate is inhibited inside the band-gaps, where the local density of states of the infinite structure vanishes, and it is enhanced at the edges of the band-gaps, which exhibit a larger local density of states. If the PhCS structure is placed on top of a Au substrate, excitation of the surface plasmon at the interface enhances the decay rate of the emitter at the SPP wavelength. As this wavelength was tuned to reside inside the band-gap of the PhCS in our calculations, the presence of the Au substrate has a powerfull effect on the decay rate of the emitter.

When considering the ET rate between two molecules located in the Photonic Crystal Slab, the effect of the photonic band-gap on the ET rate is more subtle. Reasoning from the viewpoint that the electromagnetic interaction between molecules occurs exclusively through exchange of photons, either real or virtual (the multipolar formulation of quantum electrodynamics), one can make a back-of-the-envelope argument concerning the effect of the band-gap of a periodic structure on the ET rate between two molecules embedded in that structure. The prediction is that, when the molecules are separated by much less than a few lattice constants, the effect of the band-gap on their interaction should be small. Conversely, this effect should increase as the intermolecular separation is increased above a few lattice constants. This is indeed what we have observed from our calculations, even in the case of a finite structure of relatively small size (7×7 unit cells). If, once again, the structure is placed on top of a Au substrate, excitation of the surface plasmon leads to an enhancement of the ET rate at the surface plasmon frequency, even when this frequency resides inside the band-gap.

In this work we have considered the electromagnetic properties of molecules, namely their decay rate and energy transfer rates between two molecules, in several nanostructured environments. Focusing primarily on the role of surface plasmon-

polaritons in modifying these rates, we have been able to show that the effect of these excitations is quite large, as they can provide several orders of magnitude of enhancement of both types of rates. For a single emitter, coupling to the surface plasmon greatly increases its decay rate, while the energy transfer between donor-acceptor pairs experiences a similar enhancement, because the SPPs serve as an additional channel to mediate the energy transfer. By carefully tailoring the geometric and/or material properties of the geometry, as well as the intrinsic parameters of the molecules, such as their transition frequency, it is possible to obtain very precise control of the emission and/or energy transfer rates of the molecules. The geometries presented in this work are but a small part of the toolkit that is available for this kind of precise control at the nanoscale. More complex geometries can be devised from, among others, the ones that we have presented here, to enrich the toolbox available in the field of optoelectronics.

Samenvatting

Het onderzoek gepresenteerd in dit proefschrift gaat over het modelleren van elektromagnetische interacties tussen kwantummechanische systemen, zoals moleculen, kwantum-dots etc. in de buurt van objecten met afmetingen die vergelijkbaar zijn met de golflengte van licht.

In buurt van deze objecten kunnen de elektromagnetische eigenschappen van individuele moleculen, zoals de vervalsnelheid of de levensduur, en voor paren moleculen, de snelheid van energie-overdracht van het ene molecuul naar het andere molecuul, drastisch veranderen. Om controle over deze processen te krijgen, is het belangrijk om te weten hoe objecten van de juiste grootte en vorm deze verschillende snelheden beïnvloeden. Deze processen spelen een sleutelrol in verscheidene toepassingen, zoals Licht-Emitterende Diodes (LEDs), micro-lasers, microscopen, zonne-cellen etc., en daarom is het van groot belang deze te kunnen sturen.

In dit proefschrift hebben wij getracht inzicht te bieden in het spontane emissie proces van een molecuul en het energietransport tussen twee moleculen, en de invloed die de omgeving op deze processen heeft. Hiervoor hebben wij gebruik gemaakt van de Green's tensor methode, waarmee het mogelijk is om de verschillende bijdrages aan de spontane emissie en het energietransport te scheiden, zoals de stralingsbijdrage, en die veroorzaakt door excitaties gebonden aan oppervlakken in de omgeving. Hoewel spontane emissie en energietransport kwantummechanische processen zijn, is het mogelijk om, met behulp van de Green's tensor methode, de snelheid van deze processen op een semi-klassieke manier te berekenen. Deze berekeningen zijn numeriek uitgevoerd, gebruik makend van een zelfgeschreven code. Op deze manier hebben we berekeningen gedaan voor de snelheden van spontane emissie en energietransport in drie verschillende omgevingen: in de nabijheid van een plaat en in een golfgeleider

(hoofdstuk 2), in de nabijheid van een diëlektrische en metalen cilinder (hoofdstuk 3) en in een plaat van fotonisch kristal (hoofdstuk 4). In de volgende alinea's zullen de resultaten uit deze hoofdstukken worden samengevat.

Hoofdstuk 1 is gewijd aan het opzetten van de basis waarop de berekeningen zijn uitgevoerd en geeft afleidingen van de vergelijkingen voor de snelheden van spontane emissie en energietransport vanuit de Green's tensor. Deze tensor wordt afgeleid in cartesische en cilindrische coördinaten en vervolgens uitgebreid naar de complexere geometrieën voor de volgende hoofdstukken. We hebben geprobeerd zo volledig mogelijk te zijn in de afleidingen, zodat dit proefschrift redelijk alleenstaand gelezen kan worden.

Hoofdstuk 2 beschouwt het geval van moleculen die dicht bij een metalen plaat of in een golfgeleider (bestaande uit twee metalen platen) geplaatst zijn. Hoewel de dikte van deze platen slechts enkele nanometers is, zijn ze oneindig groot in de andere richtingen. Een van de meest opvallende kenmerken van metalen oppervlakken, is het feit dat ze een bepaalde elektromagnetische toestand, een zogenaamd oppervlakte plasmon, toestaan. Zoals de naam al suggereert, is deze elektromagnetische golf gebonden aan het oppervlak van het metaal en kan deze energiedragende toestand zich voortplanten over dit oppervlak. Dit is de reden dat het oppervlakte plasmon kan optreden als een de-excitatie mogelijkheid voor een molecuul, of om energie transport tussen moleculen te faciliteren. We hebben laten zien dat oppervlakte plasmonen die zich voortplanten langs de twee oppervlakken van een metalen plaat, de vervalsnelheid van een molecuul met enkele orden van grootte kan doen toenemen. In het geval van een metalen plaat, zijn er twee mogelijke oppervlakte plasmonen, met een verschillende gebondenheid aan het oppervlak en met verschillende propagatielengtes. De manier waarop onze berekeningen zijn uitgevoerd, staat ons toe om de bijdragen die deze verschillende toestanden aan de spontane emissie snelheid hebben, te onderscheiden. De oppervlakte plasmonen bieden ook een mogelijkheid voor energietransport van een molecuul naar een nabij gelegen molecuul, dat zich ofwel aan dezelfde ofwel aan de andere kant van de metalen plaat bevindt. Ook in dit geval kan de snelheid van dit proces toenemen met enkele ordes van grootte.

In het geval van een golfgeleider, bestaande uit twee parallelle metalen platen met daar tussen een diëlektricum, zijn er vier verschillende oppervlakte plasmonen en hun bijdrage aan de snelheden voor spontane emissie en energietransport zorgen opnieuw voor een toename van enkele orden van grootte.

In hoofdstuk 3 beschouwen we het geval van diëlektrische en metalen cilinders. Als de cilinder gemaakt is van een diëlektricum, zien we een bescheiden verandering in de snelheden voor de spontane emissie en het energietransport (minder dat een orde van grootte). Dit geldt niet voor het geval dat de cilinder van metaal is. Vergelijkbaar met een metalen plaat, kunnen ook op een metalen cilinder oppervlakte plasmonen bestaan en deze kunnen zich voortplanten langs de cilinder-as. Langs de omtrek van

de cilinder zijn deze plasmonen staande golven, vergelijkbaar met de trillingen in een gespannen snaar. Door deze staande golven ontstaan 'hot-spots' langs de omtrek van de cilinder, waar de snelheid van het energietransport tussen twee moleculen zal toenemen. Deze 'hot-spots' komen overeen met de maxima van het elektromagnetische veld van het oppervlakte plasmon. Daarnaast hebben we laten zien dat er interferentie tussen verschillende plasmontoestanden mogelijk is en dat dit een bijdrage levert aan het patroon van het energietransport.

Tenslotte, hebben we in hoofdstuk 4 een andere geometrie beschouwd, namelijk die van een plaat van fotonisch kristal (*Photonic Crystal Slab* (PhCS)). Vergelijkbaar met een gewoon kristal, dat bestaat uit een periodieke rangschikking van atomen of ionen, bestaat een fotonisch kristal uit een periodieke rangschikking van elementen met een andere brekingsindex dan die van de matrix waar ze in zitten. Hierdoor hebben fotonische kristallen interessante optische eigenschappen, namelijk dat, voor bepaalde frequenties, licht zich in geen enkele richting kan voortplanten. Dit wordt een (volledig) *band gap* van het fotonische kristal genoemd, vergelijkbaar met een *band gap* in een half-geleider kristal.

Voor de berekeningen aan de PhCS, hebben we afgezien van het gebruik van de Green's tensor methode, omdat deze niet geschikt is voor dit systeem, en hebben we gebruik gemaakt van de 'finite-difference time-domain'-methode. Het voordeel van deze methode is dat hij kan omgaan met geometrieën van willekeurige complexiteit. De PhCS die we gebruikt hebben voor onze berekeningen, bestaat uit een plaat van een materiaal met een bepaalde dikte, waarin gaten zijn geboord. Dit geeft een tweedimensionale periodieke structuur. Als een molecuul in een dergelijke structuur wordt geplaatst, en zijn emissie-frequentie in de *band gap* van de PhCS valt, zal de vervalsnelheid van het molecuul sterk afnemen. De reden hiervoor is dat voor de frequentie waarop het molecuul licht wil uitzenden, licht zich niet kan voortplanten in de PhCS, en daarom het molecuul oneindig lang in zijn aangeslagen toestand zal blijven zitten. De situatie verandert wanneer we naar het energietransport tussen twee moleculen kijken. Als de moleculen zich ver genoeg uit elkaar bevinden, zal een vergelijkbare afname in de energietransport snelheid optreden. Dit effect zal echter geleidelijk verdwijnen als de moleculen dichter bij elkaar gebracht worden. Als de afstand tussen de moleculen klein is, dan kan licht tijdelijk de *band gap* negeren, en kan er energietransport plaatsvinden.

De geometrie van de PhCS kan ingewikkelder en interessanter gemaakt worden, door de PhCS boven op een metalen oppervlak te plaatsen. Hierdoor kunnen de effecten van de oppervlakte plasmonen (die de vervalsnelheid willen verhogen) gecombineerd worden met de effecten van het fotonische kristal (die deze snelheid willen verlagen). Uit onze resultaten blijkt dat, in het geval van competitie tussen het oppervlakte plasmon en het *band gap*, het oppervlakte plasmon domineert als het molecuul zich dichtbij het metalen oppervlak bevindt én zijn emissie-frequentie dicht bij de

oppervlakte plasmon frequentie ligt. In de andere gevallen zal het effect van het fotonische kristal domineren. Voor het energietransport geldt een vergelijkbare situatie.

De resultaten uit dit proefschrift zorgen voor een dieper begrip van de elektromagnetische interacties van moleculen (met licht en met andere moleculen), wanneer deze zich nabij nanostructuren bevinden. Dit begrip kan uiteindelijk bijdragen aan nieuwe strategieën bij het ontwerpen van materialen met optische functionaliteit op de nanometerschaal, zoals LEDs voor verlichting en zonnecellen om energie uit licht op te slaan.

Acknowledgements

And here I am finally at the last and most difficult to write part of the thesis. This has been a longer and more difficult journey than I expected when I started. All the more reason to be happy it's over and grateful to the people who helped along the way.

First and foremost I am greatly indebted to my supervisor, Jasper Knoester. He gave me the opportunity of doing a PhD in his group, and overlooked my idiosyncracies. He was generous and flexible enough to accept the less than usual arrangement of teleworking and sporadic communications and still managed to guide my research efficiently and well. I found our discussions always to be challenging and stimulating, as well as highly motivating.

I was lucky enough to be in a wonderful group during my PhD. Our lunches often went into overtime discussing a variety of subjects not related to Physics – when Jasper wasn't around. I still miss the volleyball practices on Sunday evening, though it never went anywhere professionally. To former and current members of the group, Victor, Maxim, Cătălin, Dirk-Jan, Joost, Arend, Rudolf, Bernard, Alina and Andrei, Sander, Michiel, thank you all for the good times. A special thank you to Thomas for the interesting discussions and his help in all matters computational, and to Jasper Compaijen for helping me with the translation (best of luck with your own thesis!).

Amalia, Anghel, Lavinia şi Oana, dacă Comunitatea nu era, trebuia inventată! Doar câteva cuvinte: plimbări cu bicicletele, mese, Porto, bătăi cu zăpadă, irişi, grădini zoologice, alegeri (chiar dacă o singură dată), parade de flori. Vă mulţumesc!

Mami, ştiu că nu ţi-a fost uşor, dar am făcut-o şi pe asta. Îţi mulţumesc pentru tot! Andreea, sper să fii la fel de mândră de mine, cum sunt eu de tine.

Amalia, nu ştiu unde aş fi fost fără tine. La câtă răbdare ai avut cu mine, poţi să-mi spui "Trebuie" de câte ori vrei!

Bibliography

[1] R. P. Feynman, R. B. Leighton, and M. L. Sands, *The Feynman Lectures on Physics* (Addison-Wesley, Boston, MA, USA, 1989).

[2] E. M. Purcell, Physical Review **69**, 681 (1946).

[3] H. Morawitz, Physical Review **187**, 1792 (1969).

[4] K. H. Drexhage, Journal of Luminescence **1-2**, 693 (1970).

[5] H. Khosravi and R. Loudon, Proceedings of the Royal Society A **433**, 337 (1991).

[6] E. Snoeks, A. Lagendijk, and A. Polman, Physical Review Letters **74**, 2459 (1995).

[7] R. M. Amos and W. L. Barnes, Physical Review B **55**, 7249 (1997).

[8] R. Matloob, Physical Review A **62**, 022113 (2000).

[9] F. Le Kien and K. Hakuta, Physical Review A **75**, 013423 (2007).

[10] C. Sanchez-Munoz, A. Gonzalez-Tudela, and C. Tejedor, Physical Review B **85**, 125301 (2012).

[11] P. Stehle, Physical Review A **2**, 102 (1970).

[12] P. W. Milonni, Optics Communications **9**, 119 (1973).

[13] M. R. Philpott, Chemical Physics Letters **19**, 435 (1973).

[14] H. Rigneault and S. Monneret, Physical Review A **54**, 2356 (1996).

[15] J.-K. Hwang, H.-Y. Ryu, and Y.-H. Lee, Physical Review B **60**, 4688 (1999).

[16] D. T. Alves, C. Farina, and A. C. Tort, Physical Review A **61**, 034102 (2000).

[17] W. L. Barnes, Contemporary Physics **41**, 287 (2000).

[18] D. Fussell, M. Dignam, M. Steel, C. M. de Sterke, and R. McPhedran, Physical Review A **74**, 043806 (2006).

[19] D. Bradshaw and M. Di Rosa, Physical Review A **83**, 053816 (2011).

[20] C. Reed, J. Giergiel, J. Hemminger, and S. Ushioda, Physical Review B **36**, 4990 (1987).

[21] T. Hakkarainen, T. Setälä, and A. Friberg, Physical Review A **84**, 033849 (2011).

[22] W. Żakowicz and M. Janowicz, Physical Review A **62**, 013820 (2000).

[23] T. Søndergaard and B. Tromborg, Physical Review A **64**, 033812 (2001).

[24] V. V. Klimov and M. Ducloy, Physical Review A **69**, 013812 (2004).

[25] D. Fussell, R. McPhedran, and C. M. de Sterke, Physical Review A **71**, 013815 (2005).

[26] N. S. Malik, E. Dupuy, J.-M. Ge, M. Munsch, and J. Claudon, Physical Review Letters **108**, 077405 (2012).

[27] H. Chew, The Journal of Chemical Physics **87**, 1355 (1987).

[28] H. Chew, Physical Review A **38**, 3410 (1988).

[29] H. T. Dung, L. Knöll, and D.-G. Welsch, Physical Review A **62**, 053804 (2000).

[30] H. T. Dung, L. Knöll, and D.-G. Welsch, Physical Review A **64**, 013804 (2001).

[31] L. A. Blanco and F. J. García de Abajo, Journal of Quantitative Spectroscopy and Radiative Transfer **89**, 37 (2004).

[32] C. Van Vlack, P. T. Kristensen, and S. Hughes, Physical Review B **85**, 075303 (2012).

[33] J. P. Dowling and C. M. Bowden, Physical Review A **46**, 612 (1992).

[34] R. Sprik, B. A. van Tiggelen, and A. Lagendijk, Europhysics Letters (EPL) **35**, 265 (1996).

[35] K. Busch, N. Vats, S. John, and B. Sanders, Physical Review E **62**, 4251 (2000).

[36] Y. Yang and S.-Y. Zhu, Physical Review A **62**, 013805 (2000).

[37] D. P. Fussell, R. C. McPhedran, and C. M. de Sterke, Physical Review E **70**, 066608 (2004).

[38] D. Fussell, R. McPhedran, and C. M. de Sterke, Physical Review E **72**, 046605 (2005).

[39] Q. Wang, S. Stobbe, and P. Lodahl, Physical Review Letters **107**, 167404 (2011).

[40] L. A. Blanco and F. J. García de Abajo, Physical Review B **69**, 205414 (2004).

[41] T. Ochiai, J.-I. Inoue, and K. Sakoda, Physical Review A **74**, 063818 (2006).

[42] F. Rosa, T. Mendes, A. Tenório, and C. Farina, Physical Review A **78**, 012105 (2008).

[43] A. Agarwal, G. D. Lilly, A. O. Govorov, and N. A. Kotov, Journal of Physical Chemistry C **112**, 18314 (2008).

[44] E. J. A. Kroekenstoel, E. Verhagen, R. J. Walters, L. Kuipers, and A. Polman, Applied Physics Letters **95**, 263106 (2009).

[45] *Resonance Energy Transfer*, edited by D. L. Andrews and A. A. Demidov (Wiley, New York, NY, USA, 1999).

[46] T. Förster, Annalen der Physik **2**, 55 (1948).

[47] J. S. Avery, Proceedings of the Physical Society **88**, 1 (1966).

[48] D. J. Griffiths, *Introduction to Quantum Mechanics* (Prentice Hall, Upper Saddle River, NJ, 1994).

[49] L. E. Ballentine, *Quantum Mechanics: A Modern Development* (World Scientific Publishing, Singapore, 1998).

[50] C. S. Yun, A. Javier, T. Jennings, M. Fisher, S. Hira, S. Peterson, B. Hopkins, N. O. Reich, and G. F. Strouse, Journal of the American Chemical Society **127**, 3115 (2005).

[51] T. L. Jennings, M. P. Singh, and G. F. Strouse, Journal of the American Chemical Society **128**, 5462 (2006).

[52] M. P. Singh and G. F. Strouse, Journal of the American Chemical Society **132**, 9383 (2010).

[53] M. Cho and R. L. Silbey, Chemical Physics Letters **242**, 291 (1995).

[54] M. de Dood, J. Knoester, A. Tip, and A. Polman, Physical Review B **71**, 115102 (2005).

[55] G. S. Agarwal and S. D. Gupta, Physical Review A **57**, 667 (1998).

[56] P. Andrew and W. L. Barnes, Science **290**, 785 (2000).

[57] T. Kobayashi, Q. Zheng, and T. Sekiguchi, Physics Letters A **199**, 21 (1995).

[58] T. Kobayashi, Q. Zheng, and T. Sekiguchi, Physical Review A **52**, 2835 (1995).

[59] D. M. Basko, G. C. La Rocca, F. Bassani, and V. M. Agranovich, physica status solidi (a) **190**, 379 (2002).

[60] V. V. Klimov and V. S. Letokhov, Physical Review A **58**, 3235 (1998).

[61] H. Fujiwara, K. Sasaki, and H. Masuhara, Chemphyschem **6**, 2410 (2005).

[62] S. D. Druger, S. Arnold, and L. M. Folan, The Journal of Chemical Physics **87**, 2649 (1987).

[63] F. Le Kien, S. Gupta, K. Nayak, and K. Hakuta, Physical Review A **72**, 063815 (2005).

[64] *Surface polaritons: Electromagnetic waves at surfaces and interfaces*, edited by V. M. Agranovich and A. A. Maradudin (North-Holland, Amsterdam, 1982).

[65] C. Argyropoulos, G. D'Aguanno, N. Mattiucci, N. Akozbek, M. Bloemer, and A. Alù, Physical Review B **85**, 024304 (2012).

[66] A. Chandran, E. Barnard, J. White, and M. Brongersma, Physical Review B **85**, 085416 (2012).

[67] H. Duan, A. I. Fernández-Domínguez, M. Bosman, S. A. Maier, and J. K. W. Yang, Nano Letters (2012).

[68] M. Pohl, V. Belotelov, I. Akimov, S. Kasture, A. Vengurlekar, A. Gopal, A. Zvezdin, D. Yakovlev, and M. Bayer, Physical Review B **85**, 081401(R) (2012).

[69] V. Siahpoush, T. Søndergaard, and J. Jung, Physical Review B **85**, 075305 (2012).

[70] D. E. Solis, B. Willingham, S. L. Nauert, L. S. Slaughter, J. Olson, P. Swanglap, A. Paul, W.-S. Chang, and S. Link, Nano Letters (2012).

[71] *Coherence and Statistics of Photons and Atoms*, edited by J. Perina (Wiley, New York, NY, USA, 2001).

[72] R. Hartman and P. Leung, Physical Review B **64**, 193308 (2001).

[73] M. Paulus and O. J. F. Martin, Optics Express **9**, 303 (2001).

[74] M. Paulus and O. J. F. Martin, Physical Review E **63**, 066615 (2001).

[75] I. Fernandez-Corbaton, N. Tischler, and G. Molina-Terriza, Physical Review A **84**, 053821 (2011).

[76] R. Matloob, Physical Review A **60**, 3421 (1999).

[77] V. Yannopapas and N. V. Vitanov, Physical Review A **81**, 042506 (2010).

[78] C. Eberlein and R. Zietal, Physical Review A **83**, 052514 (2011).

[79] J. A. Stratton, *Electromagnetic Theory* (IEEE Press, New York, NY, USA, 2007).

[80] L. D. Landau and E. M. Lifschitz, *Electrodynamics of Continuous Media* (Pergamon Press, Oxford, 1984).

[81] T. Gruner and D.-G. Welsch, Physical Review A **53**, 1818 (1996).

[82] H. T. Dung, L. Knöll, and D.-G. Welsch, Physical Review A **65**, 043813 (2002).

[83] H. T. Dung, L. Knöll, and D.-G. Welsch, Physical Review A **57**, 3931 (1998).

[84] W. H. Louisell, *Quantum Statistical Properties of Radiation* (Wiley, New York, NY, USA, 1973).

[85] S. Scheel, L. Knöll, and D.-G. Welsch, Physical Review A **58**, 700 (1998).

[86] T. Gruner and D. Welsch, Physical Review A **51**, 3246 (1995).

[87] D. P. Craig and T. Thirunamachandran, *Molecular Quantum Electrodynamics: An Introduction to Radiation Molecule Interactions* (Academic Press, New York, NY, USA, 1998).

[88] S. M. Barnett, B. Huttner, R. Loudon, and R. Matloob, Journal of Physics B **29**, 3763 (1996).

[89] W. C. Chew, *Waves and Fields in Inhomogeneous Media* (IEEE Press, New York, NY, USA, 1994).

[90] C. T. Tai, *Dyadic Green Functions in Electromagnetic Theory* (IEEE Press, New York, NY, USA, 1994).

[91] D. M. Basko, F. Bassani, G. C. La Rocca, and V. M. Agranovich, Physical Review B **62**, 015962 (2000).

[92] P. B. Johnson and R. W. Christy, Physical Review B **6**, 4370 (1972).

[93] G. W. Ford and W. H. Weber, Physics Reports **113**, 195 (1984).

[94] R. Ortuño, C. García-Meca, F. J. Rodríguez-Fortuño, J. Martí, and A. Martínez, Physical Review B **79**, 075425 (2009).

[95] E. N. Economou, Physical Review **182**, 539 (1969).

[96] X. Wang and K. Kempa, Physical Review B **71**, 085101 (2005).

[97] E. Moreno, F. García-Vidal, and L. Martín-Moreno, Physical Review B **69**, 121402 (2004).

[98] M. R. Philpott, The Journal of Chemical Physics **62**, 1812 (1975).

[99] H. A. Clark, R. Kopelman, R. Tjalkens, and M. A. Philbert, Analytical Chemistry **71**, 4837 (1999).

[100] W. Tan, Z. Shi, S. Smith, D. Birnbaum, and R. Kopelman, Science **258**, 778 (1992).

[101] E. Yablonovitch, Physical Review Letters **58**, 2059 (1987).

[102] S. John, Physical Review Letters **58**, 2486 (1987).

[103] J. W. S. Rayleigh, Philosophical Magazine **26**, 256 (1888).

[104] V. P. Bykov, Soviet Journal of Experimental and Theoretical Physics **35**, 269 (1972).

[105] V. P. Bykov, Quantum Electronics **4**, 861 (1975).

[106] S. John and J. Wang, Physical Review Letters **64**, 2418 (1990).

[107] K. M. Ho, C. T. Chan, and C. M. Soukoulis, Physical Review Letters **65**, 3152 (1990).

[108] S. John and J. Wang, Physical Review B **43**, 12772 (1991).

[109] G. Kurizki and A. Z. Genack, Physical Review Letters **61**, 2269 (1988).

[110] J. Martorell and N. Lawandy, Physical Review Letters **65**, 1877 (1990).

[111] S. John and T. Quang, Physical Review A **50**, 1764 (1994).

[112] S. Fan, P. Villeneuve, J. Joannopoulos, and E. Schubert, Physical Review Letters **78**, 3294 (1997).

[113] M. Woldeyohannes and S. John, Physical Review A **60**, 5046 (1999).

[114] R. K. Lee, Y. Xu, and A. Yariv, Journal of the Optical Society of America B **17**, 1438 (2000).

[115] N. Vats, S. John, and K. Busch, Physical Review A **65**, 043808 (2002).

[116] D. G. Angelakis, P. L. Knight, and E. Paspalakis, Contemporary Physics **45**, 303 (2004).

[117] W. Chow, Physical Review A **73**, 013821 (2006).

[118] A. F. Koenderink, M. Kafesaki, C. M. Soukoulis, and V. Sandoghdar, Journal of the Optical Society of America B **23**, 1196 (2006).

[119] P. Lodahl, A. Floris Van Driel, I. S. Nikolaev, A. Irman, K. Overgaag, D. Vanmaekelbergh, and W. L. Vos, Nature **430**, 654 (2004).

[120] M. Leistikow, A. Mosk, E. Yeganegi, S. Huisman, A. Lagendijk, and W. L. Vos, Physical Review Letters **107**, 193903 (2011).

[121] C.-H. Kuo and Z. Ye, Physical Review E **70**, 046617 (2004).

[122] M. V. Erementchouk, L. I. Deych, H. Noh, H. Cao, and A. A. Lisyansky, Journal of Physics: Condensed Matter **21**, 175401 (2009).

[123] A. Taflove and S. C. Hagness, *Computational Electrodynamics – The Finite-Difference Time-Domain Method*, 2nd ed. (Artech House, Norwood, MA, 2000).

[124] K. Yee, IEEE Transactions on Antennas and Propagation **14**, 302 (1966).

[125] C. A. Marocico and J. Knoester, Physical Review A **79**, 053816 (2009).

[126] C. A. Marocico and J. Knoester, Physical Review A **84**, 053824 (2011).

[127] S. Johnson and J. Joannopoulos, Optics Express **8**, 173 (2001).

[128] S. Johnson, S. Fan, P. Villeneuve, J. Joannopoulos, and L. Kolodziejski, Physical Review B **60**, 5751 (1999).

[129] M. Gerken and Y. Nazirizadeh, Journal of Nanophotonics **2**, 021795 (2008).